DEVELOPMENT OF AN INTEGRATED HYDROLOGICAL MODELING FRAMEWORK IN MOUNTAINOUS AREAS INCLUDING RAINFALL AND SNOWFALL QUANTIFICATION DERIVED FROM DATA INTEGRATION

A Dissertation

Submitted to the National Graduate Institute for Policy Studies (GRIPS)

and International Centre for Water Hazard and Risk Management (ICHARM),

Public Works Research Institute (PWRI)

in Partial Fulfillment of the Requirements for the Degree of

Ph.D. in Disaster Management

by

Asif Naseer

September 2018

Abstract

United Nations Water concluded that water is the core of sustainable development and its three dimensions (society, economy, and the environment). In most Asian countries, mountains bring fresh water to millions. Over mountainous regions, the precipitation mainly falls as snowfall in winter, causing a natural delay in river discharges by preserving winter precipitation to sustain streamflows during the summer. Hence, accurate estimation and prediction of discharge during all seasons are imperative to support optimal water resource planning and management. For sustainable development, there is increased focus on integrated water resource policies, which are unachievable without precise quantification of the available water resources.

One of the key gaps in knowledge regarding mountain regions is the interplay of precipitation and temperature with changing altitudes. An effort is made to propose a conceptual framework to bridge this gap and overcome the lack of observational data and large uncertainties due to the interplay of temperature and precipitation. This study integrates the merits of observational data with distributed atmospheric reanalysis and/or atmospheric model data to maximize their utilization in establishing a simplified, operational, and integrated approach. Due to significant biases, data from atmospheric reanalysis and/or atmospheric models are not frequently used to simulate the hydrological response specifically in a basin scale. However, through the integration of dynamical equations and model physics, these models have robust potential in developing 3-D distribution/profiles. Following the proposed framework, 2-D spatial distributions of precipitation and 3-D spatial distributions of temperature in the form of vertical profile of temperature (VPT) are achieved through integration of in-situ data with radar\reanalysis or atmospheric model products. The water and energy budget-

based distributed hydrological model with snow (WEB-DHM-S) is used to simulate the discharge and spatial distribution of snow cover using temperature reproduced from VPT and corrected precipitation with the logical calibration approach.

This framework was applied to the Oi River Basin of Japan due to policy implications regarding the maximization of hydropower generation and minimization of flood damages to downstream properties by improving dam operations. Precise estimation and prediction of discharge information are crucial for practitioners engaged in policy, planning, and operational roles for catchment management. The calibration and validation outcomes based on quantitative and spatial evaluation by pixel-by-pixel analysis were promising. The application of this study has robust potential toward developing countries like Pakistan suffering from frequent water-related disasters such as floods and droughts. It is because of the fact that recent current practices for water resource management are apparently becoming incompatible with growing demands of the agriculture, energy, and industrial sectors and in coping with water-related disasters under climate change. The glacier and snowmelt water from the northern mountain ranges of Pakistan are a prime source for sustaining river flows. It is therefore essential to incorporate accurate rainfall and snowfall quantification and distribution by integrating data optimize the available water resources. Through application of such integrated data analysis, a system can efficiently help policy and decision makers to effectively overcome the major water-related issues in the fields of irrigation and hydropower, and other industries associated with water.

Acknowledgement

Allah being the most beneficent and gracious, bestowed me with an opportunity to make my dream come true and gave me a chance to work with one of the world's best professors, Prof. Dr. Toshio KOIKE. I would like to express my sincere gratitude to my respected sensei for his continuous support, outstanding supervision, never-ending encouragement and motivation along with educational and professional guidance for my studies and truly generous and kind guidance for my life.

I would also like to thank my subadvisors Associate Prof. Abdul Wahid Mohamed RASMY and Prof. Hitoshi IEDA for their valuable suggestions and recommendations, guidance, and support during my research. I am obliged to Acting Chairperson of the Doctoral Programs Committee Prof. Alistar MUNRO and External Referee Prof. Yukiko HIRABAYASHI for their insightful comments, encouraging suggestions and review of my research work. I would also like to express my sincere thanks to Prof. Kuni TAKEUCHI, Prof. Shingi EGASHIRA and Prof. Shoji FUKUOKA for the valuable suggestions, recommendations and support for this doctorate program. I appreciate the educational team staff members from Mr. Katsuhito MIYAKE, Mr. Minoru KAMOTO, Mr. Yoshio TOKUNAGA and Mr. Takashi SHIRAI.

Very special thanks go to Dr. Asif Mumtaz BHATTI for his generous devotion to improving my hydrological modeling skills and mentoring me in multiple aspects for its proficient application and usability. I am thankful to Mr. Abdul MOIZ from the core of my heart for his help, tutoring and teaching throughout my research course. I am also grateful to Dr. Katsunori TAMAKAW, Dr. Maheswor SHRESTHA, Dr. Tomoki USHIYAMA, Dr. Miho OHARA, Dr. Cho Nyunt THANDA, and Dr. Daisuke HARADA for their kind advice and professional support.

I also want to highlight my appreciation to the support and guidance provided by Ms. Yukie OOKAWA for establishing a comfortable stay and her tiring efforts for countless arrangements. I am also grateful to Mrs. Mikiko NAKAMURA, Ms. Seiko TANAKA, Ms. Maiko Sano, and Ms. Rika KUMADA along with the supporting academic staff Ms. Yuki MIYABE, Ms. Masayo AWATA, and Ms. Yumiko ISHIMOTO for their politeness, kindness, and administrative assistance.

I wish to extend deep thanks for the priceless friendship, care and respectful companionship of Mr. Ahmad Ali GUL, Dr. Robin Kumar BISWAS, Mr. Neluwala PANDUKA, and Mr. Moez AHMAD. I would also like to talk about my lab mates and friends Dr. Nasif AHSAN, Mr. Irfan KHAN, Mr. Rashid BILAL, Mrs. Catherine Guevarra JACELDONE, Mrs. Chelsea TARUVINGA, Mr. Saqib JAHANGIR, Mr. Rizwan MALIK, Mr. Khairul ISLAM, Mr. Mahtab HUSSAIN, Dr. Nauman KHALID, Dr. Giselle Grace LIM, Dr. Jaki TAGUBASE, Dr. Yuanyuan PENG, and Dr. Vink KARINA.

I also want to express regards to my seniors from WAPDA, especially Imran Asim ALVI (late), GM, CDO (W), WAPDA, and Mirza Abdul REHMAN, Executive Engineer, Tarbela Dam Project, WAPDA. My colleagues include Mr. Zeeshan AHMED, Mr. Muhammad Asad YOUSAF, Mr. Syed Usman Ali SHAH, Mr. Ahmed Hasnat MAZHAR, Dr. Saleh IZHAR, Mr. Adnan YOUSAF, Mr. Nauman LIAQAT, Mr. Syed Ansar Raza SHERAZI, Mr. Atta MUHAMAD, Mr. Rana HAMAD and Mr. Mohammad BARKAAT.

Being selected for the joint program by the National Graduate School for Policy Studies (GRIPS) and International Centre for Water Hazard and Risk Management (ICHARM), in collaboration with Public Works Research Institute (PWRI), was a

dream come true. I am thankful to the selection committee and all of my mentors from these supporting institutes for the research facilities and technical support. I would like to pay my heartiest gratitude to ADB-JSP and the University of Tokyo, Japan, for making me able to step into such institutions and earn the most beautiful memories, which I shall cherish forever.

My parents, Naseer AHMED and Zahida NASEER, receive my deepest gratitude and love for their dedication and many years of support during my studies, which provided the foundation for this work. I am also obliged to my siblings Kashif, Mariam and Iqra for their continuous belief in me.

I would like to thank my wife HUMA for her understanding, love, and constant support for all the late nights and early mornings, and for keeping me sane over the past few months. Her unconditional moral support and encouragement were in the end what made this dissertation possible.

Last, but not least, I would like to dedicate this thesis to LAILA (CI-807)

Asif NASEER

Table of Content

List of Figures

List of Tables

Nomenclature and Abbreviations

AMeDAS	Automated Meteorological Data Acquisition System
anik	Anisotropic Hydraulic Conductivity Ratio
ASTER	Advanced Space-borne Thermal Emission and Reflection Radiometer
BATS	Biosphere Atmosphere Transfer Scheme
BCF	Bias Correction Factor
BHU	Basic Hydrological Unit
CAPPI	Constant Altitude Plan Position Indicator
CFV	Constant Fixed Value
CRHM	Cold Region Hydrological Model
DBHM	Distributed Biosphere Hydrological Model
DD	Degree Day
DEM	Digital Elevation Model
DHM	Distributed Hydrological Model
DHSVM	Distributed Hydrology Soils Vegetation Model
DIAS	Data Integration and Analysis System
ECMWF	European Center for Medium Range Weather Forecast
EOSDIS	Earth Observing System Data and Information System
EPA	Environmental Protection Agency
ERA	ECMWF Reanalysis
FAO	Food and Agriculture Organization
FPAR	Fraction of Photosynthetically Active Radiation
G/R	Gauge to Radar Precipitation Ratio
GBHM	Geomorphological Based Hydrological Model
GCM	General Circulation Model
GDEM	Global Digital Elevation Model
gpm	Geopotential Meters
hPa	hector-Pascal
IPCC	Intergovernmental Panel on Climate Change
JMA	Japan Meteorological Agency
JRA-25	Japanese 25-year Reanalysis

JRA-55	Japanese 55-year Reanalysis
ksat1	Saturated Surface Hydraulic Conductivity of Soil
LAI	Leaf Area Index
LSM	Land Surface Model
LWR	Longwave Radiation (W/m2)
MFV	Monthly Fixed Value
MODIS	Moderate Resolution Imaging Spectroradiometer
MRT	Modis Reprojection Tool
NASA	National Aeronautics and Space Administration
NIR	Near Infrared Albedo
NSE	Nash Sutcliffe Efficiency
NWP	Numerical Weather Prediction
OEI	Observation Elevation Interpolation
P	Pressure (Pa)
Pa	Pascal
PBIAS	Percent Bias
PPI	Plan Position Indicators
Preci	Precipitation
Qair	Relative Air Humidity
RCM	Regional Climate Model
SCA	Snow Cover Area
SFV	Seasonal Fixed Value
SiB2	Simple Biosphere Scheme 2
SnowMOD	Snowmelt Model
SSiB3	Simplified Simple Biosphere Scheme 3
SWR	Shortwave Radiation (W/m2)
Temp	Air Temperature
TI	Temperature Index
UEB-DSM	Utah Energy Balance Distributed Snow Model
UN	United Nations
USGS	United Stated Geological Survey

UTM	Universal Transverse Mercator
VIC	Variable Infiltration Capacity
VIS	Visible Albedo
VPT	Vertical Profile of Temperature
WATCLASS	Waterloo-Canadian Land Surface Scheme
WB	World Bank
WEB-DHM	Water Energy Budget based Distributed Hydrological Model
WEB-DHM-S	Water Energy Budget based Distributed Hydrological Model - Snow
WGS	World Geodetic System
WS	Wind Speed (m/s)

1. Introduction

1.1. Motivation

United Nations Water concluded that water is the core of sustainable development and its three dimensions (society, economy, and the environment). The existence of life on our planet is due to water which links and influences almost all aspects of our life directly or indirectly (EPA, 2013). According to the IPCC (2007), around 80% of the world's population is faces problems related to water availability and water security. On the other hand, the water-related disasters in the form of floods, droughts, and tsunamis, as well as windstorms under anthropogenic adversities, are undoubtedly recurrent making sustainable socioeconomic development and human security difficult to achieve (Adikari & Yoshitani, 2009).

The cryosphere is composed of solid water in the forms of snow, glaciers, sea ice, ice sheets or frozen ground or lakes, and it contributes three quarters of all fresh water. The seasonal snow cover and glacier ice are the foremost controllers for the dynamics of the Earth with respect to both climate and hydrology. Almost one-fourth of land surface comprises of mountains and high plateaus which play a pivotal role for mankind's climatic and hydrological concerns. One-sixth of the world's population depends on fresh water resources deposited as seasonal snow and ice over mountainous region (Barnett, Adam, & Lettenmaier, 2005; Immerzeel, Droogers, de Jong, & Bierkens, 2009; Minder, 2010). In most of Asian countries, mountains are the water towers bringing fresh water to the lives of millions (Immerzeel, van Beek, & Bierkens, 2010). The role of mountains is unique and significant in the renewal and cyclic provision of fresh water, mountain sustain the streamflow during seasons through the melting of accumulated snow, which depends on seasonal precipitation (Frans et al., 2016). In the

cold season, the water storage in snowpack, known as the snow water equivalent, is a function of both precipitation and temperature (Abatzoglou, 2011). Over mountainous regions, the precipitation mainly falls as snowfall in winter, causing a natural delay in river discharges by preserving winter precipitation to sustain streamflows during the summer. The discharges at the basin outlet are greatly dependent on the spatial distribution and temporal variability of precipitation (Shrestha et al., 2014). From the point of view of mountain hydrology, the seasonal snow cover and presence of glaciers are critical, as precipitation mostly occurs in solid form due to the cold climate and high elevation.

The air temperature variations in mountainous regions control the spatial seasonal patterns of precipitation; thus, temperature has a prime role in defining the physical state of precipitation with significant implications for sustaining seasonal flows. As a significant part of the hydrological cycle, snowmelt regulates flows (both surface and subsurface). For a snow-fed catchment, the two distinct physical states of precipitation (rainfall and snowfall) exhibit different hydrological responses. For such catchments it is difficult to devise a seamless integrated system that can deal with the coexistence of rainfall and snowfall. Therefore, it is critically important to simulate accumulation and melting precisely (Garen & Marks, 2005). Distributed hydrological models (DHMs) are becoming an essential tool for the simulation and analysis of the spatial and temporal variability of the hydrological response driven by snowmelt, facilitating effective water resource management (Abbott, Bathurst, Cunge, O'Connell, & Rasmussen, 1986; Bevan, 2001; Rigon, Bertoldi, & Over, 2006; Shrestha, Wang, Koike, Xue, & Hirabayashi, 2010). The modeling of seasonally snow-covered mountain basins,

considering processes such as snow accumulation, ablation, and snowmelt runoff, can be physically described using DHMs with a multilayer energy balance scheme.

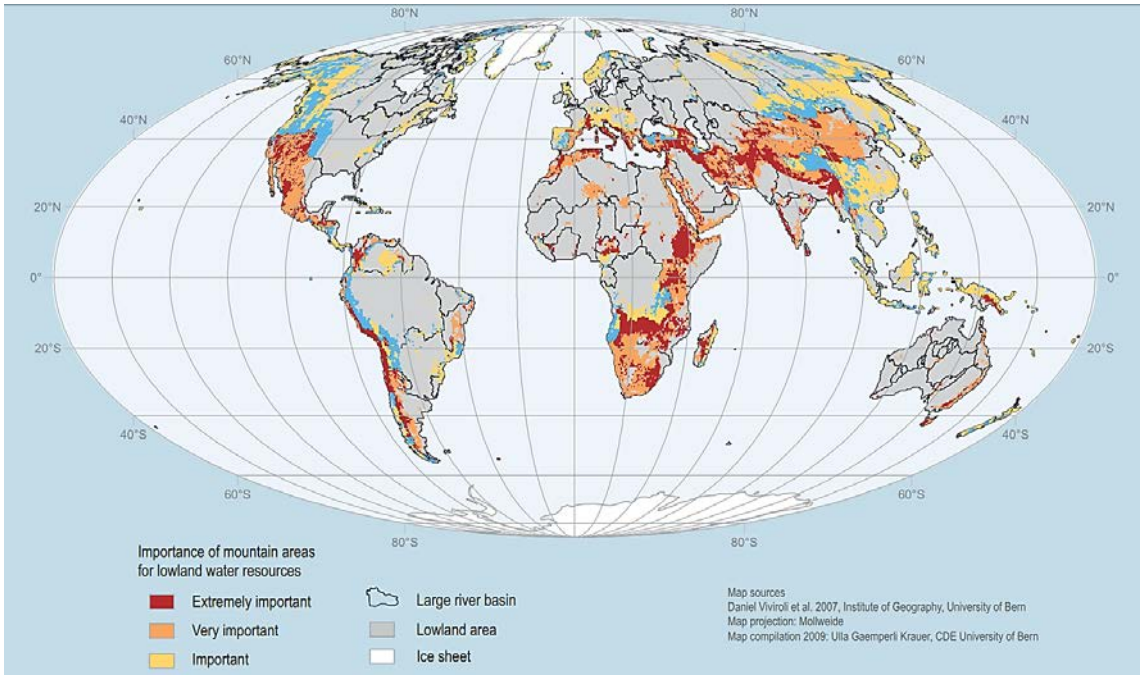

Figure 1.1. Importance of mountains as the water towers of world and their significance in specific regions (Viviroli, Dürr, Messerli, Meybeck, & Weingartner, 2007)

Over mountainous catchments, the temporal and spatial distribution of precipitation and air temperature are extremely variable (Valéry, Andréassian, & Perrin, 2010), but both are considered as primary meteorological variables in hydrological modeling (Immerzeel, Petersen, Ragettli, & Pellicciotti, 2014; Pellicciotti, Buergi, Immerzeel, Konz, & Shrestha, 2012; Wang et al., 2016). The key uncertainties in modeling mountainous region basins are the spatial distributions of both temperature (Kattel et al., 2013) and precipitation (Shrestha et al., 2014).

Modeling of the hydrological response in a mountainous watershed with snow is challenging due to the interplay between precipitation and temperature. Moreover, the coexistence of rain and snow adds to the complexity. Because of larger uncertainties in

these two important parameters, the calibration and application of a model for particular catchment are challenging issues. These uncertainties give rise to serious implications and still remain as major hurdles against operational and practical applications. Hence, accurate estimation and prediction of discharge during all seasons are imperative to support optimal water resource planning and management. For sustainable development, there is increased focus on the integrated water resource policies which are unachievable without precise quantification of the available water resources. Based on the above this research is motivated toward creating an integrated physically based modeling framework focusing on improved inputs to reduce the uncertainties from the limitations of input forcing.

1.2. Climate Change and Fresh Water Resources

Precipitation and potential evaporation are considered key climatic drivers that control various freshwater resources. Precipitation strongly depends on atmospheric water vapor content because saturation-specific humidity depends on temperature, and warmer air can hold much more water vapor. According to IPCC Working Group I's Fifth Assessment Report (WGI AR5), the surface temperature alters the vapor-carrying capacity of the atmosphere and the ratio of snowfall to precipitation; with a very high confidence level, it is likely to increase non-uniformly by about 1.5 times over the land compared to ocean. River discharges and wetland levels depend on the volume, timing and intensity of precipitation. Higher temperatures lead to increased evaporation and enhance the moisture-holding capacity of the atmosphere, which favor the climatic variability, with intensifying of both precipitation and droughts (Ntegeka, Willems, Baguis, & Roulin, 2015).

By the end of the 21st century, under different emission scenarios, the global average temperature is expected to rise by 1.1 ºC to 6.4 ºC (IPCC, 2007). Due to this expected increase in temperature, the rainfall intensity and changes in rainfall patterns (Alexander et al., 2006), as well as greater frequency of extreme events (Praskievicz & Chang, 2009), may further increase the frequency and/or intensity of floods (IPCC, 2014). Many studies had demonstrated that seasonal variations in water resources due to climate change are apparently more severe in snow dominated river basins (Barnett et al., 2005; Immerzeel et al., 2010; Minder, 2010; Mote, Hamlet, Clark, & Lettenmaier, 2005; Ntegeka et al., 2015). Climate change will impact the melting rate of glaciers as well as precipitation patterns (ratio of rainfall and snowfall), particularly affecting the timing and strength of monsoon rainfall, which will significantly impact the productivity and efficiency of water-dependent sectors such as agriculture. The significance of mountain snow and its implications for water resources have established serious concerns about future climate change due to possible rises in temperature (Minder, 2010). For regions with snow and glaciers under the influence of climate change, there are serious concerns due to rises in temperature that may eventually affect future streamflows; therefore, it is essential to predict snow and glacier melt runoff to manage future water resources. Given the influence of climate change, changes in the amount of snow covering the ground and changes in spring melts patterns, will directly or indirectly affect the water supplies for the downstream people utilizing it for different purposes in the agriculture, industry and energy sectors. The decreasing snowpack, altering snow cover and retreating glaciers are prompting concerns about dwindling water supplies from the perspectives of climate change.

1.3. Research Objective

The estimation of water is subject to precise quantification of rainfall, snowfall and mixed precipitation over a mountainous region. One of the key gaps of knowledge regarding mountain regions is the interplay of precipitation and temperature with changing altitudes. In addition, observations for these key meteorological parameters are sparse and limited. A 3-D temperature distribution is pivotal for obtaining a realistic picture of the temporal and spatial distribution of precipitation along with the physical state (rain/snow). In order to bridge this gap and to overcome the lack of observational data and the large uncertainties due to the interplay of temperature and precipitation, a development of deterministic physical approach to deal with uncertainties regarding rainfall and snowfall is of vital importance for a physically based hydrological modeling framework.

It is also anticipated to estimate or simulate snow cover to understand how the climate may be changing. In the short term, this information can help water managers to assess whether each winter's snowmelt will provide enough water for drinking, agriculture and other purposes of life. This study will be helpful for understanding various aspects of basin topography regarding the spatial and temporal distribution of precipitation and temperature collectively. It will also improve our knowledge of how any susceptible change in temperature due to the changing climate may alter seasonal precipitation patterns and distribution as well as snow dynamics linked to hydrological response.

The current research mainly emphasizes the:

1. Preparation of 3-D temperature data for establishing a VPT that will act as a realistic dynamic lapse rate at a basin scale

2. Precipitation-temperature interplay to deal with rainfall, snowfall, and the mixture of both in mountainous environments
3. Development of integrated data analysis system by combining the merits of observational data with distributed atmospheric reanalysis and/or an atmospheric model for data scarce regions
4. Application and influence of the above in connection with streamflows and the spatial distribution of snow cover extents
5. Integration of the system for seamless simulation of hydrological precipitation response and its anticipated physical states simultaneously over varying elevations
6. Establishment of a simplified, operational, and integrated approach

1.4. Outline of the Dissertation

The current chapter describe about the research motivation and objectives. Chapter 2 includes a literature review regarding different approaches and their limitations. Chapter 3 describes the methodology and conceptual framework of the research explains each component of the framework in detail. Chapter 4 is about the model selection and description of the selected DHM along with the modeling processes undertaken by the model. In Chapter 5, the development of three-dimensional temperature distributions for a basin scale by constructing a vertical profile is discussed in detail. In Chapter 6, the proposed conceptual framework is applied to one of the river basins, known as the Oi River Basin, in Japan. Also, the preparation of inputs datasets, the evaluation criteria, and the results of analysis are discussed in detail. Last chapter provides the concluding remarks.

2. Literature Review

2.1. Introduction

Snow is precipitation in the form of small white ice crystals formed directly from water vapor in the air at a temperature of less than 0 °C (273.15 K). It can be categorized as dry snow when all of the layers of the atmosphere are below freezing including the surface temperature. If the surface temperature is above freezing temperature, snow can melt slightly, thus adding more moisture and making it wet snow. The major difference between these two is surface temperature. The temperature of the Earth's surface is regulated by seasonal snow cover, whose melting helps to fill rivers and reservoirs in many regions of the world. In terms of area it is considered the largest single component covering 46,000,000 km^2 and playing a critical role for regulating the exchange of heat between Earth's surface and atmosphere. The snow's albedo is defined as the measure of sunlight reflected back into the atmosphere and its highest value ranging 80% to 90% of the incoming sunlight. By contrast, trees, plants, and soil reflect only 10% to 30% of sunlight. The reflectivity of snow helps Earth's energy balance because it reflects solar energy back into space, which helps to cool the planet.

In addition, the thermal properties of snow also play a pivotal role in controlling the heat and moisture circulation between the ground and atmosphere. As the soil freezes from due to insulation due to snow cover, this locks the exchange of gases like carbon dioxide and methane as well as chemical exchange between the ground and atmosphere. Due to the thermal properties of snow, its melting can be delayed. Based on temperature variations and other snow properties, the water likely to be available during the spring and summer melt can be estimated with the help of hydrologic modeling.

2.2. Limitation in Modeling Mountain Snow

Hydrological modeling comprises simplified conceptual representations of the hydrological cycle, expressed in mathematical equations, to simulate hydrological processes. Primarily, it is used to gain a better understanding of water and energy cycles and make hydrological predictions. Growth in computational power and improved understanding of hydrological processes have changed the modeling trend from lumped conceptual models to more sophisticated physically based DHMs (Troin, Arsenault, & Brissette, 2015). Various models have been developed and applied to address snowmelt and streamflow simulations ranging from simple degree day (DD)/temperature index (TI) approaches (Immerzeel, Pellicciotti, & Shrestha, 2012; Rango & Martinec, 1995; Tahir, Chevallier, Arnaud, Neppel, & Ahmad, 2011) to Energy Budget-based models (Garen & Marks, 2005; Rigon et al., 2006; Shrestha, Wang, Koike, Xue, & Hirabayashi, 2012; Tarboton, Luce, & Service, 1996). The DD/TI models indicate a definable and consistent relationship between temperature and energy exchange but are unable to model complex situations such as mixed precipitation rain and snow simultaneously or rain over snow (Garen & Marks, 2005).

DHMs are preferred over lumped models due to their effective representation of hydrological processes in terms of metrological inputs and temporal and spatial variability (Yang, Hearth, & Muisake, 2002). Over the past three decades, there have been significant developments in hydrological modeling (Beven, 2001) from conceptual models to DHMs, in terms of their application for simulation of hydrological responses, flood prediction, and rainfall-runoff modeling (Bevan & Kirkby, 1978; Ewen et al., 2000; Todini, 1988). Recently, the physically based DHMs have been used to analyze

climate change scenarios (Ntegeka et al., 2015) for prediction and water resource management.

The reliability of physically based DHMs depends on the physical meanings of the parameters included for accurate reproduction of hydrological responses (Pellicciotti et al., 2012). The absence of initial and boundary conditions, the model's structure, the inclusion of parameterization schemes, and most importantly, the static and dynamic data inputs are all reasons for uncertainties, which result in negative effects on model accuracy (Beck 1987; Doherty & Welter 2010; Song et al. 2015). According to Sellers et al. (1996) the inherent properties of snow such as low thermal conductivity and roughness and high albedo govern the energy and water interactions between the land surface and the atmosphere. Physical processes of snow can be expressed more realistically through a distributed hydrological system with water and energy budgets. Practically, the catchment inputs are insufficient to address all physical parameters of DHMs and many of the important characteristics of the model inputs cannot be measured completely or accurately, make the utility of DHMs questionable (Foglia, Hill, Mehl, & Burlando, 2009; Kunstmann, Krause, & Mayr, 2006; Scott, Gooseff, Bencala, & Runkel, 2003). Due to the physical meaning of the parameters involved in a physically based DHMs, principally, they do not need any calibration (Madsen, 2000) but improved understanding of dynamics of hydrological system has led to increased complexities, increasing the uncertainties (Liu & Gupta, 2007; Wagener & Gupta, 2005).

Currently, physically based DHMs are used extensively to analyze climate change scenarios and for prediction and effective management of water resources. However, the limitations/shortcomings originating from input datasets yield uncertainties. These

uncertainties give rise to serious implications and are still major hurdles against the applicability of various modeling approaches.

2.3. Data Limitations in Modeling Mountain Snow

Regarding mountainous hydrology, Beven (2001) demonstrated that the distribution of temperature and precipitation is governed by the presence and/or absence of moisture. Over mountainous catchments, the temporal and spatial distributions of precipitation and air temperature varies drastically and both are considered primary meteorological variables in hydrological modeling (Heynen et al., 2016). The modeling of the hydrological response in a mountainous watershed with snow is challenging due to the interplay between precipitation and temperature. Moreover, the coexistence of rain and snow adds to the complexity. The limitations due to precipitation and temperature are discussed in detail in the following sections.

2.3.1. Precipitation data and limitation

The precipitation itself is considered liquid (rainfall) or solid (snowfall) form of water leaving the atmosphere and moving towards the ground, generally, measured though various instrumental techniques (Sugiura, Yang, & Ohata, 2003). Most common is measurement through conventional rain gauges, such as ordinary rain gauges, cylindrical rain gauges, siphon rain gauges, and tripping bucket type rain gauges. Rain gauges measure rain directly and are therefore considered the most reliable source with least uncertainty involved. Approaches such as Thiessen polygons, inverse distance weighting, angular distance weighting, and kriging are used to obtain the rainfall and snowfall distribution using point data, but they subject to a great deal of uncertainty when gauging stations are sparse or unavailable at high elevations in mountainous terrain. Gauge precipitation measurements have systematic errors, specifically for

snowfall. The irregularities and steep topographical features in mountainous regions are a major hindrances for direct gauging of rain or snow, or for using remote-sensing technology for measuring precipitation (Nesbitt & Anders, 2009). Major constraints include the sparseness of meteorological stations, impact of topography on precipitation-pattern-induced under-catch, and losses due to evaporation and wetness along with an increasing fraction of solid precipitation (Goodison et al., 1989; Nešpor & Sevruk, 1999; Schwarb, 2000; Sevruk et al., 2009). Moreover, the precipitation gradients are not linearly correlated with altitudes and present an incomplete picture of precipitation distribution over high mountains where larger amounts of precipitation usually occur (Dahri et al., 2016; Immerzeel et al., 2014; Singh & Kumar, 1997).

On the other hand, radar is a value added source for the spatial representation of precipitation (Yang, Koike, & Tanizawa, 2004) but issues arise such as rain blocking by orography, different precipitation phases, and difficulties in estimating mixed-phase precipitation (Clark & Slater, 2006). Weather radars measure the precipitation rate indirectly by using radar reflectivity aloft. For various locations and precipitation types the power law relationship between radar reflectivity and precipitation rate is not consistent resulting as major source of uncertainty for radar precipitation estimates (Ghaemi, Kavianpour, Moazami, Hong, & Ayat, 2017). According to Shreshta et al. (2012), underestimation of 60% of the actual snowfall was reported, as compared to rain gauge measurements. By contrast, the measurements from ground-based radar reflectivity are non-uniform most of the time with uncertainty retrieval from 100% to 200%, which is quantitatively huge amounts of ambiguity (Wood, 2011). Saltikoff et al. (2015) conducted a recent effort to establish radar-based quantitative precipitation estimates by comparing datasets obtained from rain-gauges, weather radar, and

numerical weather predictions (NWPs) already in operation. In their study, various radar reflectivity equations were used to obtain mean ratio precipitation estimates in the European region, but the physical effect of the lapse rate of temperature with elevation was not considered.

In radar estimates, the distinction of precipitation phases is critically indispensable. Its complexity becomes even more pronounced when both precipitation physical states (rainfall and snowfall) appear co-incidentally over a mountainous region. Sometimes, precipitation, estimated as snow by radar, melts and is collected as rain while descending, due to temperature variations along the elevation. For snowfall, estimation by radar mainly depends on the relationship of radar reflectivity to snow particle microphysical properties, density of the snow particles, shape of the snow flakes, distribution of snow particles, and fall velocity of snowflakes (Cooper, Wood, & L ’ecuyer, 2017; Kulie & Bennartz, 2009; Wood, L’Ecuyer, Heymsfield, & Stephens, 2015). Remote-sensing data from satellites are another useful source for obtaining continuous gridded information, but intensive evaluation is indispensable because satellite-derived patterns may include significant margins of error—varying from 15% to 60% of the annual precipitation in some cases (Anders et al., 2006; Khan, Hong, Gourley, Khattak, & De Groeve, 2014; Gerard H. Roe, 2005).

2.3.2. Temperature data and limitations

In the case of temperature, the altitudinal distribution of air temperature is pivotally important in simulating of the contributions of rainfall and snowfall to towards streamflows. The additional controls due to orographic effects cause variations in the environmental lapse rate, making it different from environmental lapse rate that exists in free atmosphere. In hydrological modeling, researchers and modelers across the world

use the lapse-rate-derived temperature because of temperature perturbations (Zhang et al., 2015). For ease of understanding, the previous studies have categorized into four main classifications:

1. Constant fixed value (CFV)
2. Seasonal fixed value (SFV)
3. Monthly fixed value (MFV)
4. Observation elevation interpolation (OEI)

Constant fixed value

In free atmosphere, the average decrease of temperature as elevation increases is generally known as "the environmental lapse rate" (Berry, 2008). A uniform and/or constant environmental lapse rate (e.g., 6–6.5 K/km) over multiple years, as considered in a wide range of studies (Immerzeel, van Beek, Konz, Shrestha, & Bierkens, 2012; Maurer, Wood, Adam, Lettenmaier, & Nijssen, 2002; G. H. Roe & O'Neal, 2009; Shrestha et al., 2014; Tahir et al., 2011), is unrealistic and thus unable to represent the atmosphere of particular region during a particular season (Li et al., 2013; Marshall, Sharp, Burgess, & Anslow, 2007).

Seasonal fixed value

Some of the recent researches are applied lapse rates based on the seasonal average values computed over the different seasons of the year (premonsoon, monsoon, postmonsoon, summer, winter) based on statistical analysis or approaches (Kattel et al., 2013; Immerzeel et al., 2014).

Monthly Fixed Value

In practice, researchers base the temperature lapse rate values fixed over different monthly values on the regression between temperature and elevation (Kattel et

al., 2015; Zhang et al., 2015) but in reality, the temperature lapse rate cannot be fixed based on month.

Observation elevation interpolation

In many studies, the temperature lapse rate is derived from the extrapolation of temperature records obtained at various meteorological stations (Heynen et al., 2016; Marshall et al., 2007; Shrestha et al., 2015; Valéry et al., 2010). However, such extrapolation is unable to express local variability, as these stations are sparely located at lower elevations (the bottom of valleys) and are difficult to establish and access at remote altitudes (the mountain peaks).

Over the past few years, multiple studies (Blandford et al., 2008; Harlow et al., 2004; Kattel et al., 2013; Marshall et al., 2007; Minder, Mote, & Lundquist, 2010; Rolland, 2003) have pointed out the lapse rate of temperature is a function of energy balance regimes such as elevation, surface conditions, air moisture content, radiative conditions, vegetation patterns, wind, and cloud availability. Despite the fundamental importance of the spatial variability of temperature, such assumptions lead to large uncertainties in model simulations regarding rainfall, snowfall, and snowmelt contributions (Minder et al., 2010). The near-surface mountain air temperature is, therefore, considerably different from that of free air, and temperature gradients are generally non-static (Heynen et al., 2016) and nonlinear, subjected to water vapor content.

Table 2.1. Summary of Relevant Recent Studies Based on the Temperature Lapse Rate and their Limitations

Relevant Studies	Major Contributions	Limitations
Tahir et al. (2011)	Modeled snowmelt runoff in a high-altitude river catchment using snow runoff model based on a degree day conceptual approach	Lapse rate value of -0.0048K/m for lower areas and -0.0076K/m for higher elevations
Immerzeel et al. (2012)	Corrected precipitation time series using different degree day factors (DDFs) as a conceptual approach	Daily temperatures at the station were converted to sea level temperatures by using a lapse rate of -0.0068K/m
Sixto et al. (2012)	Snow cover modeling using water and energy budget based distributed hydrological modeling system	JRA-25 temperature dataset was used with correction and a constant lapse rate of -0.0065K/m
Immerzeel et al. (2014)	Improved understanding of temperature and precipitation variability's strong elevation dependency	Application of seasonal lapse rates -0.0046K/m (monsoon), -0.0058K/m (winter), -0.0064K/m (premonsoon), -0.0049K/m (postmonsoon)
Tennant et al.(2015)	Assessment of elevation dependent streamflow responses with a stratified gauging network and spatially distributed climate product	Application to a wide range of basins for to estimate the change in snowline for anticipated alterations in streamflows.
Zhang et al. (2015)	Modeled snow cover and runoff in high mountain catchments with scarce data based on critical snowfall temperature	Temperature lapse rate values were estimated on the basis of historical observations, monthly temperature lapse rate varying from (from -0.003 to -0.0062) K/m
Shrestha et al. (2015)	Integrated a system for snow and glacier melt using a water and energy budget based DHM	Application of variable lapse rates (from -0.0023 to -0.0092) K/m from observation stations much lower than the basin's maximum elevation
Thayyen & Dimri (2016)	Evaluation of the variation in slope environmental lapse rate in the Himalaya and proposed modeling for the valley scale slope environmental lapse rate	Monthly lapse rate indices were calculated based on previous observations and atmospheric reanalysis

2.4. Implications of data from other models

Atmospheric state variables can be obtained from general circulation models (GCMs), regional climate models (RCMs), numerical weather predictions (NWPs), and atmospheric reanalysis with relatively coarser resolution. Weather radars observations, satellite observations, NWPs, Reanalysis products, GCMs, and RCMs are sources providing the distributed temporal and spatial distributions of various metrological parameters, of which the most important and crucial are precipitation and temperature. The accuracy for quantified of rainfall or snowfall estimates from these sources or products is still questionable but can provide continuous evolutionary spatial information with reasonable temporal frequency. Precipitation estimates obtained from satellites are also becoming popular due to spatial and temporal availability. Temperature observations from stations are sparse and few are available from higher elevations in mountainous areas (Cao et al. 2017). Alternatively, gridded (NWP, reanalysis, RCMs, and GCMs) outputs are available with coarse resolution (10 -100 km) but observational data assimilation accuracy of these modeling systems is questionable. The lower availability of observational data assimilations directly influences the quality of products (Whitaker et al. 2009) due to which significant bias exists.

Estimates obtained through these sources are unable to provide realistic absolute values due to uncertainties regarding the improper representation of topography and the lack of subgrid parameterization for smaller scale processes and surface characteristics (Dimri, 2014). Due to their significant biases, data from atmospheric reanalysis and/or atmospheric models are not frequently used to simulate the hydrological response at a basin scale. However, due to the integration of dynamical equations and model physics (Grell et al., 1994; Roe, 2005) these models have robust potential in developing 3-D

distribution/profiles. Meteorological observations are the most preferred option for basin-scale hydrological applications. Despite the highest level of confidence in meteorological records from the representative stations, they largely contain sparse data, limited in number and unable to generate realistic 3-D distribution/profiles of meteorological parameters.

3. Methodology for an Integrated Hydrological Modeling Framework

3.1. Introduction

In this chapter the modeling strategy and components of the integrated hydrological modeling framework are explained in detail. The purpose of this chapter is to present a distributed hydrological framework for quantification of rainfall and snowfall. So far, it has been demonstrated that point observations/meteorological stations are considered ground truth but are limited and sparse. For precipitation, weather radars and satellite products are considered adequate replacements for observed data of course, with some bias, but much less than that of reanalysis data, NWPs, RCMs, and GCMs. Moreover, all of these alternate sources are able to capture the spatial pattern much more accurately than interpolation methods adopted to convert the point data into distributed information.

3.2. Modeling Strategy

We have proposed a conceptual framework to devise an integrated system capable of reproducing the hydrological response. The main components of this framework are presented in Figure 3.1 whereas the detailed flow chart diagram is presented in Figure 3.2 following the mail components of the research. For ease of understanding, the framework can be divided into four major components.

1. Preparation of inputs for precipitation and temperature datasets including VPT and dynamic lapse rate data, in addition to other forcing and static data
2. Classification of precipitation into rainfall and snowfall
3. Spatiotemporal bias correction of rainfall
4. Spatiotemporal bias correction of snowfall in the distributed hydrologic modeling framework.

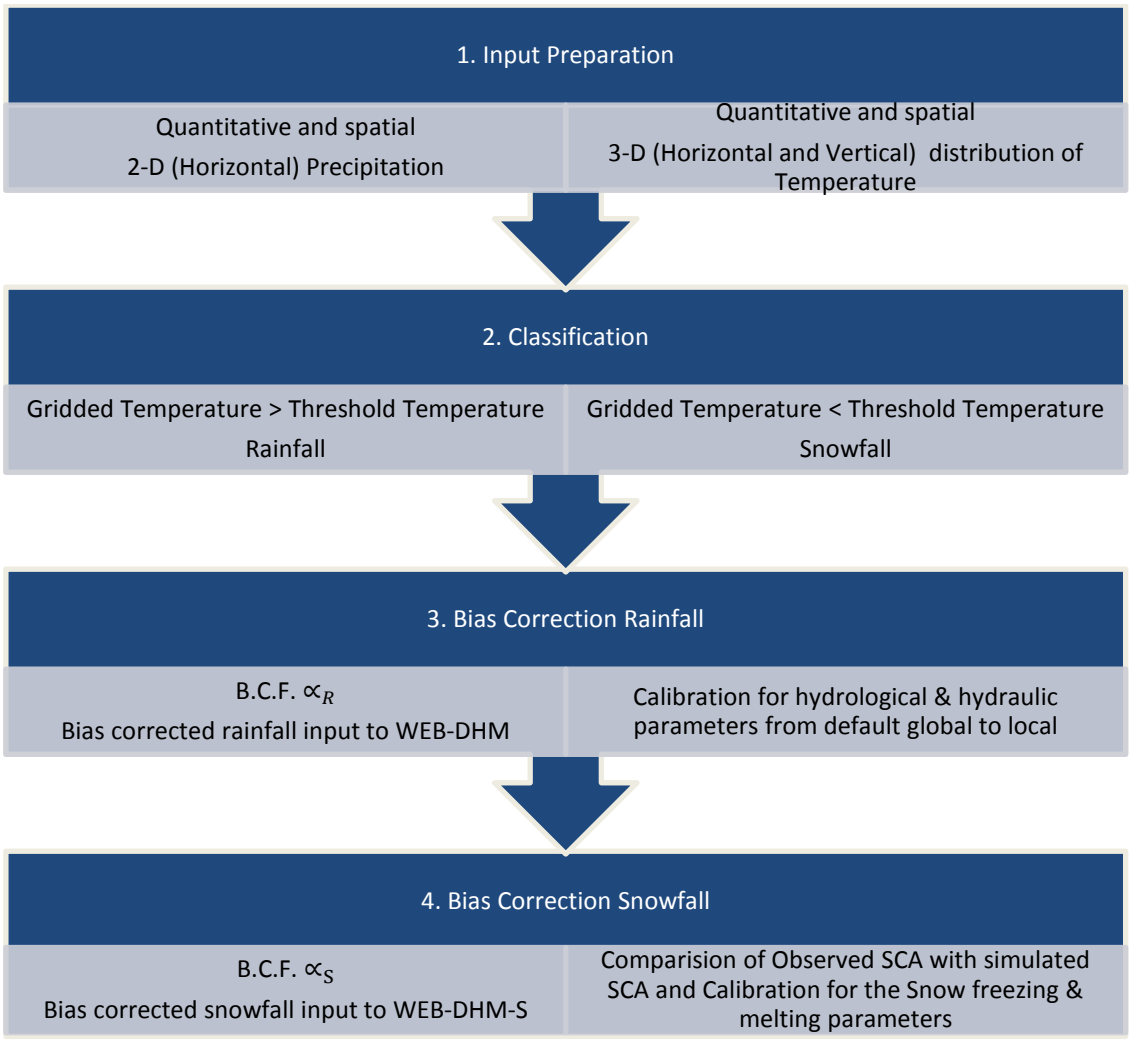

Figure 3.1. Flow Chart for the Main Components of Research Framework

This framework has three cycles of tuning loops (C1, C2 and C3) enclosed in circles, as shown in Figure 3.2**,** to establish a logical and step-by-step calibration procedure. One calibration loop is for the static input parameters and other two loops are associated with snowfall and its spatial distribution. The details of each step are explained in the following sections for more detailed insight and understanding.

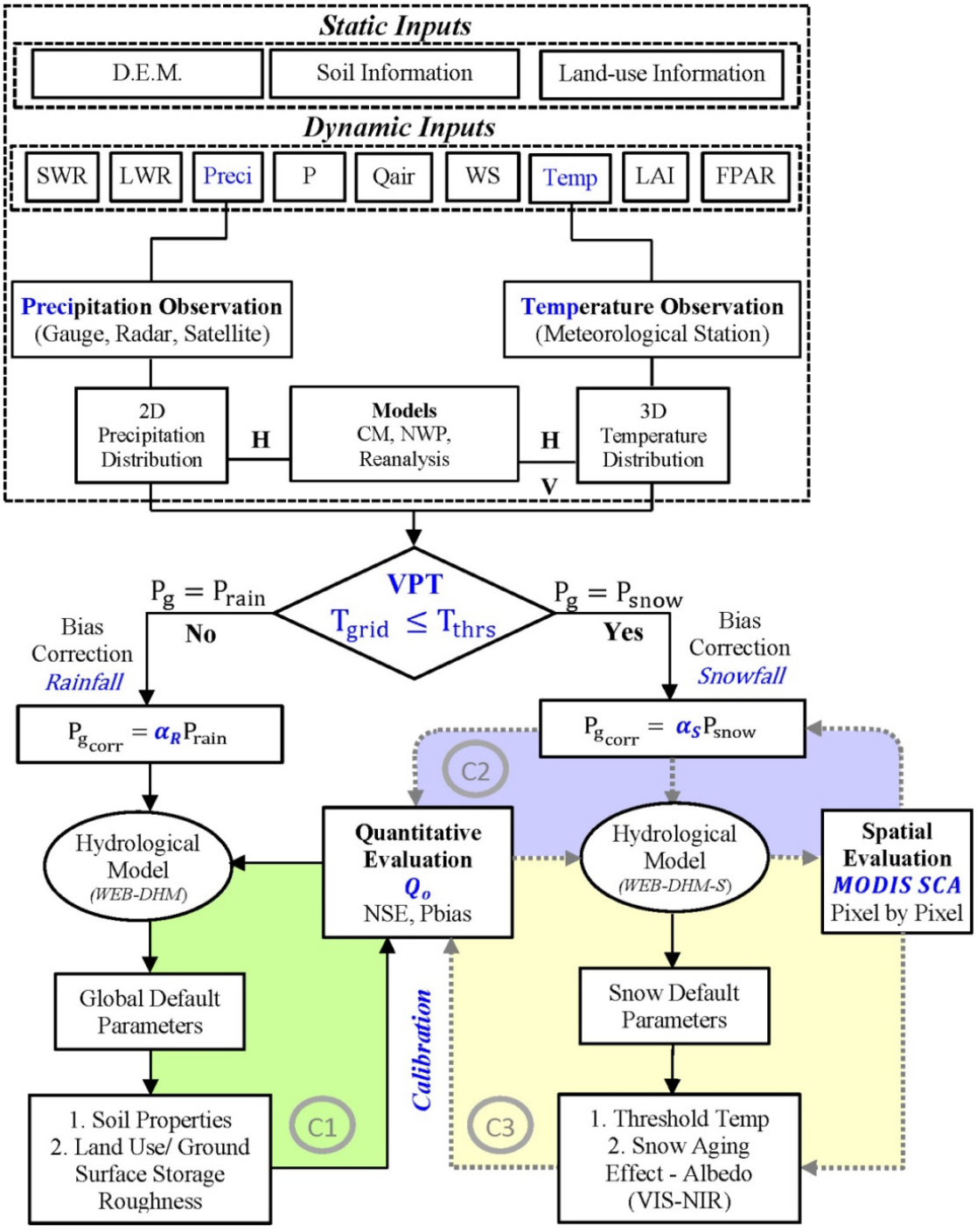

Figure 3.2. Methodology (Conceptual Framework) for Integrated Hydrological Modeling

3.2.1. Input Preparation

The first step is associated with the preparation of the required inputs by physically based DHM. Broadly, the inputs can be classified as static data and dynamic forcing. The static inputs are unchanging for specific areas of interest and include the digital elevation model (DEM) and soil and land-use information. On the other hand, the dynamic inputs change with respect to time and space and include dynamic vegetation data for the leaf area index (LAI) and the fraction of photosynthetically active radiation (FPAR), and meteorological forces such as long-wave radiation (LWR), short-wave radiation (SWR), precipitation (Preci), air temperature (Temp), relative air humidity (Qair), pressure (P), and wind speed (WS). Based on the significance of precipitation (Preci) and air temperature (Tair) data in snow-fed mountainous regions, an effort is made to merge the benefits and minimize the shortcomings of different sources, in this framework, especially for precipitation (Preci) and air temperature (Tair). The sources for observed precipitation datasets are meteorological stations, weather radar, and satellite products. Likewise, the sources for temperature are meteorological stations, weather balloons/radiosondes and satellite products. Alternatively, atmospheric reanalysis, NWPs, RCMs, and GCMs also provide various spatiotemporal distributions of precipitation and temperature. Accordingly, the 3-D temperature profile (VPT) and 2-D precipitation distribution are prepared in this step.

3.2.2. Temperature based classification

As temperature is the prime variable for splitting the precipitation phase into rainfall and snowfall, the developed VPT holds the information for change in air temperature (Temp) with respect to elevation. By defining a threshold/critical

temperature value for the temperature and using VPT with precipitation, such bifurcation is achieved in the second step.

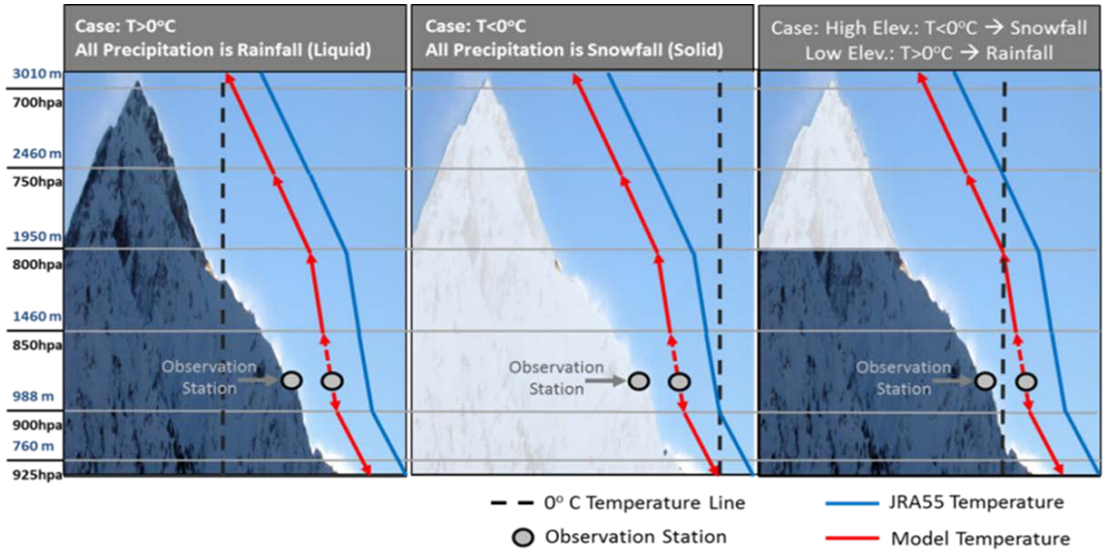

Figure 3.3. Integrated role of vertical temperature profile and Threshold Air Temperature

3.2.3. Spatiotemporal bias correction for rainfall

After the bifurcation we sort out the summer and winter season based on air temperature throughout the basin elevation. The period with air temperature at all the basin elevations above the threshold temperature, is considered to be the summer season, with the primary precipitation being rainfall. For this period, quantitative analysis of rainfall is performed by using available in-situ data and/or the weather radar rainfall and/or the satellite product. In the case that only one of these is available, various other model outputs from atmospheric reanalysis, NWPs, RCMs, and GCMs can also be used. The in-situ rainfall in an irregular network of meteorological stations is converted to a gridded spatially distributed product by interpolation. Unfortunately, none of the interpolation methods stand out as superior to the others in providing realistic and actual spatial distribution patterns, as they are primarily subjective to the

data and its quality issues (Hofstra, Haylock, New, Jones, & Frei, 2008). However, the spatial patterns can also be obtained for observational sources like weather radar and satellites in addition to atmospheric reanalysis, NWPs, RCMs, and GCMs products. Based on quantitative analysis between observed rainfall from gauges and radar, a bias correction factor (BCF) for rainfall is calculated as (α_R), and then the corrected radar rainfall is used to simulate the discharge as the hydrological response using a physically based DHM with water and energy budget to simulate the snow processes effectively. The static inputs include the spatial information for soil and land-use properties of watershed. These properties have direct implications for rainfall in establishing surface and subsurface flow. If the local datasets for the static inputs such as soil characteristics and land-use are not available, global datasets can serve the same purpose. Due to limitations in the availability of local spatially distributed datasets, the global datasets can fulfill the requirements with probable uncertainties in output results. It is difficult to find exact soil properties and land-use information from global datasets therefore, adjustments are requisite based on the evaluation of simulated outputs using statistical methods (NSE, PBIAS). The calibration loop (C1) is therefore introduced in the framework to deal with adjustments in global datasets by modifying the soil and land-use information. Based on findings from calibration loop (C1), the static parameters are then kept fixed.

3.2.4. Spatiotemporal bias correction for snowfall

Finally, we move toward a spatiotemporal bias correction for the snow based on the quantitative and spatial analysis. Unlike rainfall only quantitative analysis of precipitation is not enough, as the snow cover extent is evidence for the spatial distribution of snowfall. The BCF for winter season (α_S) depends on both, the

quantitative analysis of the precipitation and spatial distribution of snow over the watershed. In addition to statistical methods (NSE, PBAIS) for tuning the discharge the indices for the pixel-by-pixel analysis are also introduced for evaluation of the spatial distribution of snow in the winter season. The simulated discharges and snow cover are compared with observed discharge and Moderate Resolution Imaging Spectroradiometer (MODIS) Terra satellite 8-day composite maximum snow extents (MOD10A2). For facilitating the decision for the BCF for the winter (α_S), a calibration loop (C2) is introduced in the framework. Different parameters related to accumulation/ablation of snow include the threshold temperature and snow aging controlled by the visible (VIS) and near infrared (NIR) albedo. These parameters are set initially to some default values to initiate the modeling process and can be adjusted if necessary. To address these snow default parameters, an additional calibration loop (C3) is introduced to obtain the optimal result on discharge and snow cover.

4. Study Area and Model Selection

4.1. Introduction

To implement the applicability of the conceptual framework proposed in the previous chapter, we basically need to define the study area and select most appropriate model. First of all, the study area will be discussed in detail followed by a detailed discussion about the model selection criteria and description of the selected model to provide understanding and to illustrate the applicability of hydrological framework in snow-fed mountain regions. The model selection criteria are based on the capability of a model to not only regenerate the discharges but also reproduce the snow cover extents, especially on mountainous region established on rainfall and snowfall classification at the same time based on the existing temperature at various elevations.

4.2. Study Area

To implement the applicability of this proposed framework, we primarily need to select a suitable mountainous watershed as the study area with seasonal snow-cover and the most appropriate model. The selected study area is located in the Akaishi Mountains of Shizuoka Prefecture in the Honshu Island of Japan, comprising of the northern part of the Oi River Basin (Figure 4.1a). A smaller portion of the basin lies in the Yamanashi and Nagano Prefectures, mainly consisting of mountains above 2,000 m (40%) with elevation ranging from 929 m to 3,110 m (Figure 4.1b). The basin climate is wet and humid with heavy snowfall in winter from December to March and a summer season from June to September with no snowfall. The annual average precipitation over the year is 3,000 mm/year. There are several check dams in the Hata-I basin, namely Akaishi Dam (1,140m), Tokusa Dam (1,210m) and Nikengoya (1,450m). Nearly half of this watershed is comprised of high mountains (with elevation greater than 2,000 m)

therefore, entire watershed is covered with snow in mid-winter and there is no snow in the summer season.

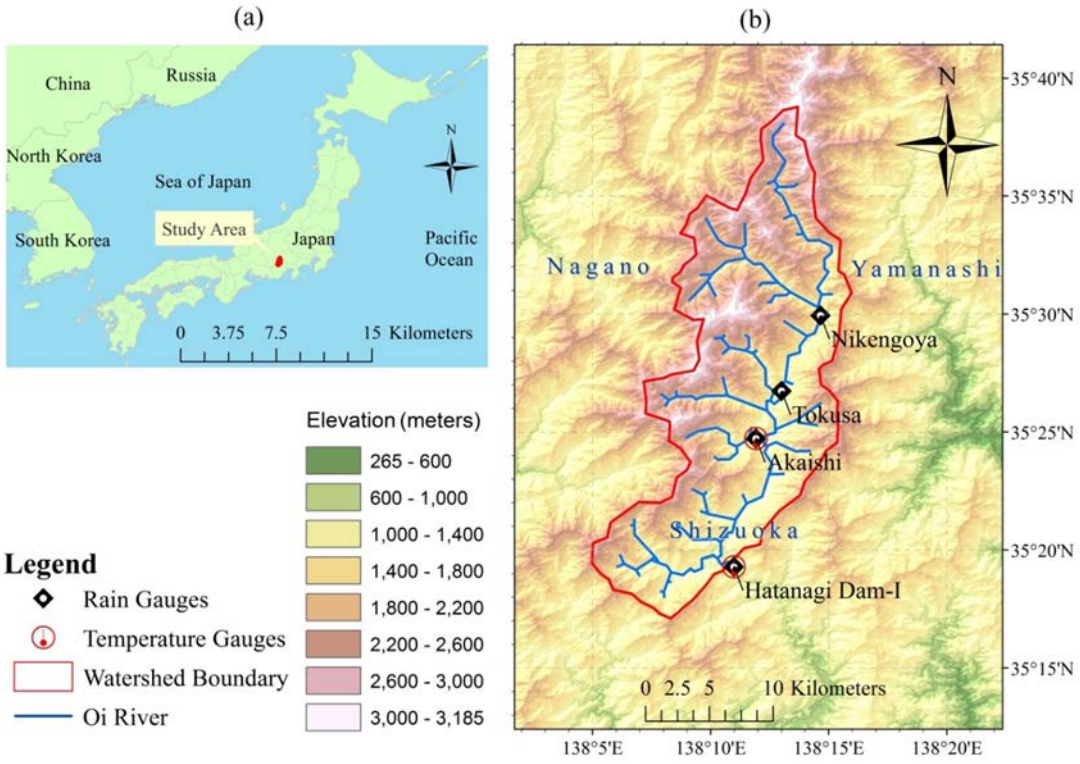

Figure 4.1. (a) Location of the study area in Japan (b) Hatanagi Dam-I Basin in Shizuoka Prefecture in between Nagano and Yamanashi Prefecture with four meteorological stations for rain gauges and two stations with temperature records

4.3. Model Selection Criteria

Earlier, the hydrological models were unable to provide a correct estimate for the evapotranspiration and they also need the pan evaporation data for their application to the semiarid regions. Moreover, these models were not capable of being coupled directly to atmospheric reanalysis, NWPs, RCMs, and GCMs. In the past, the problems for obtaining the distributed information for the dynamic hydrological modeling datasets such as precipitation, temperature, wind speed, humidity, long-wave radiations

and short-wave radiation and dynamic vegetation forcing emerged as the biggest hurdle for using the distributed hydrological modeling. The additional problems faced by the distributed hydrological modeling were the incorrect estimate of water and energy fluxes due to a wide gap in hydrological models and atmospheric models. Hydrological modeling is becoming more sophisticated with the passage of time and new developments in the field of computer sciences. Growth in computational power and improvement in understanding of hydrological processes have changed the modeling trend from lumped conceptual models to more sophisticated physically based distributed hydrological models (Troin et al., 2015). The modeling of seasonally snow-covered mountain basins, considering processes such as snow accumulation, ablation, and snowmelt runoff, can be physically described using DHMs with a multilayer energy balance scheme (Shrestha et al. 2010).

Therefore, the selection criterion is based on the selection of the DHM not only with water budget but to deal with snow processes based on multilayer energy balance scheme. Moreover, the ease coupling with atmospheric reanalysis, NWPs, RCMs, and GCMs and available satellite product outputs with DHM is critically important.

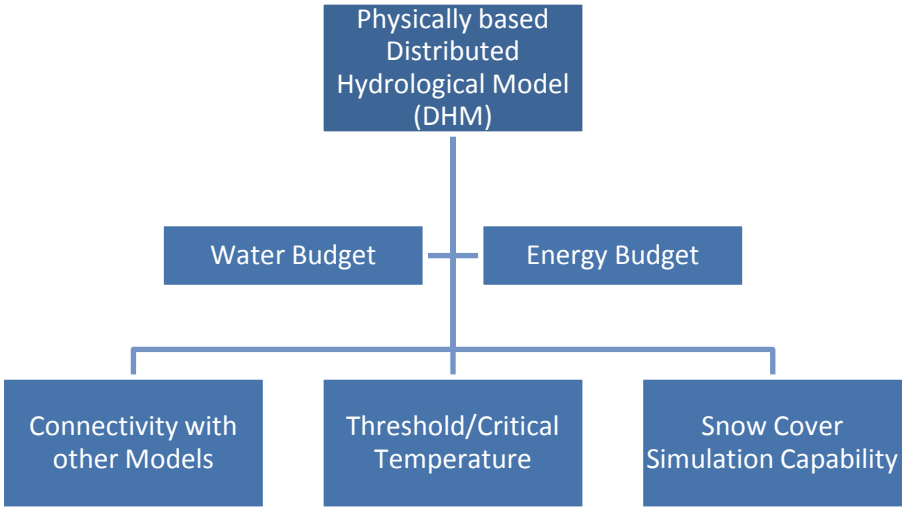

Figure 4.2. Hierarchy for the Distributed Hydrological Model Selection

The uncertainties in modeling the mountain hydrology are strongly associated with temperature distribution. The temperature has most substantial influence for precipitation amount, pattern (rain or snow) and spatial distribution especially in case of snowfall.

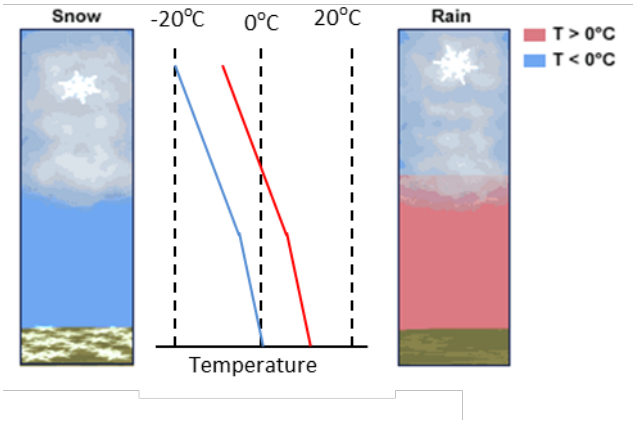

Figure 4.3. Classification into rainfall and snowfall based on the threshold temperature

Many of the previous studies used for the simulation of snowmelt runoff used the remote sensing information but these data were unable to predict snowmelt and snow cover in the future (Immerzeel et al., 2009; Xiaowen Li, Gao, Wang, & Strahler, 2001;

Rango, Salomonson, & Foster, 1977; Singh & Jain, 2003). Therefore, the selected model is required to have the simulation capability for simulating snow cover information.

4.4. Model Inter-comparison

Multiple attempts have been made for developing effective modeling system of runoff routing depending on the snow hydrological process based on ground and snow temperatures, soil and snow layer schemes and canopy soil process using DHMs. Some of the DHMs such as the Utah Energy Balance Distributed Snow Model (UEB-DSM), ISNOBAL and SnowMOD have advantages for better simulating the snow process better but were unable to simulate runoff routing (Tarboton et al., 1996; Garen & Marks, 2005). On the other hand, many schemes, despite the ability to simulate the runoff due to water balance approach but were lacking in energy balance schemes and also considered snow temperature and as bulk, such as the Distributed Hydrology Soils Vegetation Model (DHSVM), Variable Infiltration Capacity (VIC), WATCLASS, Distributed Biosphere Hydrological Model (DBHM), Cold Region Hydrological Model (CRHM), and Geo-TOP (Liang et al., 1994; Wigmosta et al., 1994; Storck et al., 1998; Cherkauer et al., 2003; Zanotti et al., 2004; Soulis et al., 2005; Pomeroy et al., 2007) The simulation for snow surface temperature and the melting of snow on a temporal and quantitative basis were unable to represent the diurnal freezing and thawing cycles due to the single snow layer energy balance approach (Jin et al., 1999; Sun et al., 1999; Slater et al., 2001; Luo et al., 2003). However, the three-layer snow scheme was found to be the best alternate to simulate the snow processes more precisely (Jin et al., 1999; Shreshta, 2012; Sun et al., 1999). Wang (2007) brought together the geomorphology-based hydrological model (GBHM) and improved land surface model (LSM)

incorporating sparse canopy processes and the transfer of turbulent fluxes, known as the Simple Biosphere scheme 2 (SiB2) (Sellers et al., 1996) and model was called the water energy budget based distributed hydrological model (WEB-DHM). The main theme behind the development of Water Energy budget based distributed hydrological model was to obtain the improved streamflow simulation ability by bridging the gap between the hydrological models and atmospheric models and to produce reliable estimates for the water and energy fluxes.

Further improvements were made in the snow physics for WEB-DHM by embedding the three-layer energy balance snow scheme of the Simplified Simple Biosphere Scheme 3 (SSiB3) (Xue, Shufen, Daniel, & Jiao, 2003) and the Biosphere Atmosphere Transfer Scheme (BATS) (Dickinson, Henderson-Sellers, & Kennedy, 1993). To simulate the basin scale simulation and ablation processes more realistically, coupling the snow-soil-vegetation atmosphere transfer scheme with the multilayer energy balance snow scheme and parameterization of albedo as a prognostic state variable is critical. The SSiB3 with three-layer snow scheme and the BATS with albedo as prognostic state variable were used with WEB-DHM to improve the snow physics. This made WEB-DHM more accurate for simulating the snow processes in cold regions as well and due to these improvements it is known as WEB-DHM-S. The structure of the WEB-DHM-S is shown in Figure 4.5 with the elaboration of different processes.

Table 4.1. Inter-comparison of different Distributed Hydrological Models (DHMs)

Model	Year	Runoff Routing	Soil Temp	Soil Moisture	Snow Layers	Canopy Snow Process	Snow Temp	Glaciers
DHSVM	1994	O	O	O	2	O	O	X
VIC	1994	O	O	O	2	O	O	X
UEB-DSM	1999	X	B	X	1	X	B	X
WATCLASS	2000	O	X	O	2	O	B	X
ISNOBAL	2005	X	B	X	1	X	O	X
DBHM	2005	O	X	O	1	O	B	X
SnowMOD	2006	X	B	X	1	O	B	X
CRHM	2007	O	X	O	5	O	B	X
Geo-TOP	2007	O	O	O	1	X	B	X
WEB-DHM	2007	O	B	O	1	O	B	X
WEB-DHM-S	2012	O	O	O	3	O	O	O

O = Yes, X = No, B = Bulk

Where,

Distributed Hydrology Soils Vegetation Model (DHSVM)	Wigmosta et al. (1994); Storck (1999)
Variable Infiltration Capacity (VIC)	Liang et al. (1994),Cherkauer et al. (2003)
Utah Energy Balance (UEB) – Distributed snow model	Tarboton and Luce (1999)
Waterloo-Canadian Land Surface Scheme (WATCLASS)	Soulis et al. (2000, 2002)
Coupled Energy and Mass Balance Model (ISNOBAL)	Garen and Marks (2005)
Distributed Biosphere Hydrological Model (DBHM)	Tang (2006) SiB2 - LSM
Snowmelt Model (SnowMOD)	Liston et al. (2006)
Cold Region Hydrological Model (CRHM)	Pomeroy et al. (2007)
Geo-TOP: Coupled Water and Energy Budgets Hydrological Model	Zanotti (2007)
Water and Energy Budgetbased Distributed Hydrological Model (WEB-DHM)	Wang et al. (2007; 2009a,b) SiB2-LSM
WEB-DHM with improved snow and glacier physics(WEB-DHM-S)	Shrestha et al.(2012) SiB2/SSiB3/BATS-LSM

As WEB-DHM/WEB-DHM-S is a fully physical based model with improved capabilities to simulate the snow/ice process based on 3 layer snow scheme and can be coupled with other models, this study will include it as a core model.

4.5. Model Description and Structure

The overall model structure of WEB-DHM can be easily explained through Figure 4.4 as shown below.

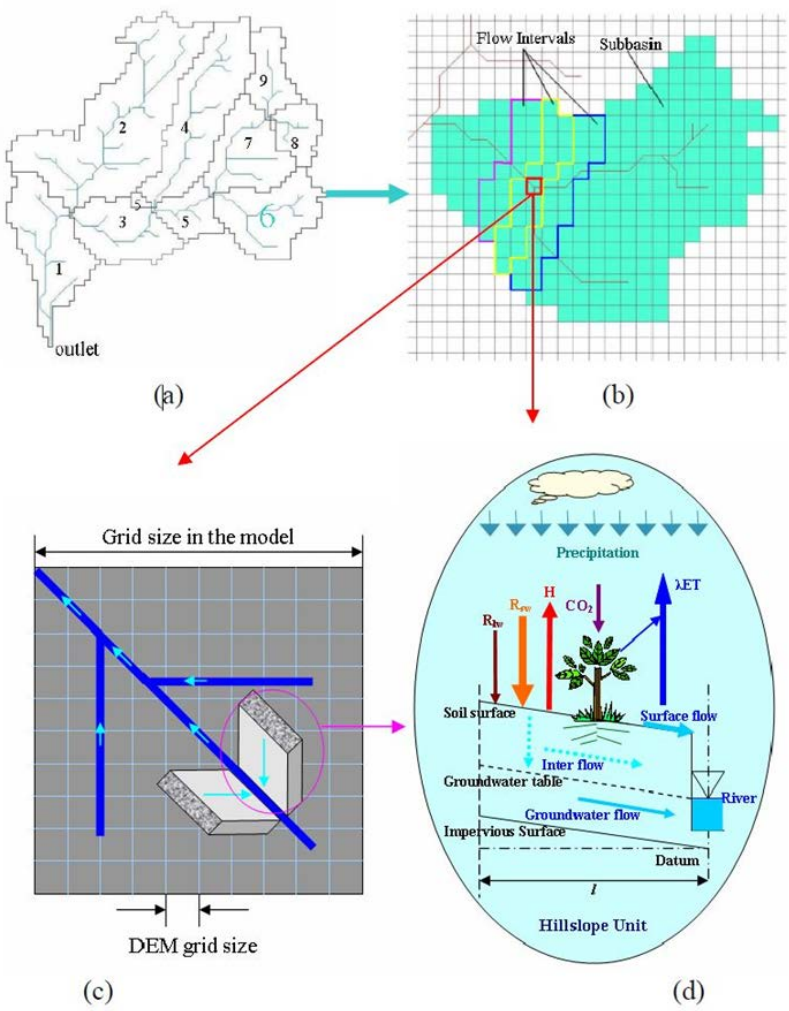

Figure 4.4. Structure of WEB-DHM (a) Basin Delineation and Sub-Basins (b) Sub-Basin to flow interval within multiple model grids (c) Basic Hydraulic Unit BHU (d) Water and Energy balance from atmosphere to river (for details see Wang et al., 2009)

The model physically addressed all the hydrological processes occurring with considerable attention toward snow hydrology. The mountain or the snow hydrology in this water energy budget system was improved later on due to its potential application for flood, droughts and the water resource management from point scale to continental scale. Although the model was capable of simulating the hydrological processes in different climates, the single snow layers scheme and constant albedo in SiB2 were required to be prognostic physical variables.

4.6. Development of WEB-DHM-S

The simulation for snow surface temperature and the melting of snow on temporal and quantitative basis were unable to represent the diurnal freezing and thawing cycles due to the single snow layer energy balance approach (Jin et al., 1999; Sun et al., 1999). However, the three-layer snow scheme was found to be the best alternate to simulate the snow processes more precisely (Shrestha, Wang, & Koike, 2010; Xue et al., 2003). In order to simulate the basin scale simulation and ablation processes, a more realistic approach was required for improved snow physics. This could be achieved by coupling the snow-soil-vegetation atmosphere transfer scheme based distributed hydrological model with the multilayer energy balance snow scheme and parameterization of albedo as a prognostic state variable.

For the development of a DHM with such a land surface scheme including multilayer snow energy balance approach with some glacier melt approach was critically important. The SSiB3 with the three-layer snow scheme and the BATS with albedo as the prognostic state variable were used with WEB-DHM to improve the snow physics. This made WEB-DHM more accurate for simulating the snow processes in

cold regions as well and due to these improvements it is known as WEB-DHM-S (Figure 4.5).

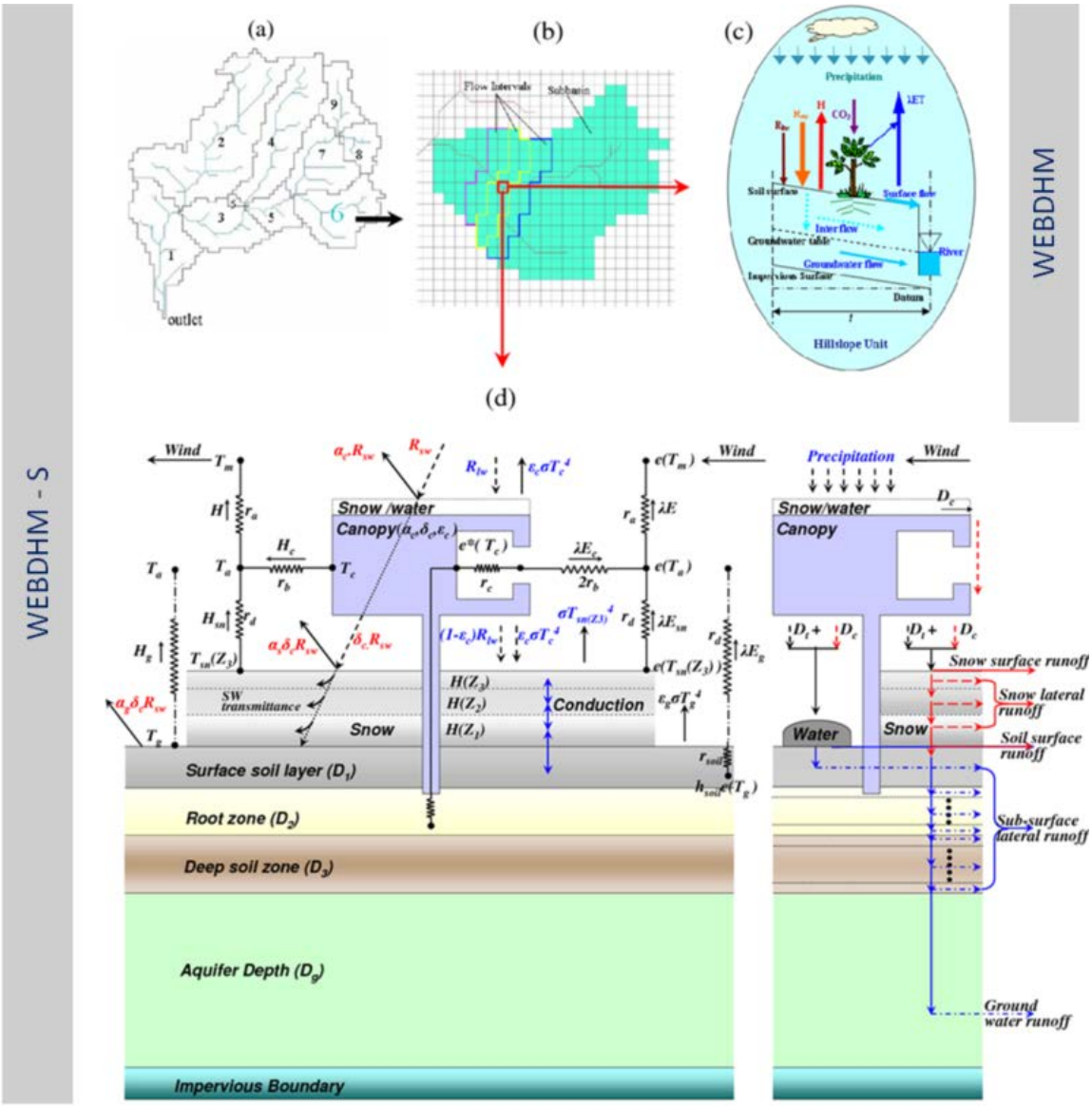

Figure 4.5. Structure of Improved WEB-DHM with snow physics (a) Basin Delineation and Sub-Basins using Pfafstetters (b) Sub-Basin to flow interval within multiple model grids (c) Water and Energy balance from atmosphere to river (d) detailed description of the three layer snow energy balance model (for details see Shrestha et al., 2012)

Due to these improvements in the model, first of all, a snow pack is divided into three layers with different thicknesses but identical initial snow temperatures. The topmost layer has a minimum and fixed thickness of 2 cm. By incorporating the radiation budget and sensible and latent heat fluxes, a surface energy balance equation is formulated only for the topmost layer with minimum thickness. The middle one has a higher thickness with a maximum value of 20 cm in order to deal with diurnal changes in snow. Heat conduction and penetrating downward shortwave radiations are used to control the heat budget. After fixing the thickness for first and middle layer, last layer thickness varies and has the same mechanism for controlling the heat budget initially. With the passage of time all of these three layers have different mechanisms because of their own individual energy budget and heat exchanges between them. The parameterization of snow cover surface albedo by application of physically based prognostic snow albedo from BATS (Dickinson et al., 1993). With the improvement of snow physics there were significant changes for the various snow processes such as snow layers, density, depth, thermal conductivity, radiation transmission, albedo, surface and snow temperatures, and the fraction of snow cover. A brief comparison of these improved processes is shown in the following Table 4.2.

Table 4.2. WEB-DHM versus WEB-DHM-S processes

Process Description	**WEB-DHM (After Wang et al., 2009)**	**WEB-DHM-S (After Shrestha et al., 2012)**
Snow Processes		
Snow Layers	Single	Three
Snow Density	Constant 200kg/m	Prognostic
Snow Depth	Empirical (5 times)	Prognostic
Snow Thermal Conductivity	Similar to soil	Depends on Snow Density
Snow water/ice Contents	No	Yes
Snow Albedo	Initially constant decreases with melting	Prognostic Considers age effect and solar zenith angle
Snow Surface Temperature	Average temperature of bulk layer	Different temperature of soil
Snow Cover Fraction	Linear function of snow depth	Function of snow depth and density
Other Processes		
SW Radiation Transmission	No	Transmission into soil layers
Surface Energy Fluxes	Applied to bulk layer	Applied top layer
Ground Surface Temperature	Dreadorff (1978) – single layer	Heat Conduction b/w soil and bottom snow layer

5. Data Integration for Vertical Profile of Temperature

5.1. Introduction

The relationship between the temperature and altitude and the variability of the temperature distribution determines where precipitation falls as snow or rain. As we have discussed, there are different approaches for the application of lapse rate of temperature in Chapter 2, such as constant fixed value (CFV), seasonal fixed value (SFV), monthly fixed value (MFV) and observation elevation interpolation (OEI). None of these approaches provide realistic and true variation of temperatures along the altitude. This chapter is about the development of vertical profile for temperature (VPT) introduced as the more realistic dynamic lapse rate instead of any approximation. This chapter describes how different sources of data are integrated to produce reliable temporal and spatial distribution of temperature within the basin. Before its application to simulate the hydrological response of the watershed, the reproduced dataset is validated. For the development we need to have temperature data records for at-least two stations. Firstly, we have to reproduce the vertical profile for temperature (VPT) data and then we need to validate the output with the other station data. For this we have considered the same study area as described in Chapter 4 (Section 4.2).

5.2. In-Situ Temperature Data

It is a ground reality that the observed temperature data are limited and sparse, and the availability of such temperature information or data is one of the biggest challenges to modeling the mountain hydrology. As described in Section 4.2.3, the daily maximum, minimum, and mean temperatures are available at two stations; Hatanagi Dam-I (950 m) and Akaishi (1,140 m)—whereas the basin elevation varies from 929 m to 3,110 m. For this basin, the available meteorological stations are unable to provide the

horizontal and vertical spatial distribution of temperature. Using a diurnal temperature trend model (Cesaraccio, Spano, Duce, & Snyder, 2001), the daily maximum and minimum temperatures at the stations were resampled to one hour (1 h).

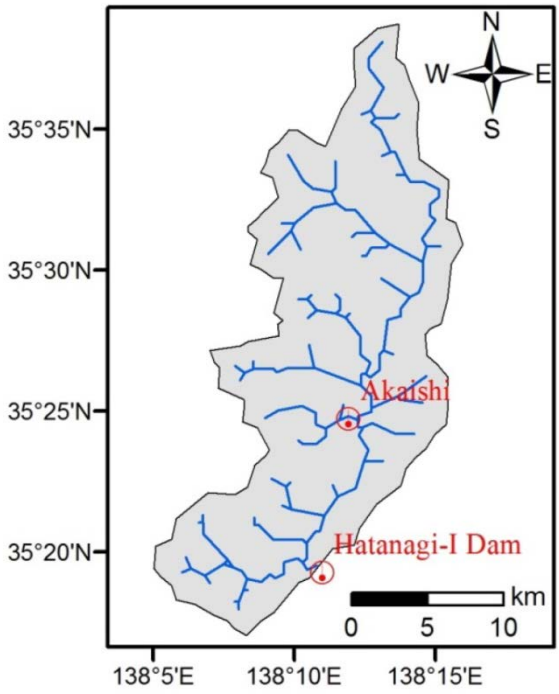

Figure 5.1. Location of temperature measurement station in study area

5.3. Japanese 55-year Reanalysis Temperature Data

The Japanese 55-year Reanalysis (JRA-55) provided by JMA is producing datasets for multiple types of metrological variables in a physically consistent and regular spatiotemporal manner (Kobayashi et al., 2015). The JRA-55 product known as isobaric analysis fields (anl_p125), captures the temperature, geopotential height, and other climatic variables at different isobaric surfaces, at six hour (6 h) temporal resolution and a spatial resolution of 1.25° latitude/longitude (JMA, 2013) as shown in the Figure 5.2. It was utilized to obtain the temperature distribution along elevation by

acquiring temperature and geopotential height data (http://search.diasjp.net/en/dataset/JRA-55).

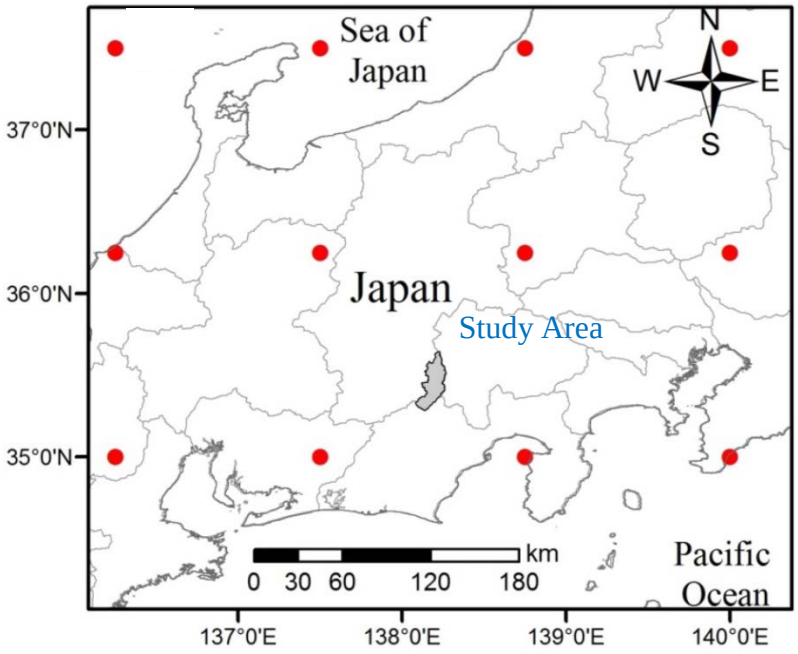

Figure 5.2. Location of study area within JRA-55 (1.25°) grid shown with red dots for temperature (K) and geopotential heights data (m) from isobaric analysis fields (*anl_p125*).

The JRA-55 assimilates the observational dataset obtained from the European Center for Medium Range Weather Forecast (ECMWF) 45-year reanalysis (ERA-40), along with Japanese observational datasets, to produce comprehensive atmospheric variability and climate change (Ebita et al., 2011; Kobayashi et al., 2015). As the JRA-55 (anl_p125) grid resolution is coarse enough (1.25°), almost all of the study area is covered within a single grid, as shown in Figure 5.2**.**

5.4. Development of Vertical Profile of Temperature

There is considerable difference between mountain air temperatures than that of the free atmosphere due to the local variability of mountainous terrain. The governing equations for the dry and moist adiabatic lapse rate of temperature are well established and are generally used in the context of air parcel lifted vertically upward under various moisture conditions (Thayyen & Dimri, 2016) and exhibit lapse rate as a function of temperature and with water vapor content as shown in equation (3).

$$\Gamma_m = \Gamma_d \left(\frac{1+\frac{L_v m_s}{R_d T}}{1+\frac{L_v^2 m_s}{C_p R_v T^2}} \right) \tag{5.1}$$

Γ_m and Γ_d are the moist and dry lapse rate of temperature respectively, L_v denotes the latent heat of vaporization (2260 kJ/kg), R_v and R_d are known as gas constants for water vapor (461 J/K kg) and dry air (287J/K kg), respectively, C_p is the heat capacity at constant pressure (1004 J/kg K), and g is acceleration due to gravity (9.8m/s^2), whereas, T is the temperature (K) and m_s is the mixing ratio of saturation.

It is worth mentioning that various atmospheric reanalyses in operations are generating reanalysis data based on in-situ data and satellite information and by utilizing mathematical and statistical algorithms. In this study, JRA-55 is used to establish the vertical distribution of temperature. Like other atmospheric reanalyses (Thayyen & Dimri, 2016), the JRA-55 is also sensitive to moisture. This sensitivity to moisture enables it to capture the gradient of temperature correctly in vertical fields. The JRA-55 product for the isobaric analysis fields “anl_p125” is comprised of 37 isobaric surfaces

from 1,000 hPa to 1 hPa for temperature and geopotential heights (Appendix 2). In order to cover the entire basin elevation, among various vertical surfaces, the temperature and geopotential height data corresponding to isobaric fields from 925 hPa to 675 hPa were downloaded from year 2013 to 2017. The six-hourly temporal resolution was resampled to one-hourly by linear interpolation. One of the meteorological stations inside the watershed (Hatanagi-I Dam: 950 m) was considered to be the reference station. Using the temperature data and geopotential heights, the VPT was constructed. Using VPT and the observed temperature records from the reference station, the temperature profile was reproduced as shown in Figure 5. It is important to mention that instead of using temperature values from JRA-55, we construct a vertical temperature profile based on the temperature estimates of this atmospheric reanalysis. A summary of the characteristics of JRA-55 (anl_p125) is provided as follows:

Table 5.1. Characteristic of Japanese Reanalysis (JRA-55) for anl_p125

Availability	1958 ~ onward	
Horizontal Grid System	Reduced Gaussian	
Horizontal grid resolution	1.25^{o}	(Ebita et al., 2011; Kobayashi et al., 2015; JMA 2013; Jones et al., 2016)
Temporal resolution	6h	
Vertical Levels	37	
Bottom level	1000 hPa	
Top level	0.1 hPa (1 hPa)	

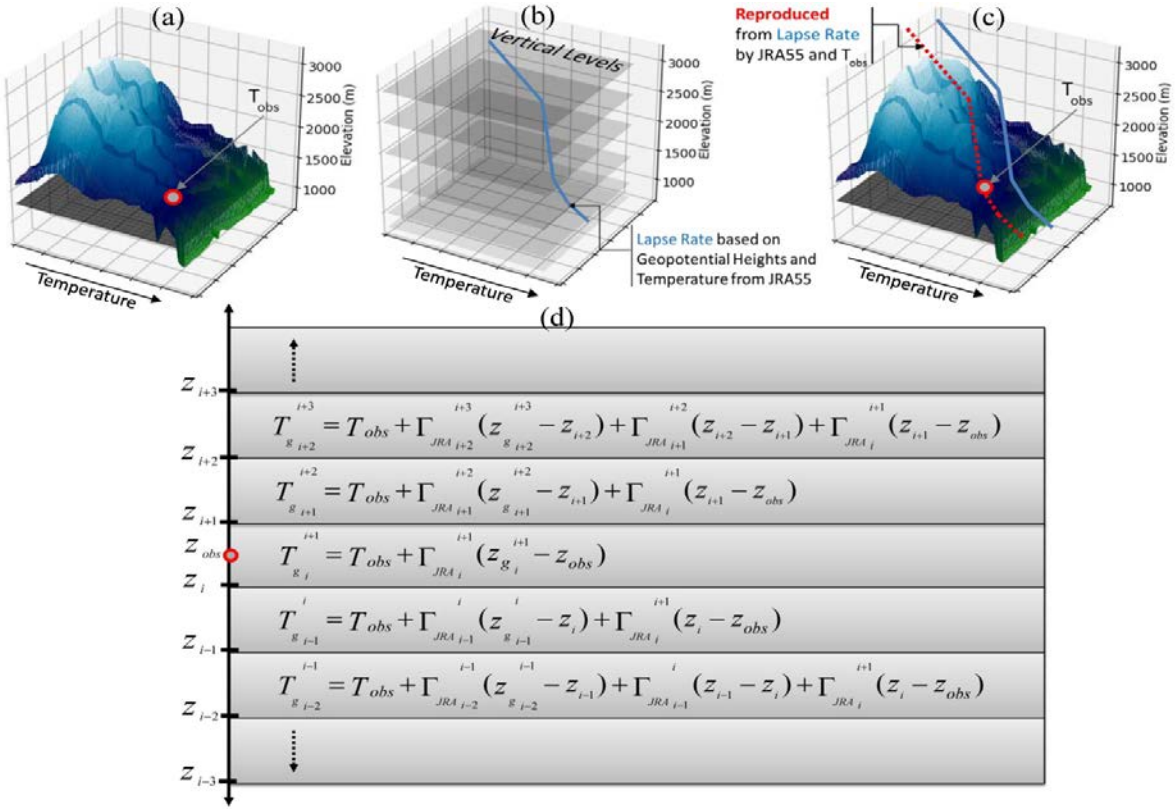

Figure 5.3. Observed temperature (T_{obs}) at reference station at elevation z_{obs} (b) lapse rate derived from temperature and geopotential heights data at each vertical level by using JRA-55 isobaric analysis fields (anl_p125) product's vertical levels ranging from 925hPa to 675hPa (c) using the temperature lapse rate obtained at (b) reproducing the temperature profile based on observed temperature at reference station at z_{obs} (d) equations for calculation of temperature at each model grid elevation by using the JRA-55 temperature lapse rate profile with observed temperature at reference station z_{obs}

where,

Γ_{JRA_i} Lapse rate from JRA-55 between two geopotential height levels (K/m) $\left(\frac{T_i - T_{i+1}}{z_{i+1} - z_i}\right)$

T_i JRA-55 temperature at i^{th} vertical level (K)

z_i Elevation of i^{th} geopotential height (m)

z_g Elevation at the model grid (m)

z_{obs} Elevation of station (Hatanagi-I: 950m) for temperature observation (m)

T_{obs} Temperature record at meteorological station (K)

T_g Temperature at Model grid from Γ_{JRA_i} and observed temperature (K)

Various snapshots for the of VPT from JRA-55 and temperature profile were reproduced from observed data and VPT-JRA-55 for different time steps in year 2014, as demonstrated in Figure 5.4. It was confirmed that the lapse rate over the mountain terrain is different from the environmental lapse rate primarily governed by the existence or nonexistence of moisture and other orographic factors. The trends for the temperature lapse rate vary not only with increase in elevation but also have discrete characteristics.

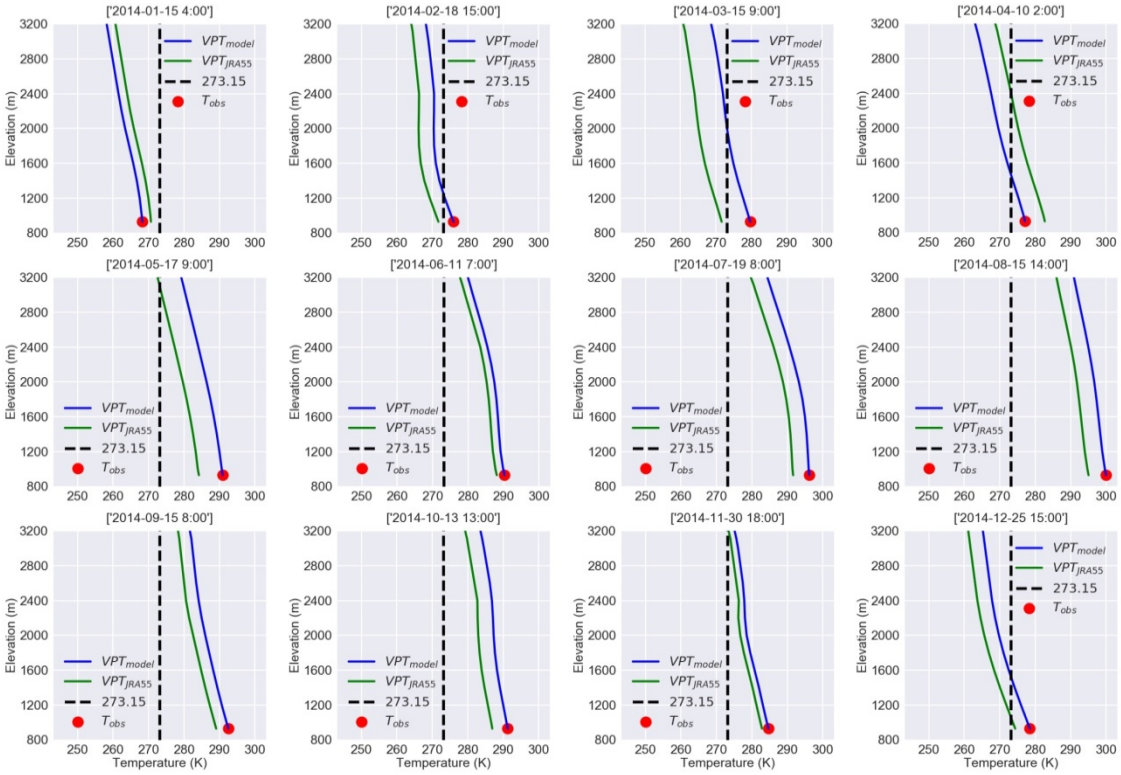

Figure 5.4. Snapshots of Vertical Profile of Temperature (VPT) showing non-static and non-linear variation in temperature along higher and lower altitudes within basin elevations (929 m to 3,110 m) at different time steps

The use of the constant values over the specific period of time or the specific month based on the past analysis results in approximations, such approximations may result in sever uncertainties which adds to the complexity in the distributed hydrological framework. The application of VPT as the dynamically active lapse rate varying spatially as well as temporally consistently based on a physical approach.

5.5. Validation of Reproduced Vertical Profile of Temperature

There are two stations for temperature measurement within the basin i.e. Hata-I (950 m) and Akaishi (1,140 m) with an elevational difference of 200 m. It was found that the mean daily temperature difference between these two stations was sometimes over 8 °C, as shown in Figure 5.5.

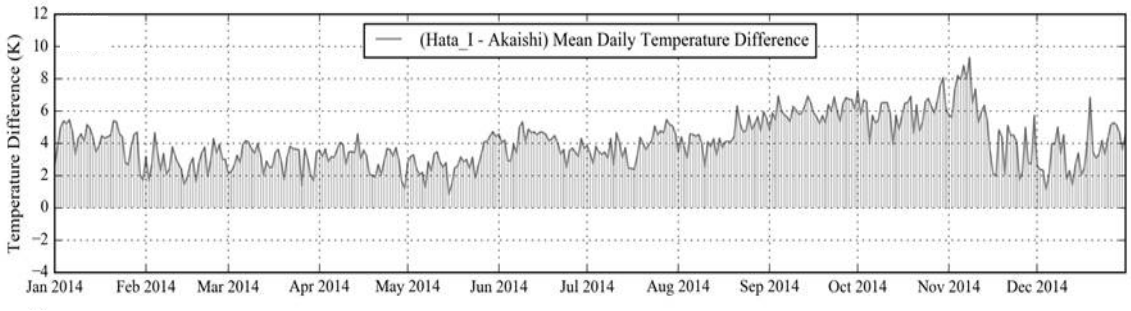

Figure 5.5. Mean daily temperature difference between observed temperatures from stations Hatanagi-I (950 m) and Akaishi (1,140 m)

With such a small elevational difference the temperature difference was considerably high; therefore, it was not used for validation purposes. On the other hand, temperature records were available at the downstream station “Ikawa Dam” (700 m) and the mean daily temperature difference between Ikawa Dam and Hata-I Dam temperatures was found to be reasonable, as shown in Figure 5.5.

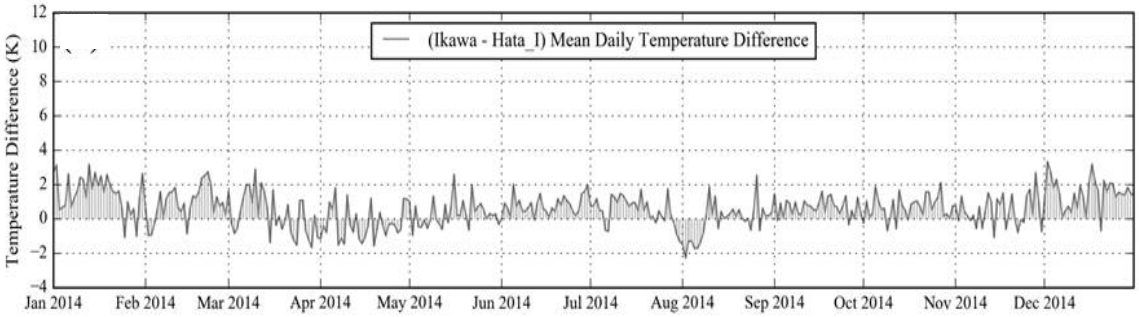

Figure 5.6. Mean daily temperature difference between observed temperatures from stations Ikawa Dam (700 m) and Hatanagi-I (950 m)

Observed temperatures at the Hatanagi-I station, along with the JRA-55 derived lapse rates, were used to reproduce the vertical profile of temperature in both upward and downward directions with respect to reference station. By extending the temperature profile toward the Ikawa Dam altitude (700 m) the reproduced temperature was plot against the observed temperature at Ikawa Dam for validation of VPT for year 2104. Figure 5.7a demonstrates the validation of VPT with minor variations in temperature depending on the availability of moisture content and radiations and other local surface processes. There is a strong correlation between the temperature observed and from VPT (R^2 value of 0.968) in Figure 5.7b. After the promising validation of the VPT reproduced from the JRA-55 geopotential heights and air temperature, it can be applied as the dynamically active lapse rate of temperature in the mountainous area. It can provide information of change in air temperature even in the remote areas where the installation of the instrument for the measurement is difficult. With the help of reference station within the mountainous watershed such VPT can be constructed and applied globally.

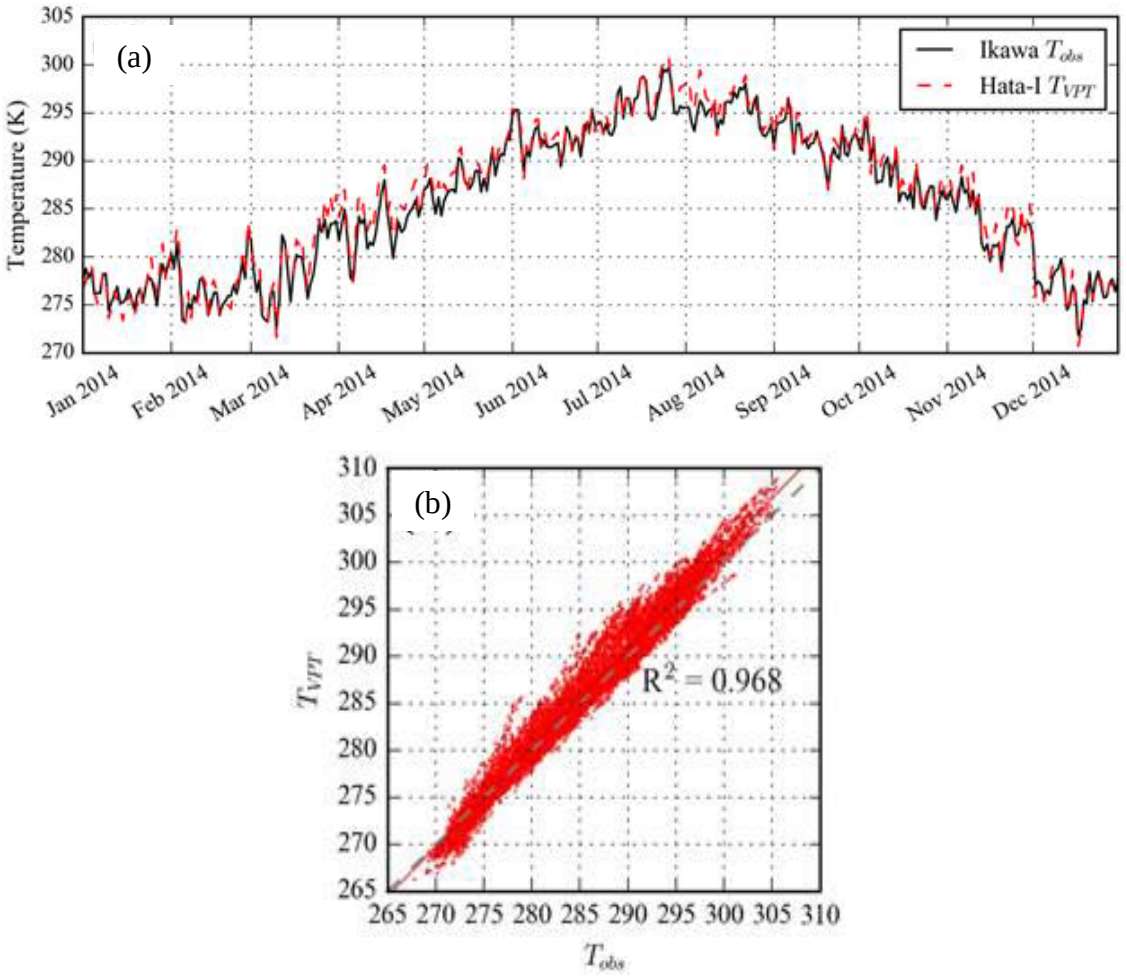

Figure 5.7. (a) Validation of VPT by observed temperature at Ikawa (T_{obs}) and temperature reproduced at Ikawa using VPT (T_{VPT}) for the and (b) Correlation between observed temperature (T_{obs}) and temperature reproduced from VPT (T_{VPT}) at Ikawa

5.6. Comparison of Lapse Rate with Other Studies

As discussed in the literature review, different approaches are in practice for the application of the temperature lapse rate for hydrological modeling and assessments. Most of research in the past has used constant fixed value, whereas, based on the data availability statistical analysis and interpolations are becoming more popular as they provide a wide range of the lapse rate. Despite of the variability the values adopted in

later approaches are not true representative of prevailing temperature profiling along the elevation. Based on the VPT, the variation of temperature lapse rate ranges from 0 °C to -9.8 °C, from the wet to dry adiabatic lapse rate, as shown in the comparison diagram (Figure 5.8).

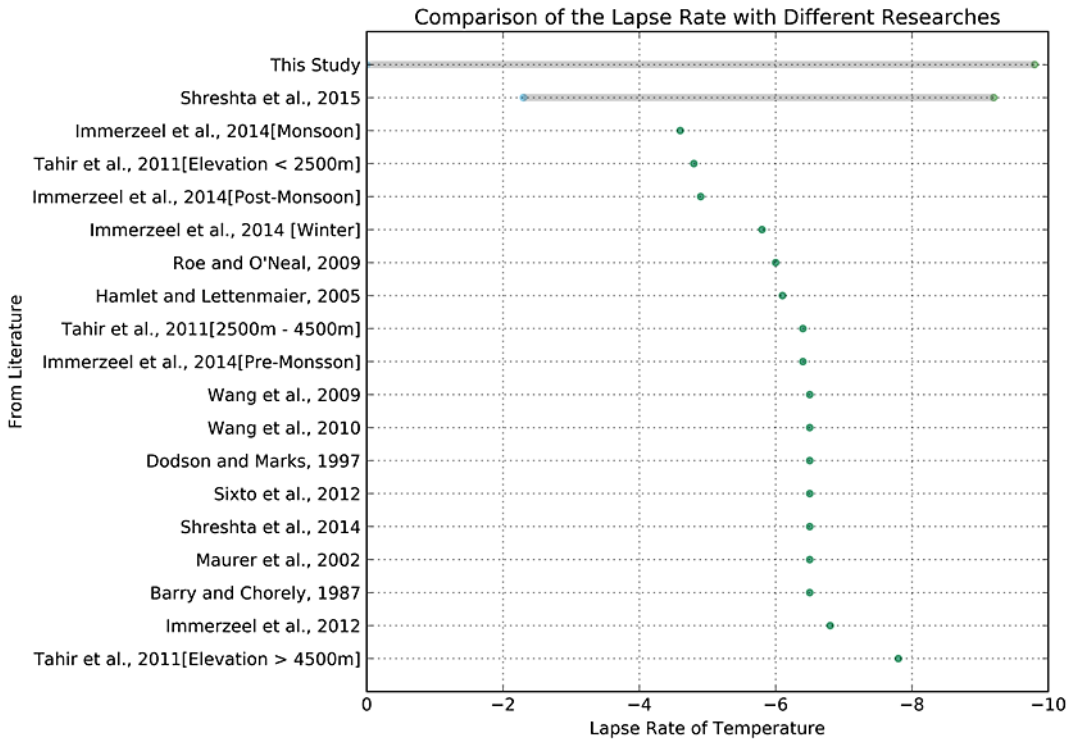

Figure 5.8. Comparison of Lapse Rate of Temperature from Vertical Profile of Temperature (VPT) with other studies

6. Application of integrated framework in Oi River Basin Japan

6.1. Introduction

This study integrates the merits of observational data with distributed atmospheric reanalysis and/or atmospheric model data for maximizing their utilization for establishing a simplified operational and integrated approach. The framework was applied to the Oi River Basin of Japan. There are series of dams constructed in the Oi River catchment, namely Nagashima Dam (downstream most), Ikawa Dam, Hatanagi-II Dam, Hatanagi-I Dam, Akaishi Dam, and Tashiro Dam (upstream most) as shown in Figure 6.1 below

The upper reach dams (Tashiro and Akaishi Dam) are smaller in size, functioning primarily as the sediment control and based on the run of the river mechanism with negligible or no storage facilities, whereas all other dams (Hatanagi-I, Hatanagi-II, Ikawa and Nagashima Dam) are mainly operated and managed from standpoint of power generation with storage capacity which is regulated and controlled by the relevant authorities. In winter the northern part of the Oi River Basin is completely covered with snow from mid-December to mid-March, which completely melts away during the spring season, and there is no snow in the summer season from mid-June to the end of September. Thus, the generation of hydropower plants from these dams is subject to seasonal snow cover. It is therefore critically important to develop and establish an integrated framework for simplified operation with reliability. This reliability can be addressed by data integration for reducing the uncertainties and providing a more realistic estimate of water especially in the melting period.

To illustrate the applicability of the framework the hydrological year October 2013 to September 2014 was selected and calibration was carried out for the hydrological years from October 2014 to September 2017.

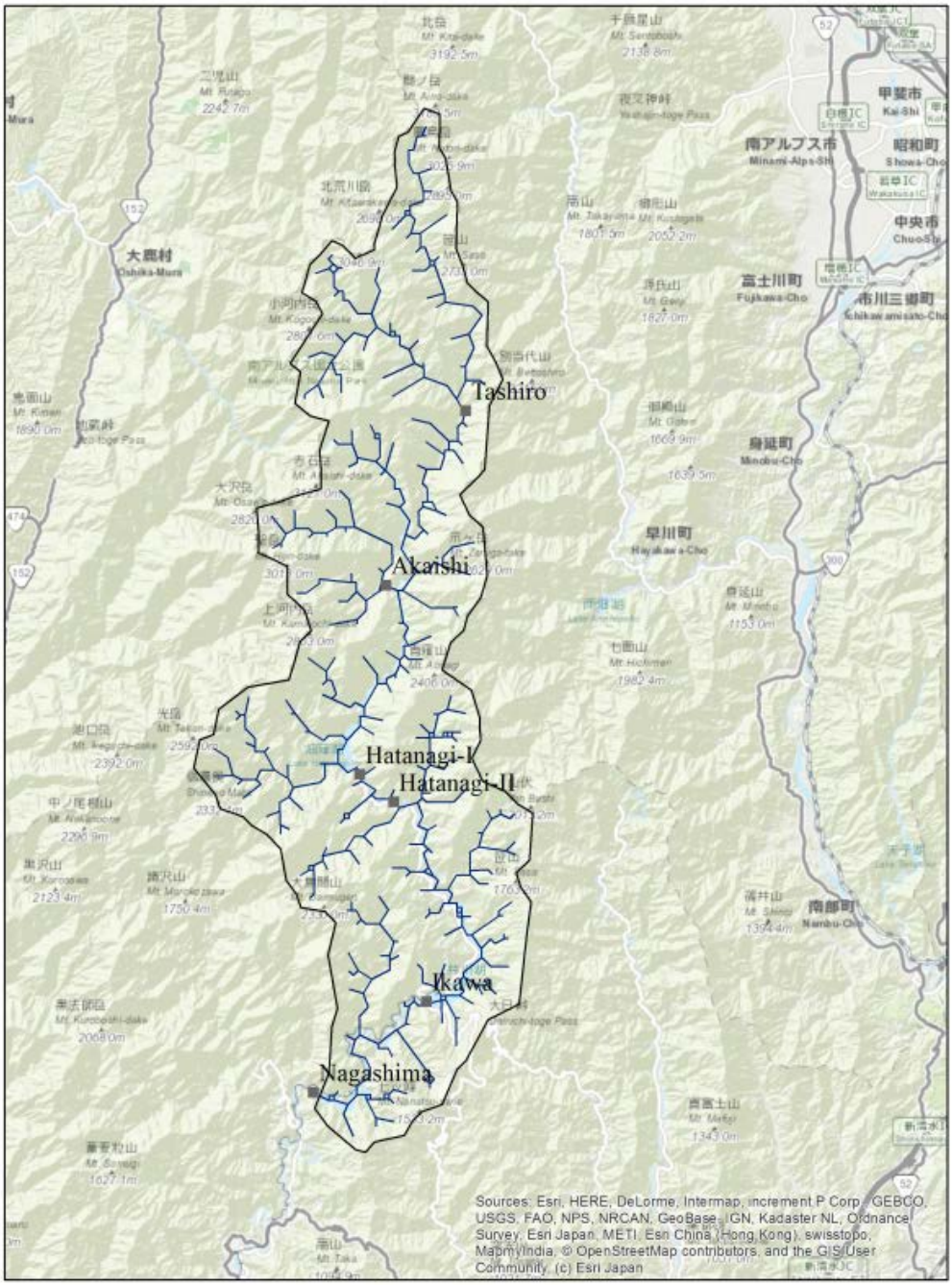

Figure 6.1. Hydropower Dams in Oi River Basin, Shizuoka Prefecture, Japan

It is also important to note that the study area selected as the mountainous basin for the implementation of the methodology proposed in framework is the northern part of the Nagashima Dam watershed outlet at the Hatanagi-I Dam (950 m) as described in Chapter 4 (Section 4.2).

6.1.1. Static inputs

Static inputs for the WEB-DHM-S include the preparation of the digital elevation model (DEM), soil map, and land-use map with various parameters. The DEM was obtained from the Advanced Space-borne Thermal Emission and Reflection Radiometer (ASTER) global digital elevation model (GDEM) version 002 developed through the cooperation of Japan's Ministry of Economy, Trade, and Industry (METI) and the United States National Aeronautics and Space Administration (NASA) with a 30 m resolution as shown in Figure 6.2a (https://asterweb.jpl.nasa.gov/gdem.asp).

The soil map was prepared using Food and Agriculture Organization (FAO) data with a relatively coarse resolution of 9 km (http://www.fao.org). The soil datasets include parameters such as saturated hydraulic conductivity for surface soil, hydraulic conductivity for root zone, hydraulic conductivity for groundwater zone, residual soil moisture content, saturated soil moisture content, and Van-Genutchen parameters like alpha and n. Only one type of soil (medium loam) was found due to coarse resolution of the FAO soil data and in this small watershed. The detailed description and values for different hydraulic and other soil parameters is given in Figure 6.2b. To include the morphological, optical, and physiological properties, the land use map was prepared from United States Geological Survey (USGS) global datasets with spatial resolution of 1 km. The vegetation types in land use datasets are reclassified as per SiB2 (Sellers et

al., 1996) as shown in Figure 6.2c (Appendix 1). All static datasets were resampled to model grid resolution of 250 m.

6.1.2. Dynamic Vegetation Forcing

Dynamic inputs such as Leaf Area Index (LAI) and Fraction of Photosynthetically Active Radiation (FPAR) data were from Moderate Resolution Imaging Spectroradiometer (MODIS) on-board Terra satellite. The product is known as MOD15A2 (Version 5), which is 8-day composite with a 1 km resolution. For the study area the single MODIS tile (h29v05) obtained from NASA Earth Observation Data and Information System (http://reverb.echo.nasa.gov) covers the whole watershed. As the standard MODIS products use Sinusoidal grid tiling system therefore it was projected to WGS 1984 UTM Zone 54N and then resampled to model the grid by the Modis Reprojection Tool (MRT, 2011).

6.1.1. Dynamic Meteorological Forcing (without precipitation and temperature)

The dynamic meteorological forcing required for the model includes the datasets for precipitation, air temperature, air pressure, relative humidity, wind speed and downward shortwave and longwave radiation with hourly temporal resolution. Stemming from multiple JRA-55 products, the two dimensional average diagnostic fields (fcst_phy2m) were used to obtain datasets for downward longwave and shortwave radiation flux at surface (W/m^2) and surface pressure (Pa). The specific humidity (kg/kg) at 2 m, the surface zonal and meridional wind speed (m/s) at 10 m above ground, and the total cloud cover (%) were obtained from surface analysis fields (anl_surf). These products are available with temporal resolution of three-hour (3 h) and relatively coarse spatial resolution of 0.5625 °, as demonstrated in the Figure 6.3 given below (http://search.diasjp.net/en/dataset/JRA-55).

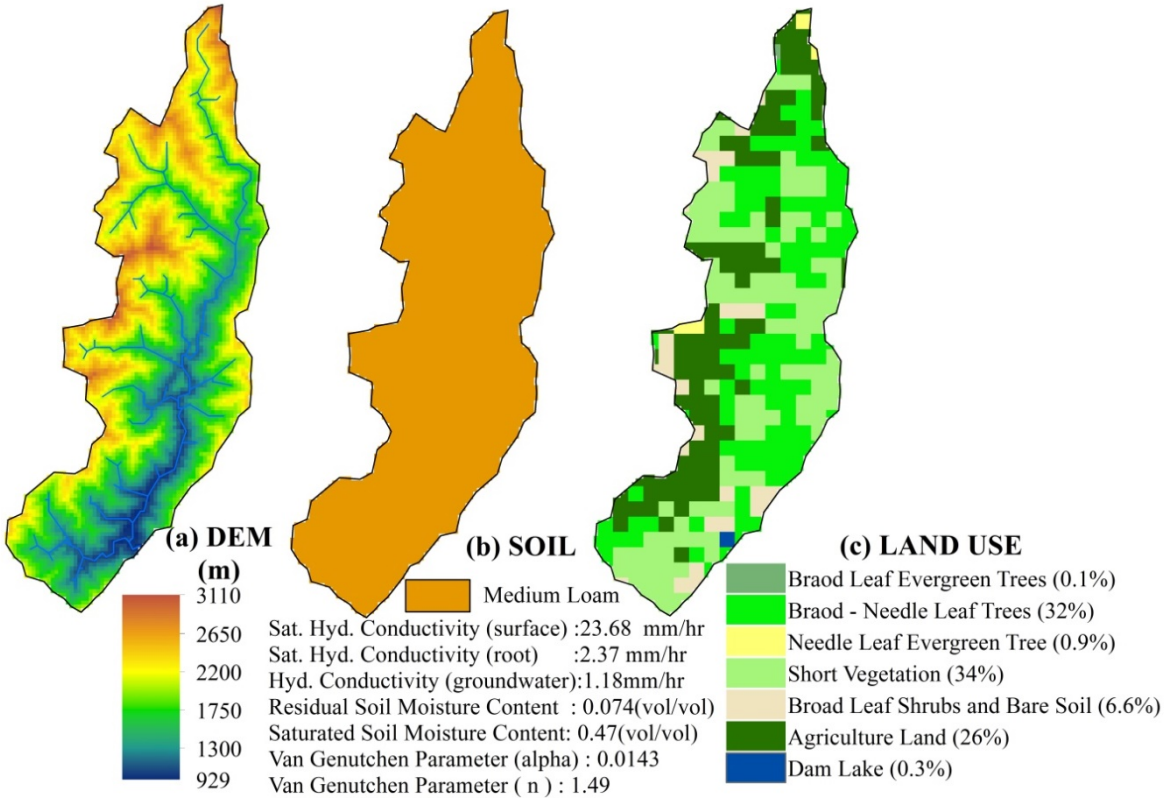

Figure 6.2. Static Dataset for input (a) Digital Elevation Map for Hatanagi Dam-I Basin with Oi River from ASTER-GDEM (b) Soil and parameters from FAO global datasets and (c) Land use types with respect to USGS global datasets and distribution in watershed

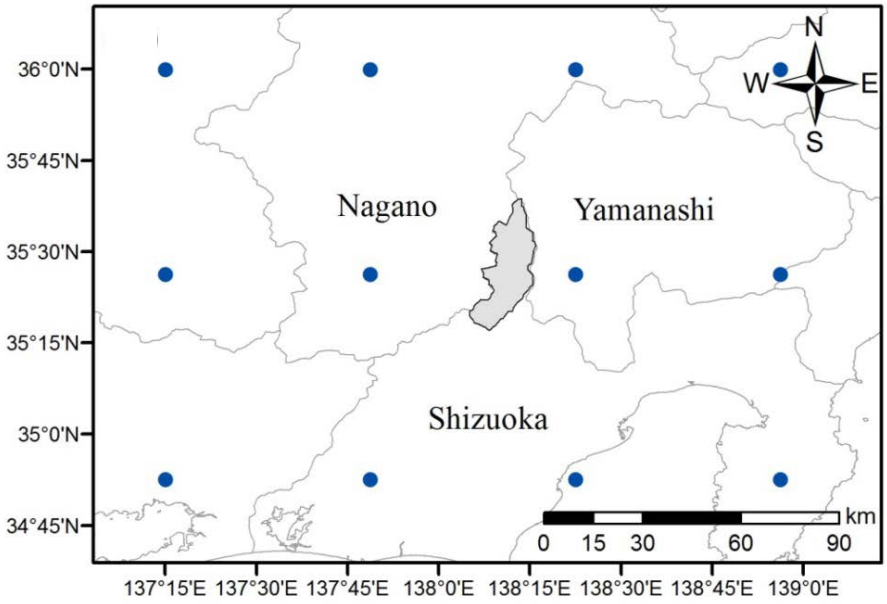

Figure 6.3. Location of study area within JRA-55 (0.5625°) grids for meteorological data for i) Downward Longwave & Shortwave radiation flux at surface (W/m2) and surface pressure (Pa) from two dimensional average diagnostic fields (fcst_phy2m) , ii) Specific humidity (kg/kg) at 2m, surface zonal and meridional wind speed (m/s) at 10m above ground and total cloud cover percentage by surface analysis fields (anl_surf)

6.2. Integrated Data for Precipitation and Temperature

6.2.1. 2-D spatial distribution of precipitation

There are four rain gauges inside the basin, as shown in Figure 6.4a with precipitation records from 2010 to 2017 and with 10-min temporal resolution. The rain gauges are considered as ground truth especially for rainfall but existing rain gauges are located predominantly at the valleys, therefore, unable to reflect the topographical complexity and realistic spatial variability of precipitation. The correct estimation of precipitation is subjected to the spatial distribution of precipitation events however, irregular network of rain gauges is too coarse to grasp the such spatial variability (Berne, Delrieu, Creutin, & Obled, 2004) but in principle the radar are capable of

collecting the spatial information correctly (Hazenberg, Yu, Boudevillain, Delrieu, & Uijlenhoet, 2011).

The Meteorological Service Support Center Japan under the supervision of Japan Meteorological Agency (JMA) is archiving composite radar product at Research Institute for Sustainable Humanosphere (RISH) established at Kyoto University. This composite radar product is known as “JMA all Japan Composite Rainfall GPV Data”. It covers the whole Japan with temporal resolution of 10-min over 1km grid resolution (Figure 3c) and is released through the (http://database.rish.kyoto-u.ac.jp).

Table 6.1. Characteristics of Meteorological Stations

Station	Elevation (m)	Latitude (d-m-s)	Longitude (d-m-s)	Variables
Hatanagi Dam – I	950	138°11’00”	35°29’56”	P, T
Akaishi	1,140	138°11’55”	35°26’44”	P, T
Tokusa	1,210	138°13’00”	35°24’43”	P
Nikengoya	1,450	138°14’40”	35°19’17”	P

There are over 1300 meteorological stations using automatic observation equipment collectively known as the Automated Meteorological Data Acquisition System (AMeDAS) in Japan. Furthermore, 26 radar instruments operated by the Ministry of Land and Infrastructure Management (MLIT) are also in operation. This composite data include 20 JMA & 26 MLIT C-Band weather radars data, calibrated by AMeDAS, MLIT, and available local government rain gauges. For reducing the effects of ground clutters and topographical features, JMA is selecting an optimal elevation angles for making a Constant Altitude Plan Position Indicator known as CAPPI (JMA, 2018). The CAPPI height for JMA radars is located near 2,000 m altitude in each place by using several Plan Position Indicators (PPIs) at low elevation angles. The dataset was

subset and resampled to 1hour temporal resolution and downscaled to the model grid resolution.

First, the preparation of the spatial distribution of precipitation from the rain gauges is discussed. The point data was converted to gridded data by the Angular Distance Weight (ADW) method (New, Hulme, & Jones, 2000) as per equation (6.1). The employed method for interpolation includes the weighting function to consider the distances of any number of available stations in such a way that grids nearest to the station have greater weights. This method also deals with the angular displacement to account for directional isolation of the irregular network of meteorological sites (Hofstra & New, 2009), as shown in equation (6.2).

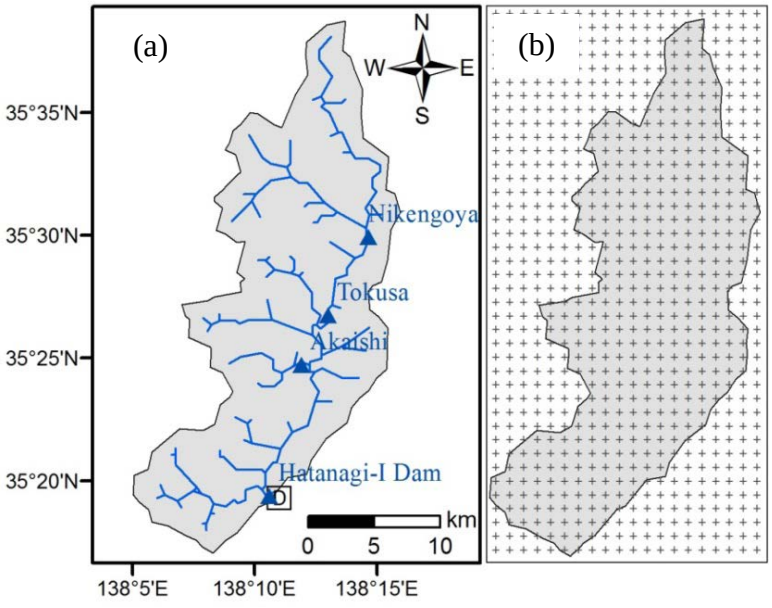

Figure 6.4. (a) Location of rain gauges station inside the study area (b) Japan Meteorological Agency (JMA) C – Band Radar grid (1 km) over the basin

$$P_g = \frac{1}{\sum_{i=1}^{ng} W_i}\left[\sum_{i=0}^{n} P_{gauge} W_i\right] \tag{6.1}$$

$$W_i = w_i\left\{1 + \frac{\sum_k w_k\left[1+\cos(\theta_k - \theta_i)\right]}{\sum_k w_k}\right\}, i \neq k \tag{6.2}$$

Here, P_g is the precipitation in model grid, P_{gauge} is the precipitation from rain gauges and W_i is the weighting factor for i^{th} gauge out of *ng* which denotes the total number of contributing rain gauge stations with w_i and w_k as weighting functions for distance and angular displacement. In mountainous regions, the correct measurement of the spatial variability of precipitation is recognized as major constraint in hydrologic modeling especially in snow fed region, therefore, correct spatial distribution of precipitation is principally crucial for reproducing the accurate hydrological response.

Table 6.2. Characteristics of JMA All Japan Composite Rainfall GPV Data

Product Name	20 JMA & 26 MLIT C-Band weather radars	Source: Quantitative forecast technique material, Improvement of Rainfall analysis, short-range rainfall forecast, rainfall nowcast, 2012, JMA (JMA, 2018)
Spatial Resolution	1 km	
Temporal Resolution	10 min	
Calibration Sources	AMeDAS, MLIT & Local Government gauges	
Distinction	At least calibrated by AMeDAS with for rainfall 1h interval and 1 km mesh	
CAPPI	2 km above ground	

The rain gauges are considered as ground truth especially for rainfall but existing rain gauges are located predominantly at the valleys, therefore, unable to reflect the

topographical complexity and realistic spatial variability of precipitation. To check the spatial distribution from both precipitation sources to select the precipitation to be used as input to the model, the spatial coverage obtained through the radar and interpolated gauge data were compared for arbitrary rainfall events. Interestingly, the northern part receives smaller amounts of rainfall, despite of multiple high mountain peaks as shown in Figure 6.5.

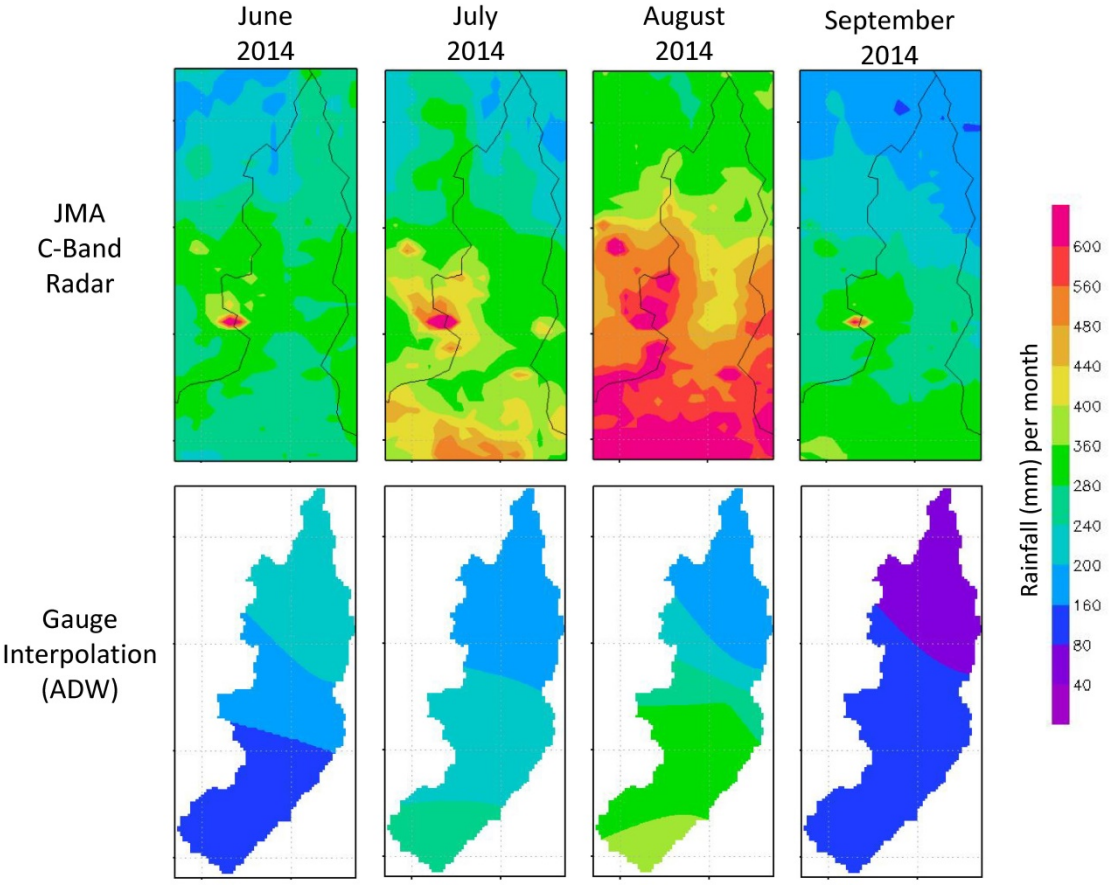

Figure 6.5. Comparison of Monthly Rainfall Spatial Distribution obtained through Gauge ADW Interpolated method and from C-Band Radar from JMA all Japan Composite Rainfall GPV Data, illustrating the difference in the spatial distribution (June–September, 2014)

6.2.2. 3-D spatial distribution of temperature

As described earlier, despite of the highest level of confidence in meteorological records from the representative stations, they largely contain sparse data, limited in number and unable to generate realistic 3-D distribution/profiles of meteorological parameters. 3-D distribution/profiles obtained from reanalysis products or atmospheric models can be regenerated more realistically by adjoining the in-situ data. The development of 3-D datasets for the temperature has been described in detail as Chapter 5. The daily maximum, minimum, and mean temperatures are available at two stations: Hatanagi Dam-I (950 m) and Akaishi (1,140m). On the other hand, out of 37 vertical levels from JRA-55 (anl_p125), the temperature and geopotential height data corresponding isobaric fields from 925 hPa to 675 hPa was downloaded from year 2013 to 2017. By considering the Hatanagi Dam-I temperature as the reference station temperature the vertical profile was constructed from JRA-55 geopotential heights and temperature, the profile was reconstructed, and this 3-D spatiotemporal temperature distribution was used as the temperature (Temp) input for WEB-DHM-S.

6.3. Seasonal Classification

Precipitation being the generic term that describes the form of moisture falling from air to ground surface or over the mountain, is broadly categorized as rainfall (liquid) and snowfall (solid) based on the prevailing temperature. The temperature that defines the partitioning of the precipitation phase (liquid or solid) is termed critical or threshold temperature (T_{thrs}), above which precipitation is primarily rainfall and below which is primarily snowfall (Jennings, Winchell, Livneh, & Molotch, 2018). In order to deal with the rainfall and snowfall separately, seasonal classification is important based on

temperature anomalies along elevation for which threshold temperature (T_{thrs}) is the most useful metric. Initially, a threshold temperature (T_{thrs}) was introduced as 0 °C (273.15 K) for the classification of summer and winter season as explained through equation (6.3). Temperature and geopotential heights values for various vertical surfaces corresponding to isobaric fields, from 925 hPa to 700 hPa, were obtained at six-hour temporal resolution, later resampled to 1 h, for the model input for period 2013 to 2015.

$$P_g = \begin{cases} Rain, \rightarrow T_g(z_g) > T_{thrs} \\ Snow, \rightarrow T_g(z_g) \leq T_{thrs} \end{cases} \tag{6.3}$$

P_g, T_g, and z_g stand for the precipitation, temperature and elevation at a particular model grid and T_{thrs} is the threshold temperature. The vertical temperature profile was used to produce the temperature throughout the basin elevation from available temperature data (2013-2017).

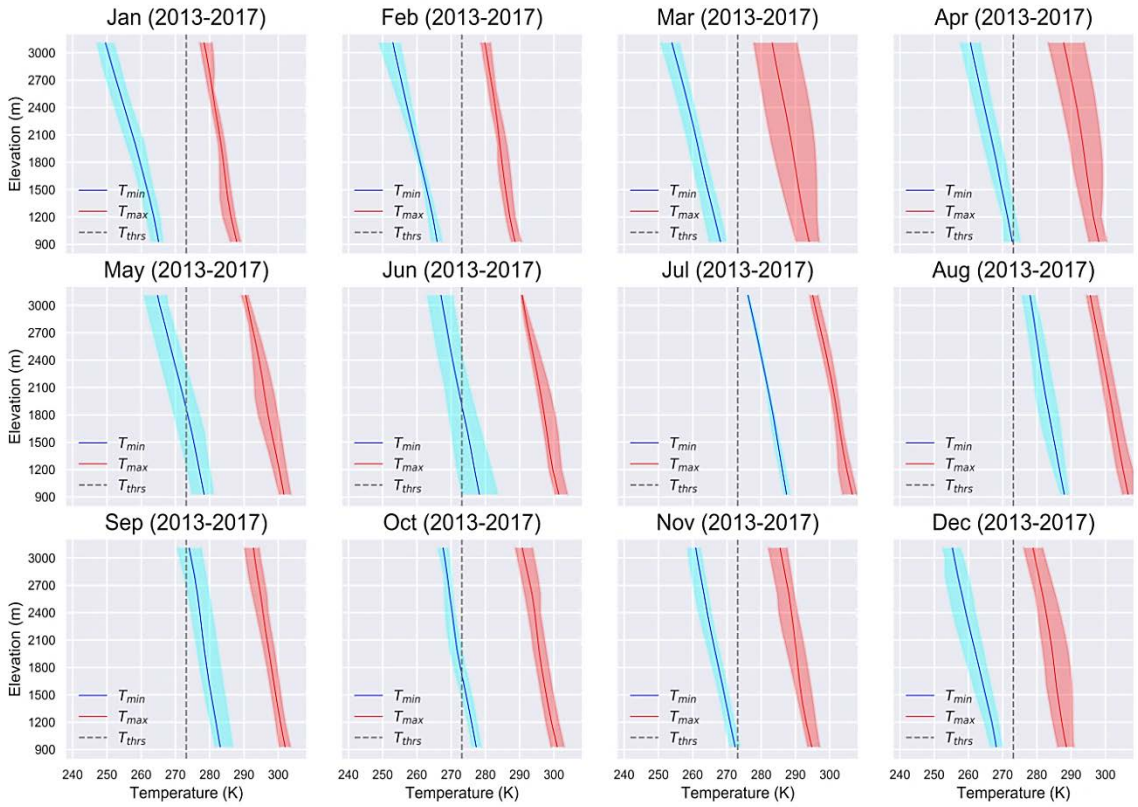

Figure 6.6. The anomalies of maximum and minimum mean monthly temperature and variations at different elevations basin ranging from 929m to 3110m obtained through Vertical Profile of Temperature (VPT) for 05-year period (2013 to 2017)

6.4. Evaluation Criteria

6.4.1. Evaluation Datasets

Inflows to Hatanagi-I Dam was provided by the *Chubu Electric Co. Japan* in collaboration with the Data Integration Analysis System (DIAS) forum (http://mizu.diasjp.net) for a period from 2011 to 2017. The dam inflow information was used as the observed discharge to compare with the simulated model discharge output.

Another dataset used for the evaluation in this study obtained was from MODIS aboard Terra (EOS-AM-1) product called the MODIS/Terra Snow Cover 8-Day L3 Global 500 m Grid Version-6 (MOD10A2). The maximum snow cover extent during an 8-day period is generated by compositing 500 m observations from MODIS/Terra Snow Cover Daily L3 Global 500m Grid (MOD10A1) by reducing the cloud effect. If snow is observed in a cell on any day during 8-Day period, the cell is mapped as snow (else no snow) and the cell is filled with the clear-view observation that occurred most often as land, lake etc. The cell is reported as cloud cover if it was cloud-obscured by clouds for all 8-days in the period. The tile (h29v05) covering the whole study area was downloaded from the National Aeronautics and Space Administration (NASA) Earth Observing System Data and Information System (EOSDIS) website (https://search.earthdata.nasa.gov). As all MODIS datasets are georeferenced to an equal-area sinusoidal projection therefore, the downloaded dataset was re-projected to the WGS 1984 UTM Zone 54N and then resampled to model grid resolution for snow cover analysis.

6.4.2. Discharge evaluation

For evaluation of simulated discharge against observed discharge the Nash Sutcliffe Efficiency (NSE) (Nash & Sutcliffe, 1970) and for volume the Percent Bias PBIAS (%) (Moriasi et al., 2007) are used in this study. By addressing the key parameters the simulated discharge is optimized by minimizing the errors through use of NSE and PBIAS (%), as expressed in equations (6.4-6.5) given below.

$$NSE = 1 - \frac{\sum_{i=1}^{N}\left(Q_{oi} - Q_{si}\right)^2}{\sum_{i=1}^{N}\left(Q_{oi} - \overline{Q}_o\right)^2} \tag{6.4}$$

$$\text{PBIAS}(\%) = \left(\frac{\sum_{i=1}^{N}\left(Q_{oi} - Q_{si}\right)^2}{\sum_{i=1}^{N} Q_{oi}} \right) \times 100 \tag{6.5}$$

Where, Q_{oi} and Q_{si} are the observed and simulated discharges at i^{th} time interval and $\overline{Q}_o$ is averaged observe discharge.

6.4.3. Snow Cover Evaluation

The simulated snow cover area (SCA) is compared to the MODIS-derived SCA by performing a pixel-by-pixel analysis for evaluation. As described in Chapter 4 (Section 4.1), the model (WEB-DHM-S) is capable of providing gridded information for simulated snow, and the model demonstrating the threshold for snow depth is set to be 4 cm (Carturan, Fontana, & Borga, 2012). On the other hand, the MODIS dataset provides information of existence and absence of snow in particular cells. Based on pixel-by-pixel analysis and the under- and overestimation of snow, three types of indices are calculated (Table 6.3) and errors are examined for simulated SCA with MODIS-derived SCA for defined threshold snow depth amount in each cell. In the case when the model and MODIS are both reporting snow in respective cells, it is considered as “A”. Similarly, if there is snow in model cell but no snow in MODIS cell, then this overestimation is considered to be “B”, and vice versa is “C”. Finally, when there is no snow in either model or the MODIS grid, it is denoted by “D”. The model accuracy, model overestimation, and model underestimation are calculated to quantify the

accuracy and bias of the model output. The average absolute bias ($|M|_{BIAS(avg)}$), average model accuracy ($M_{ACC(avg)}$), average overestimation ($M_{OE(avg)}$), and average underestimation ($M_{UE(avg)}$) over the comparison period (N) expressed in percentage (%) are calculated from equations (6.6-6.10) given below.

Table 6.3. Indices for Pixel-by-Pixel Evaluation of spatial distribution of snow

Description	MODIS : Snow	MODIS : No Snow
Model : Snow	A	B
Model : No Snow	C	D
Overestimation (M_{OE})	B/(A+B+C+D)	
Underestimation(M_{UE})	C/(A+B+C+D)	
Accuracy (M_{ACC})	(A+D)/(A+B+C+D)	

$$|M|_{BIAS(avg)}(\%) = \left(\frac{\sum_{i=1}^{N} |Model_{SCA} - MODIS_{SCA}|}{N} \right) \times 100 \tag{6.6}$$

$$M_{ACC(avg)}(\%) = \left(\frac{\sum_{i=1}^{N} M_{ACC}}{N} \right) \times 100 \tag{6.7}$$

$$M_{OE(avg)}(\%) = \left(\frac{\sum_{i=1}^{N} M_{OE}}{N} \right) \times 100 \tag{6.8}$$

$$M_{UE(avg)}(\%) = \left(\frac{\sum_{i=1}^{N} M_{UE}}{N} \right) \times 100 \tag{6.9}$$

$$M_{ERR(avg)}(\%) = M_{ACC(avg)} - \left(M_{OE(avg)} + M_{UE(avg)} \right) \tag{6.10}$$

6.5. Results of Analysis

6.5.1. Summer season analysis

Out of the two available datasets for precipitation, the JMA C-Band radar product (All Japan Composite Rainfall GPV) is used as model input besides other dynamic forcing. In terms of spatial coverage and temporal consistency, the gridded datasets provide better information than interpolated point observation but with considerable potential for errors. The attenuation of radar signals due to wetting of radome by rainwater, Drop Size Distribution (DSD), beam blocking due to orography and distance from radar are the primary the sources of errors. Uncertainties exist despite of the fact that JMA-C band radar product is calibrated with a high density-gauge network from known as AMeDAS (Makahira, Uekiyo, Tabata, & Abe, 1996). During the summer season (July to September) the rainfall analysis was performed 03 years (2013-2015). Next, we plotted the monthly precipitation aggregates for each month of the summer season to check the collective response during the hot season. It was done by obtaining the radar rainfall estimate at the same location as that of existing meteorological stations.

To establish a correlation between the interpolated gauge and radar rainfall, the same pixel values were selected. The one-hour values were plotted for four stations: Hatanagi-I, Akaishi, Tokusa, and Nikengoya, represented by HAT, AKA, TOS, and NIK, respectively hereafter. A positive correlation was found for each month in summer, as shown in Figure 6.7a. Furthermore, the total monthly rainfall for these selected months was plotted to have a quantitative overview of both sources Figure 6.7b. For each station, pixel values were used to calculate the gauge-to-radar ratio

(G/R). From average G/R for all stations for each month, the BCF for rainfall $\boldsymbol{\alpha_R}$ was estimated for rain (Table 6.4).

Table 6.4. Estimation of bias correction factor for summer season for station's G/R

Year	Month	HAT (950m)	AKA (1140m)	TOS (1210m)	NIK (1450)	Monthly Average
2013	Jul	0.64	0.99	0.87	0.66	0.79
	Aug	0.67	0.79	0.84	0.75	0.76
	Sep	1.35	1.63	1.97	1.59	1.63
2014	Jul	0.72	0.69	0.76	0.70	0.72
	Aug	0.74	0.86	0.79	0.43	0.70
	Sep	0.64	0.65	0.60	0.28	0.54
2015	Jul	0.73	0.77	0.91	0.43	0.71
	Aug	0.81	0.69	0.69	0.89	0.77
	Sep	0.72	0.67	0.70	0.86	0.74
					Average	***0.82***

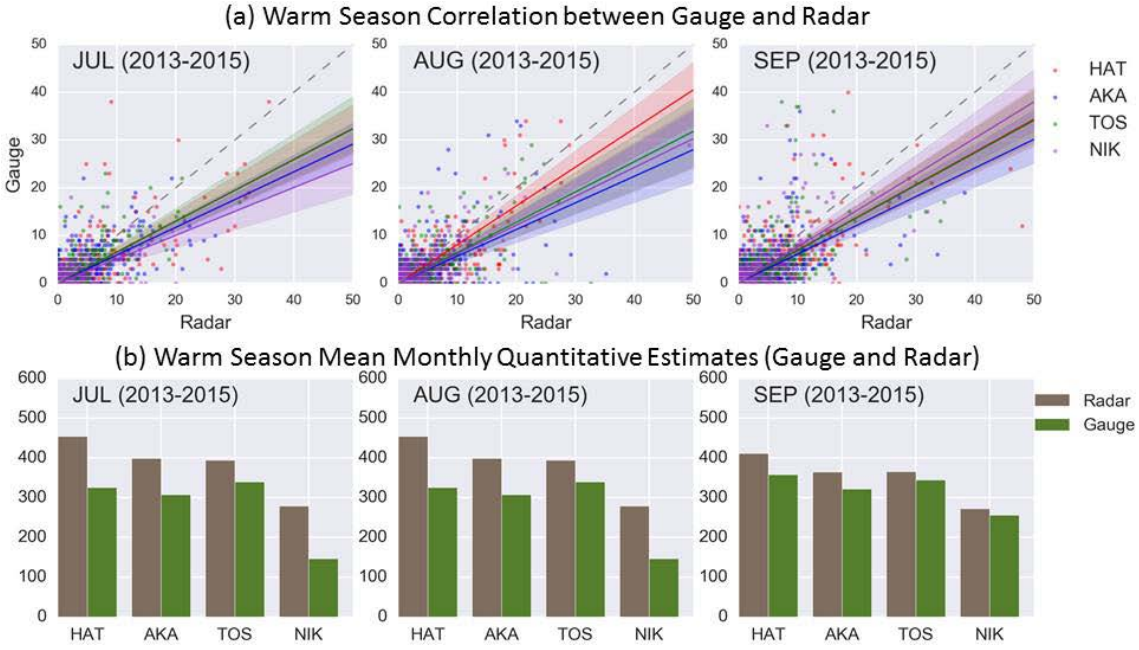

Figure 6.7. Warm season (a) correlation between observed hourly gauge rainfall at four stations and JMA C-Band radar rainfall estimate at same pixel location (b) comparison of mean monthly quantitative rainfall at four gauging stations rainfall records with JMA C-Band radar estimates from 2013 to 2015

As the radar rainfall furnished the actual spatial distribution of rainfall despite the overestimation in the summer season, the composite rainfall product by JMA was preferred for hydrological simulation. The calculated BCF for rainfall ($\boldsymbol{\alpha_R}$) based on the G/R ratio was then applied to the radar rainfall to reproduce the discharge as shown in equation (6.11).

$$P_{g_{corr}} = \alpha_R P_g \tag{6.11}$$

For any grid, $P_{g_{corr}}$ is the corrected precipitation (rainfall) and P_g stands for the selected radar product rainfall. Figure 6.8 shows the result for discharge simulation using original precipitation from radar and corrected precipitation as described above. The extreme overestimation of peak discharges significantly diminished with the application of BCF. The NSE improved from -1.56 to -0.15 abruptly and PBIAS shifted from 10.74% to -16.82%, with significant over and underestimation.

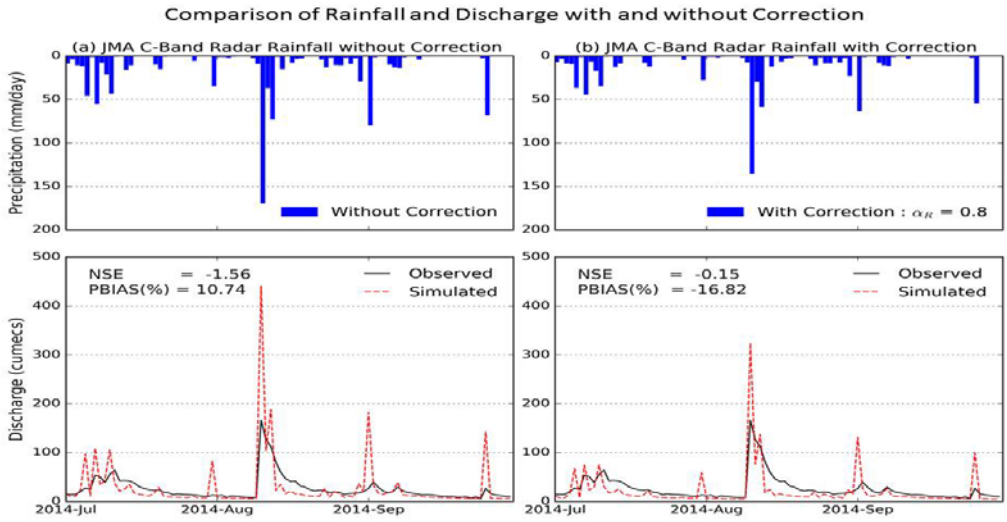

Figure 6.8. Rainfall and Discharge Comparison (a) without (b) with bias correction

6.5.2. Calibration in Summer Season

The considerable over and underestimation of simulated discharge, compared to observed discharge, needs to be addressed. As described in the methodology section, in sustaining the surface and subsurface flow in the aftermath of rainfall, the soil and land-use properties of the watershed have substantial significance. The uncertainties in global data can be addressed by soil–water interaction in the physically-based distributed hydrological modeling system by calibration loop C1. In this section, the role of most sensitive parameters is illustrated based on the statistical evaluation (NSE, PBIAS) of the model response.

The vertical movement water in soil is controlled by the intrinsic permeability, also known as the saturated surface hydraulic conductivity, which considers the water movement through saturated media. Figure 6.9a shows the model output for corrected rainfall with global data (Default) values. The overestimation of peak discharges is clearly visible, and the model efficiency for NSE is very low (-0.15) with PBIAS (-16.82%). The pronounced peaks represent limited or no water absorption in soil and water contribution toward the generation of surface runoff in general. The parameter for saturated surface hydraulic conductivity in this modeling system is denoted by ksat1. By increasing ksat1, more water is allowed to enter into the soil. The value is increased to a level where peak discharges are at least that of the observed discharge. The result is NSE = 0.69, and PBIAS also altered from -16.82% to -22.5%, as shown in Figure 6.9b and value is fixed for the next few levels. The differences in texture, structure, and porosity due to the layered structure of soil result in different horizontal and vertical permeability. These factors reflect the directional dependency of hydraulic

conductivities, causing soil to be anisotropic in nature. The anisotropic behavior of soil has a significant role in land drainage and subsurface lateral flow.

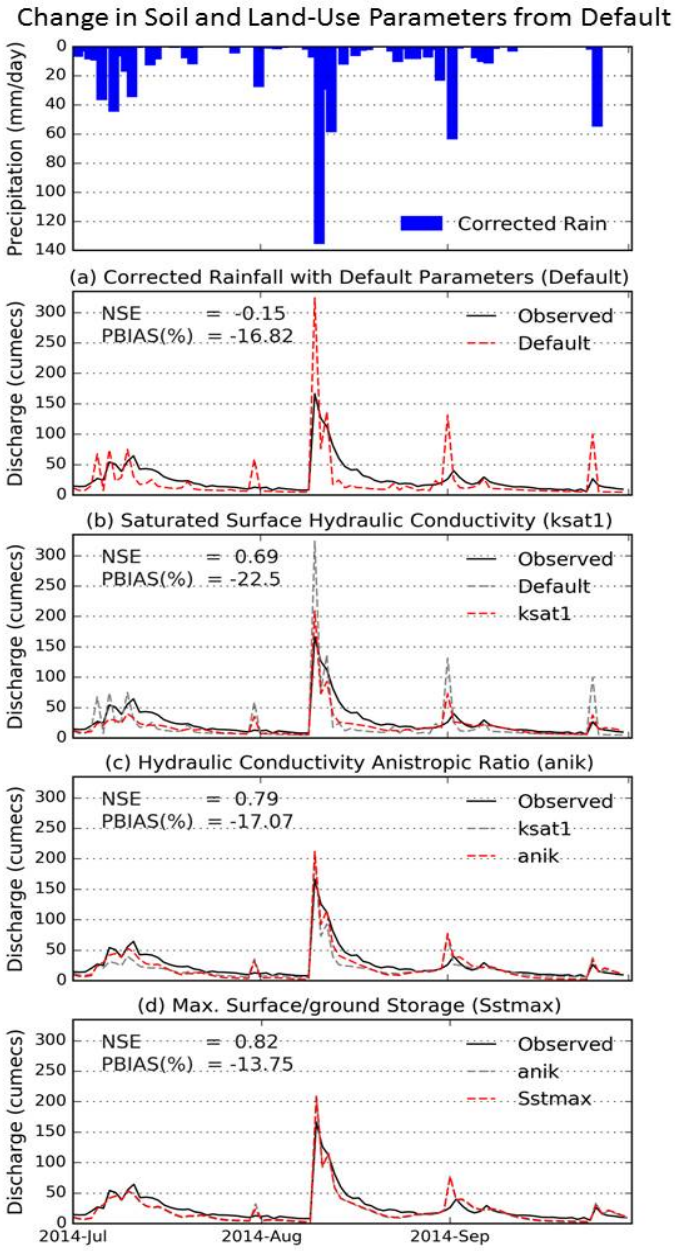

Figure 6.9. (a) With default values in soil and land-use datasets (b) lowering discharge peaks by increasing saturated surface hydraulic conductivity (c) improving subsoil interflow movement by altering hydraulic conductivity anisotropic ratio (d) in mountainous areas the ground/surface storage have very minor impact.

Therefore, with horizontal saturated hydraulic conductivity greater than vertical saturated hydraulic conductivity, there is an increased subsurface lateral flow. Despite improvements in the simulated discharge in Figure 6.9b**,** there are abrupt variations in peak discharge, and there is no or insufficient base flow. The base flow can be increased by altering the anisotropic ratio, which is denoted by anik in the current modeling system. To improve the lateral flow, anik needed to be increased to fill the gaps for base flow, as compared to the observed output. With this improvement, the NSE turned to 0.79 and the PBIAS changed to -17%, as shown in Figure6.9c.

Surface conditions are defined by the physiological properties of vegetation and ground cover. The hydrological response of two distinct land-use types, such as forests with dense vegetation, will offer more resistance to flow; meanwhile, urban areas with sparse vegetation will result in quick runoff or flooding. The surface storage/retention due to land-use types (defined in SiB2) is denoted as ground surface storage Sstmax in the model. As a mountainous area, the parameter has a negligible impact on the current basin. For this basin, the alteration of land-surface parameter resulted in NSE = 0.82 and PBIAS = -13.75%, as shown in Figure 6.9d. Hereafter, the calibrated values for the soil and land surface parameters are fixed to conduct hydrologic analysis in winter season.

6.5.3. Winter Season Analysis

Due to the inherent properties of the snow, obtaining accurate spatiotemporal distribution of snow in terms of accumulation and ablation for different land-use types under different climates (Shrestha et al., 2015) is a daunting challenge. As discussed earlier, observational sources such as rain gauges, weather radar, and satellite products are unable to present the actual amounts of snowfall. The role of temperature for determining the precipitation patterns and amount, by and large depends on the spatial

distribution of temperature. To cope with the temperature distribution, the VPT was developed and introduced based on the moisture conditions obtained from JRA-55 for a mountainous area. From available sources of precipitation datasets, we examined the correlation of meteorological station records and C-Band radar precipitation estimates, both in quantitative and spatial analysis, following a similar approach already adopted for rainfall in Section 5.1. For winter analysis, we have subdivided this season into further sub-seasons such as pre-winter (October–December), mid-winter (January–March), and post-winter (April–June) seasons. The correlation of precipitation from four meteorological stations' hourly records and corresponding estimates from radar (with the same pixel location as that of meteorological station) is plotted in Figure 6.10a. There is a positive correlation between station records and, particularly, for the mid-winter season. Meanwhile, the mean monthly total precipitation from 2013 to 2015 is shown quantitatively in Figure 6.10b.

As compared to the rainfall there is no well-defined and distinct pattern for the entire winter season for evaluating BCF for winter (α_S). From the quantitative analysis presented in Figure 6.10b for mid-winter, it is evident that both gauge and radar rainfall estimates are found to be almost identical at all the stations. Also in mid-winter season, the mean temperature is a below-freezing temperature for entire elevation therefore precipitation mainly occurs as snowfall. Whereas, in the pre & post winter seasons there is enormous discrepancy with different patterns especially at the commencement of spring (March) when temperatures are drastically increasing. Other than the mid-winter season, the radar precipitation is comparatively overestimated mainly due to rainfall in addition to snowfall as a result of a drastic variation in temperature along the altitudinal range. Stations with lower altitude showed overestimation of precipitation by radar

compared to gauge precipitation estimate as temperature are relatively higher at lower elevation and the resulting precipitation is dominantly rainfall. Conversely over the highest elevated station, where the air temperature is relatively lower, the differences between the gauge and radar are negligible.

Based on the mean monthly quantitative estimates for precipitation, the BCF for the winter (α_S) was calculated as 0.90 as shown in Table 6.5. In case the of radar precipitation appraisal, the distinction of precipitation phase (solid or liquid) is critically indispensable.

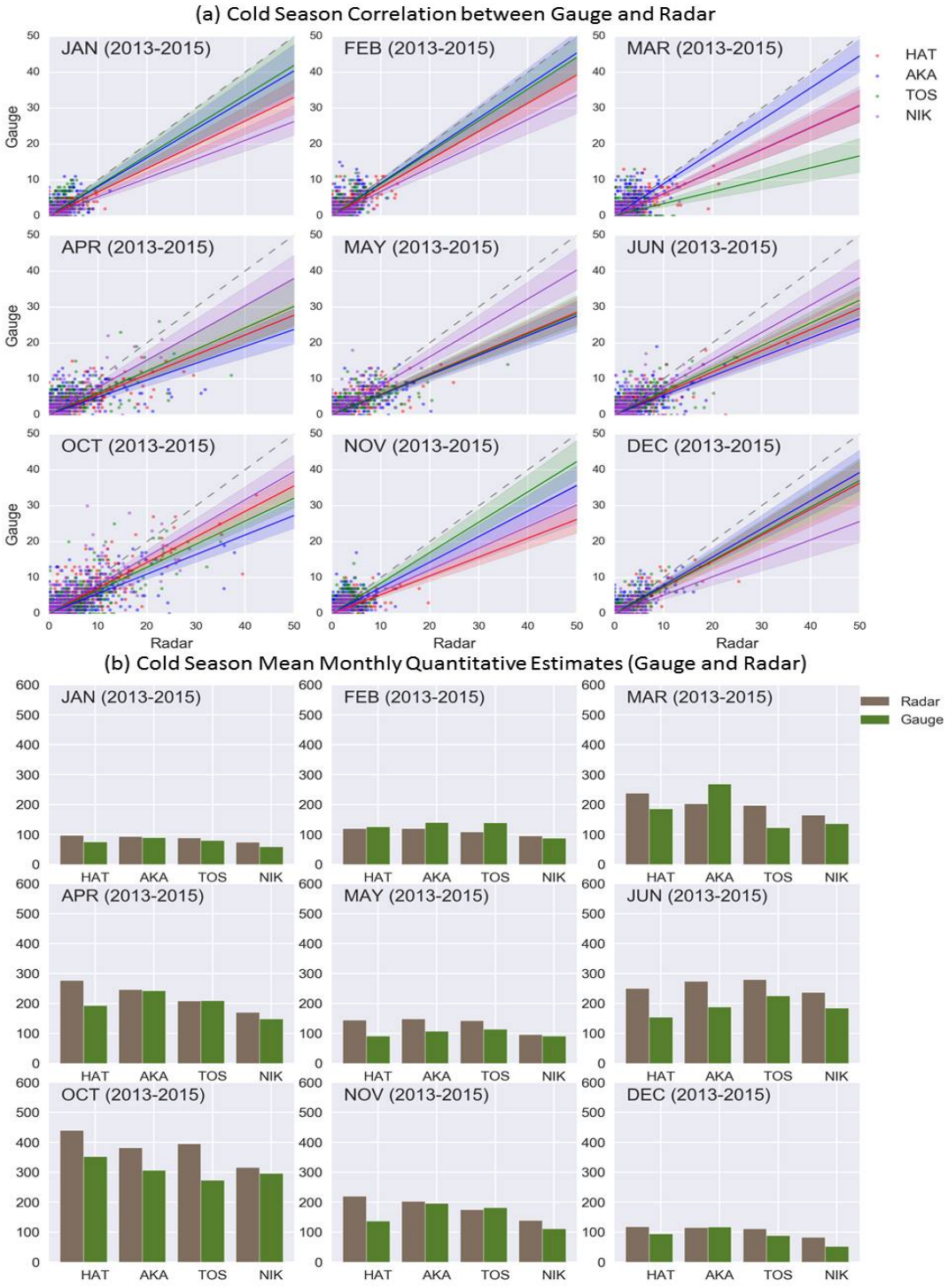

Figure 6.10. Cold season (a) correlation between observed hourly gauge rainfall at four stations and JMA C-Band radar rainfall estimate at same pixel location (b) comparison of mean monthly quantitative rainfall at four gauging stations rainfall records with JMA C-Band radar estimates from 2013 to 2015

Table 6.5. Estimation of Bias Correction factor for winter season (2013–2015)

Year	Month	Season	HAT (950m)	AKA (1140m)	TOS (1210m)	NIK (1450)	Monthly Average
2013	Dec	Mid Winter	0.90	0.77	0.94	0.40	0.75
	Jan		1.43	1.20	1.42	0.94	1.24
	Feb		1.17	1.53	1.48	0.68	1.21
	Mar	Post Winter	1.08	2.05	1.79	1.22	1.54
	Apr		0.94	1.52	1.45	1.25	1.29
	May		0.85	0.79	1.40	0.89	0.98
	Jun		0.64	0.76	0.80	0.44	0.66
	Oct	Pre Winter	1.03	1.00	0.72	1.16	0.98
	Nov		0.88	1.47	1.53	0.95	1.21
2014	Dec	Mid Winter	0.68	1.11	0.66	0.57	0.75
	Jan		0.81	0.98	1.06	0.61	0.86
	Feb		1.07	0.83	1.07	1.27	1.06
	Mar	Post Winter	0.72	1.01	0.64	0.67	0.76
	Apr		0.69	0.63	0.69	1.07	0.77
	May		0.58	0.63	0.87	1.08	0.79
	Jun		0.74	0.70	0.68	0.92	0.76
	Oct	Pre Winter	0.51	1.22	1.05	0.81	0.90
	Nov		0.68	1.11	0.66	0.57	0.75
2015	Dec	Mid Winter	0.87	1.04	0.92	0.85	0.92
	Jan		0.58	0.87	0.60	0.87	0.73
	Feb		0.60	0.92	1.19	0.60	0.83
	Mar	Post Winter	0.59	1.12	1.25	0.90	0.97
	Apr		0.57	0.82	0.92	0.78	0.77
	May		0.48	0.77	0.68	0.88	0.70
	Jun		0.62	0.66	0.77	0.85	0.72
	Oct	Pre Winter	0.53	0.69	0.66	0.49	0.59
	Nov		0.55	0.65	0.81	0.72	0.68
						α_S	***0.90***

It is also noticeable that the precipitation amount in the mid-winter season observed by both gauge and radar are relatively smaller but the snow cover extent data observed by the MODIS (MOD10A2) product revealed that over 90% of the basin area covered with snow in this period (Figure 6.11), possibly due to heavy snowfall mainly as precipitation.

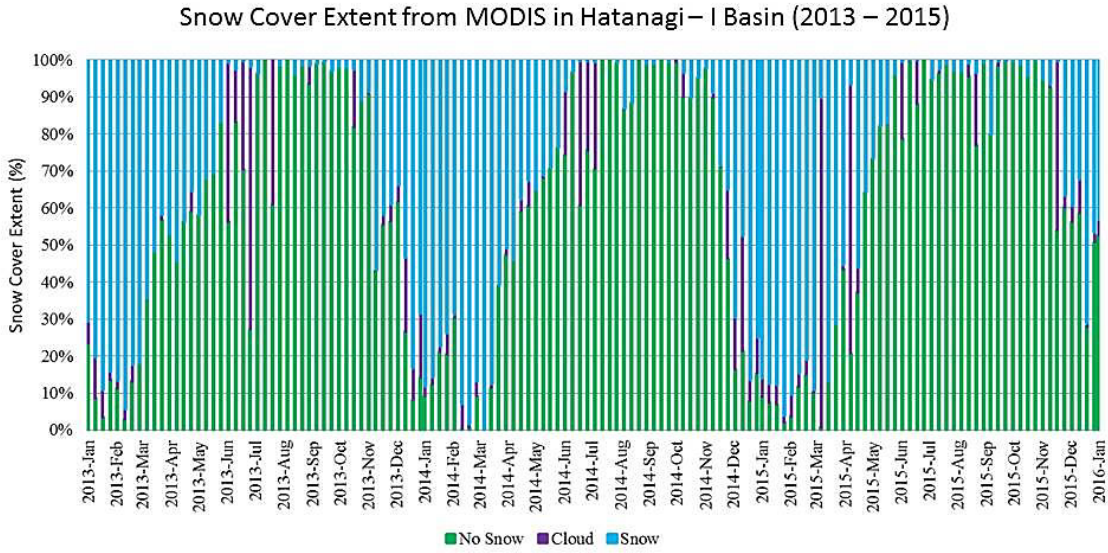

Figure 6.11. Segregation of observed snow extent compared to clouds and no-snow extent expressed as percentage (%) derived from MODIS (MOD10A2) product for 3 years (2013 – 2015)

The coexistence of snow and rain mainly depends on freezing temperatures and available moisture, and it is therefore impossible, in reality, to fix certain values for rainfall or snowfall due to which modeling such realistic phenomenon is challenging. The attenuation in radar reflectivity is highly anticipated due to the phase of the precipitation, either as rainfall or snowfall. The snowflakes that form in the upper atmosphere vary greatly in shape and size and typically much larger than the rain droplets. Moreover, ice does not reflect energy as effectively as water as both the liquid water and ice have different temperature and structure. Due to discrete microphysical properties and natural variability of ice particles physical characteristics, the accurate precipitation estimation of snowfall is highly indispensable. The water content of the snow also alters the radar reflectivity, more is the water content higher is the reflectivity difference as compared to rain droplet. The fall velocity, non-spherical shape, density

and particle size distribution of ice/snow particles significantly affect the scattering signature for radar.

To devise a simplified and operational solution and considering the above issues, the uncertainties regarding precipitation measurements and due to the coexistence of rain and snow for pre- and post-winter are critically essential to address. In order to proceed, first of all, the BCFs evaluated from the mean monthly quantitative analysis based on the gauge-to-radar ratio (G/R), rainfall (α_R= 0.80), and winter (α_S= 0.90) were introduced to address the precipitation for one complete hydrological year (October 2013 – September 2014). The output was examined not only in terms of discharge (quantitatively) but also considering the snow extent (spatially) simultaneously, as described in Chapter 3. It was considered to be Case 1, and based on the evaluation parameters, underestimation of discharge (NSE = 0.66, PBIAS = -25.16%) was the result, as shown in Figure 6.14a (Case 1). The inter-comparison of simulated snow cover area (SCA) shows a huge underestimation of snow compared to the MODIS-derived snow extent (MOD10A2) on both pre- and post-winter seasons. The underestimation of discharge was mainly due to the insufficient amount of snowfall with a higher average absolute bias ($\left|M\right|_{BIAS(avg)}$ = 13.07%) and large average underestimation (M_{UE_AVG} = 14.69%), as shown in Case 1 of Figure 6.14b. To overcome this underestimation of snowfall the value for BCF for the winter was increased to relatively higher number (α_S= 2.0) in Case 2. In this case, it was observed that the precipitation in the winter season increased significantly, resulting in overestimation of discharge in the middle of post-winter season (April) with simultaneous underestimation in end of the post winter season (May). Yet the output for

the model snow cover in comparison with MODIS snow cover extent revealed that in pre and mid-winter season, significantly large amount of snow accumulated throughout the basin even at lower elevations where the air temperature is higher. This high temperature at lower elevations swiftly melted the snow which resulted in overestimation in April but an underestimation in May, from which it can be concluded that spatial distribution of snowfall is non-uniform and nonlinear with elevation. It is understandable that lower temperatures over high altitudes are likely to collect more precipitation as snowfall in the winter season compared to low-lying area, these areas with relatively higher temperatures are likely to receive liquid precipitation. It led to a hypothesis of dividing the basin into different altitudinal bands and using different BCFs to address the spatial distribution of snowfall correctly. For reducing the effects of ground clutters and topographical features, JMA is selects an optimal elevation angles for making a constant altitude plan position indicator known as CAPPI (JMA, 2018). The CAPPI height for JMA radars is located near 2,000 m altitude in each place by using several plan position indicators (PPIs) at low elevation angles.

Because of this reason incomplete or partial beam resulted in For “Case 3” we consider the CAPPI to be the boundary and divide the basin in two elevational bands (Figure 6.13), the lower elevational band is B_1 (929 m - CAPPI) and the higher elevational band is B_2 (CAPPI - 3,110 m). The BCFs for these two bands are represented by α_{SB1} and α_{SB2} respectively, hereafter.

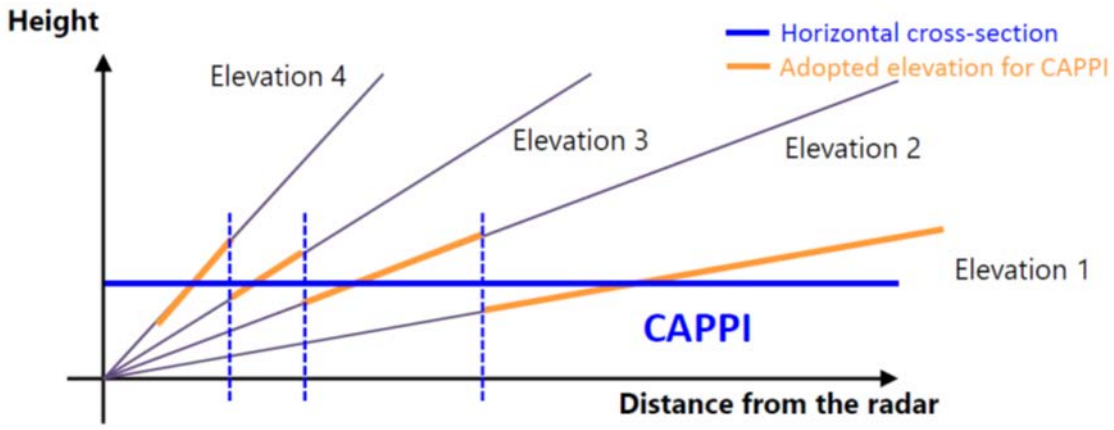

Figure 6.12. Schematic Diagram for Constant Altitude Plan Position Indicator (CAPPI) (JMA, 2018)

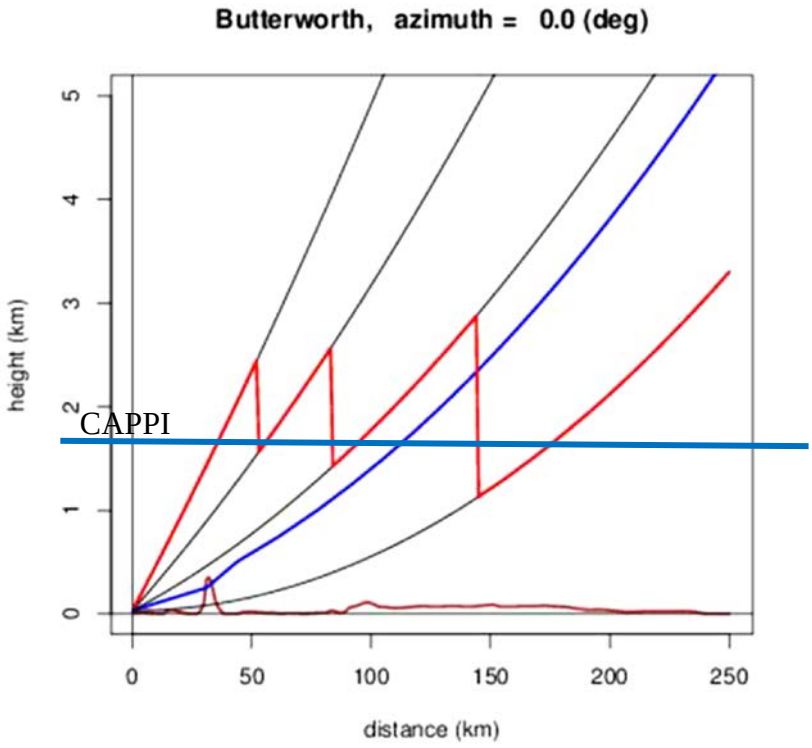

Figure 6.13. CAPPI Height of 2 km Adopted by JMA for the composite product (JMA, 2018)

$$P_{g\_corr} = \begin{vmatrix} \alpha_R P_g & (T_g > T_{thrs}) & 929m < z_g < 3110m \\ \alpha_{SB1} P_g & (T_g \le T_{thrs}) & 929m < z_g < CAPPI \\ \alpha_{SB2} P_g & (T_g \le T_{thrs}) & CAPPI < z_g < 3110m \end{vmatrix} \quad (6.12)$$

Where, P_{g_corr} is corrected precipitation, α_R is BCF of rainfall, and α_{SB1} and α_{SB2} are BCFs for snowfall for bands B1 and B2 respectively. The T_{thrs} denotes threshold temperature for rain/snow whereas, P_g, T_g, and z_g are the precipitation, temperature and elevation of grid respectively. Based on criteria defined in equation 6.11, the BCF for rainfall was kept as before ($\alpha_R = 0.80$) and for winter the BCF for lower band B1 was kept as calculated ($\alpha_{SB1} = 0.90$) However, winter BCF for band B2 was increased to much larger value ($\alpha_{SB2} = 2.40$) as the higher elevation air temperature is much lower. With such an application for the BCFs for rainfall and snowfall the not only the discharge but also the spatial distribution of snow cover improved as higher elevation received more snow owing to the low temperature and larger BCF for snow. The under- and overestimation of discharge was addressed and the SCA in the post-winter season was also significantly enhanced. The graphics for Case 3 in Figure 6.14a show improvement of discharge with NSE = 0.74 and PBIAS = -12.23%, whereas Figure 6.14b **(**Case 3**)** designated for the spatial distribution of snow with increased average model accuracy ($M_{ACC(avg)}$) from 83.5% to 87.13% and decreased average absolute bias ($|M|_{BIAS(avg)}$) from 13.07% to 8.22% based on pixel-by-pixel analysis.

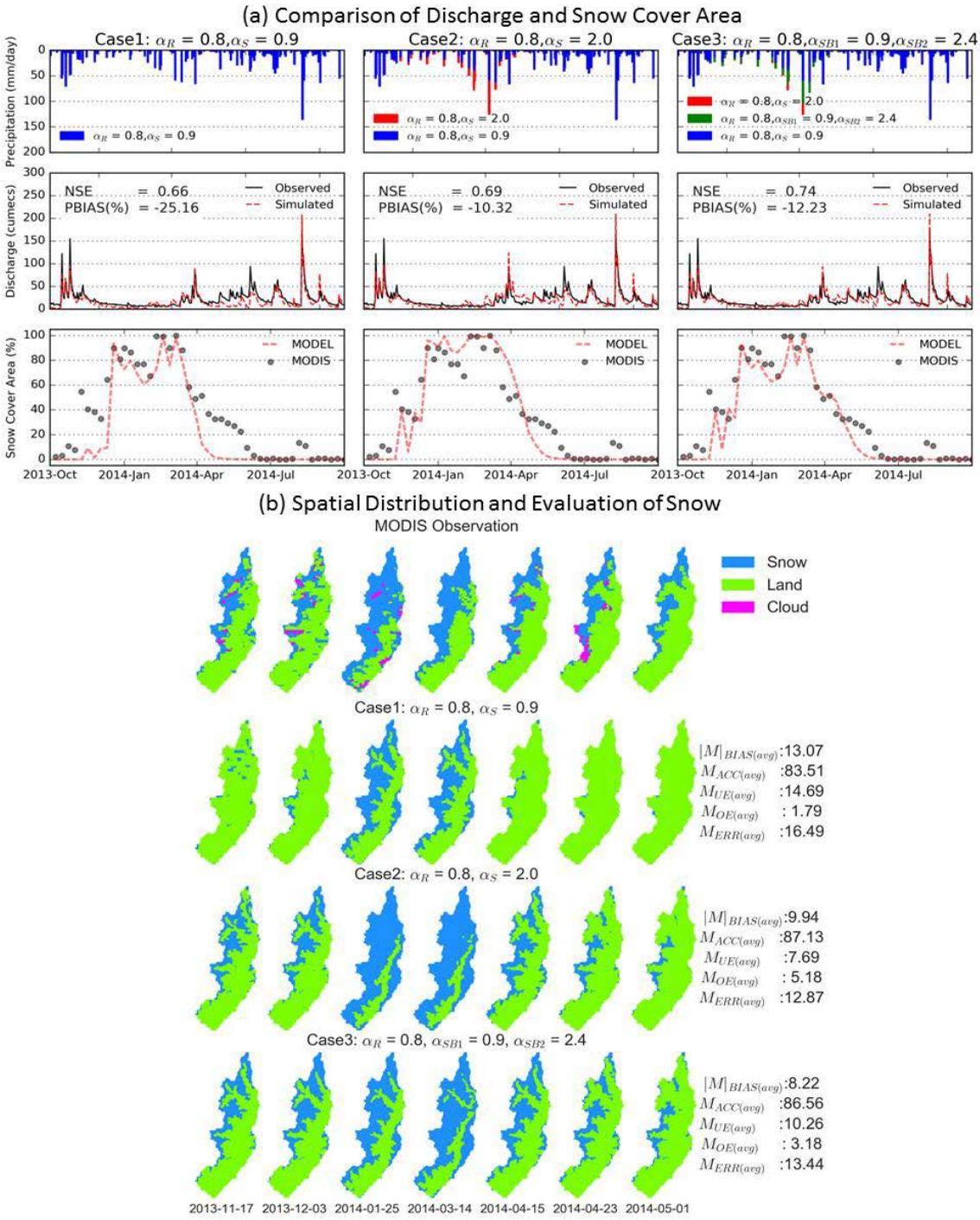

Figure 6.14. Bias Correction Factors for rain and snow Case 1: α_R= 0.80, α_S= 0.90, Case 2: α_R= 0.80, α_S= 2.0 and Case 3: α_R= 0.80, α_{SB1}= 0.90, α_{SB1}= 2.40 for (a) simulated discharge and snow cover area (%) with MODIS (MOD10A2) snow extent and (b) Spatial distribution of snow with pixel-by-pixel evaluation

6.5.4. Snow Parameters Calibration

As described earlier in the methodology section, the model has some default snow parameters such as threshold of temperature (T_{thrs}) and snow aging parameters associated with albedo within visible (VIS) and near infrared (NIR) bands. Initially the threshold temperature value was set to 0 °C (273.15 K) and albedo in VIS and NIR Bands were set to 0.85 and 0.65 respectively.

Firstly, the threshold temperature is discussed in detail, followed by the snow aging parameter. Three distinct cases with changes in temperature under control model simulations are presented to demonstrate the disparity of flows and significant change in the spatial distribution of precipitation mainly snowfall with ablation and accumulation. As a control run, the BCFs for rainfall and snowfall are maintained as achieved in Case 3 of Section 6.3 (α_R= 0.8, α_{SB2}= 0.9 and α_{SB2}= 2.4) with the aging parameters set as default (VIS = 0.85 and NIR = 0.65). A smaller domain is selected to express the variation in discharge and snow during the winter season (mid-January to mid-May) when most of the accumulation and ablation occur.

Three different cases are discussed here with different threshold temperatures by observing the change in the discharge and distribution of snow in comparison with the observed discharge and MODIS-derived snow extent over the basin. With other parameters set as the control run described above, in Case 1 comprises of the threshold temperature as 0 °C (273.15 K). In this case the flow conditions exhibition NSE = 0.63 and PBIAS = 21% (Figure 6.15a) and pixel-by-pixel spatial distribution analysis shows $M_{ACC(avg)}$ = 82.26% and $|M|_{BIAS(avg)}$ = 7.91% (Figure 6.15b). For the second case (Case 2), the threshold temperature was increased to 1 °C (274.15K) due to which the

precipitation amount changed considerably (+6%), as shown in Figure 6.15a (Case 2). In addition to the quantity the spatial distribution also changed because, with increase in threshold temperature the precipitation phase ration (rain : snow), as in considerable portion of precipitation transforms more into snowfall compared to rainfall causing more accumulation Figure 6.15b (Case 2). As a result the of this increase, the NSE reduced from 0.63 to 0.57 and PBIAS increased from 21.23% to 26.3% as more snow accumulation altered the flow regime substantially Figure 6.15b (Case 2). However, the spatial distribution of snow cover as compared to MODIS was upgraded as pixel-by-pixel analysis came out with significant drop in $|M|_{BIAS(avg)}$ and changed from 7.91% to 4.76% and $M_{ACC(avg)}$ increased from 82.26% to 85.16%, as per graphics in shown in Figure 6.15b (Case 2). With threshold temperature as 1 °C (274.15 K) the magnitude for the average overestimation ($M_{OE(avg)}$ = 7.05%) and underestimation ($M_{UE(avg)}$ = 7.78%) was found to be almost the same. While considering the third case with threshold temperature set to 2 °C (275.15 K), the precipitation amount altered more vividly (+11.5%) and resulted in significant overestimation of discharge poorly described by the an NSE less than 0.5 and PBIAS over 30%, as evident in Figure 6.15a (Case 3). In addition to the flow conditions, the spatial distribution of snow also resulted in overestimation of the sow cover in comparison with the MODIS snow extents.

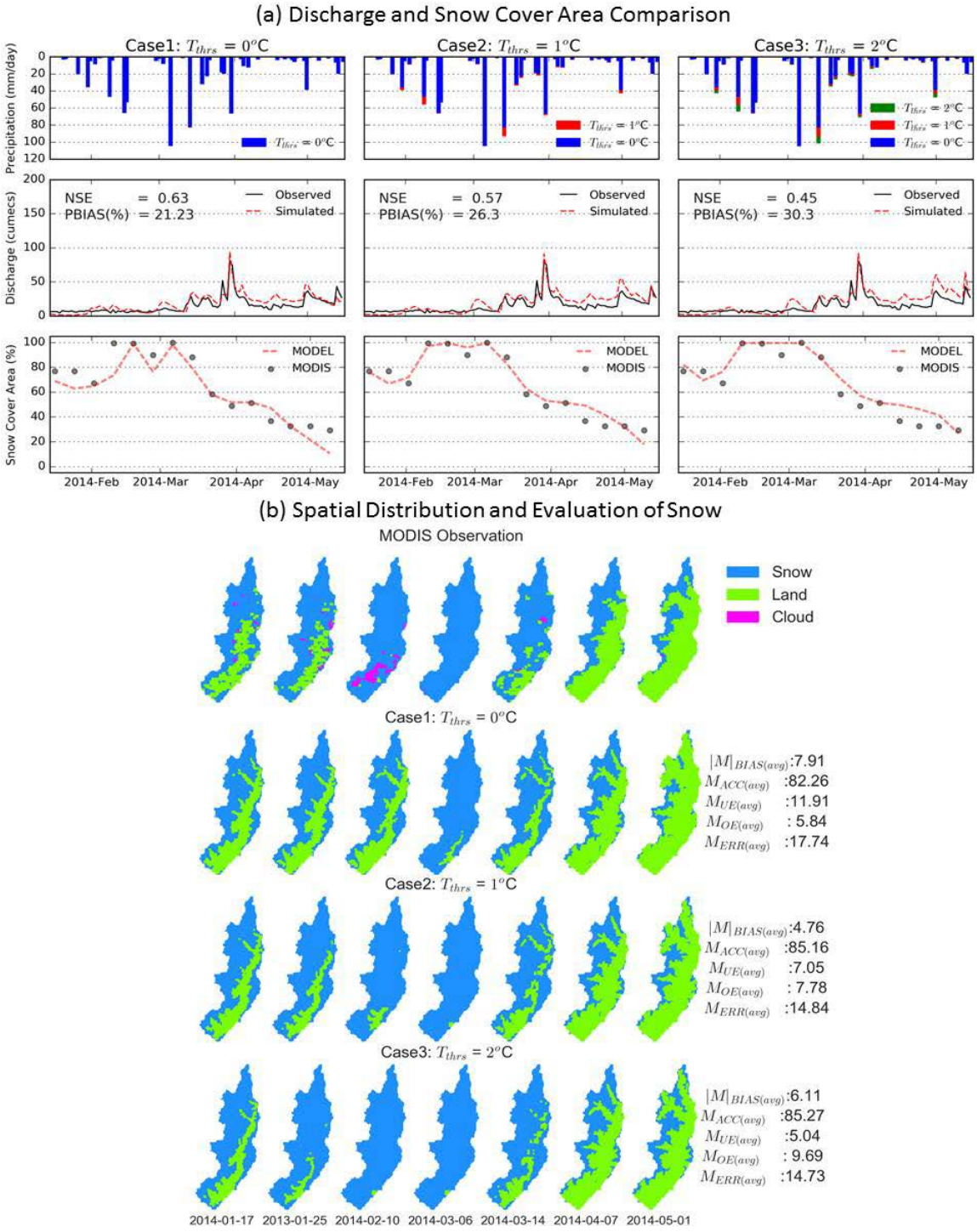

Figure 6.15. Threshold temperatures Case 1 : $T_{thrs} = 0$ °C, Case 2 : $T_{thrs} = 1$ °C, and Case 3 : $T_{thrs} = 2$ °C for (a) Comparisons of simulated discharge and snow cover area (%) with MODIS (MOD10A2) snow extent and (b) Spatial distribution of snow with pixel-by-pixel evaluation

The pixel-by-pixel evaluation presented in graphics of Figure 6.15b (Case 3) came up with a minor increase in $M_{ACC(avg)}$ from 85.27% to 85.16% in previous cases whereas the $|M|_{BIAS(avg)}$ increased from 4.76% in previous cases to 6.11%. Substantial increases in precipitation with ample amount of snow accumulated over the basin in Case 3 and exhibited poor evaluation for both flow regime and spatial distribution of the snow; therefore, the threshold temperature for this study was considered as 1 °C (274.15 K) hereafter.

The controlled conditions set for the demonstration of the snow aging parameter are as described previously but with a threshold temperature set at 1 °C (274.15 K) considered as Case 2. Mainly, the snow aging parameter governs the accumulation and melting rate and has nothing to do with precipitation. Therefore, for the same precipitation, different snow aging parameters altered flow conditions extensively due to the different spatial distributions of snow.

As compared to Case 2, firstly, the visible and near infrared albedo were reduced to 0.8 and 0.6 from 0.85 to 0.65 respectively in Case 2. With this decrease in albedo, more radiations are absorbed as compared to reflectance. Therefore, the accumulated snow melts with much faster rate that resulted in overestimation of flow with NSE = 0.51 and PBIAS = 29.33%, as presented in Figure 6.16a (Case 1). Conversely, the results for pixel-by-pixel analysis and spatial distribution of snow in Figure 6.16b (Case 1) showed decline in $M_{ACC(avg)}$ from 85.16% to 83.22%, with increase in $|M|_{BIAS(avg)}$ from 4.76% to 7.05%.

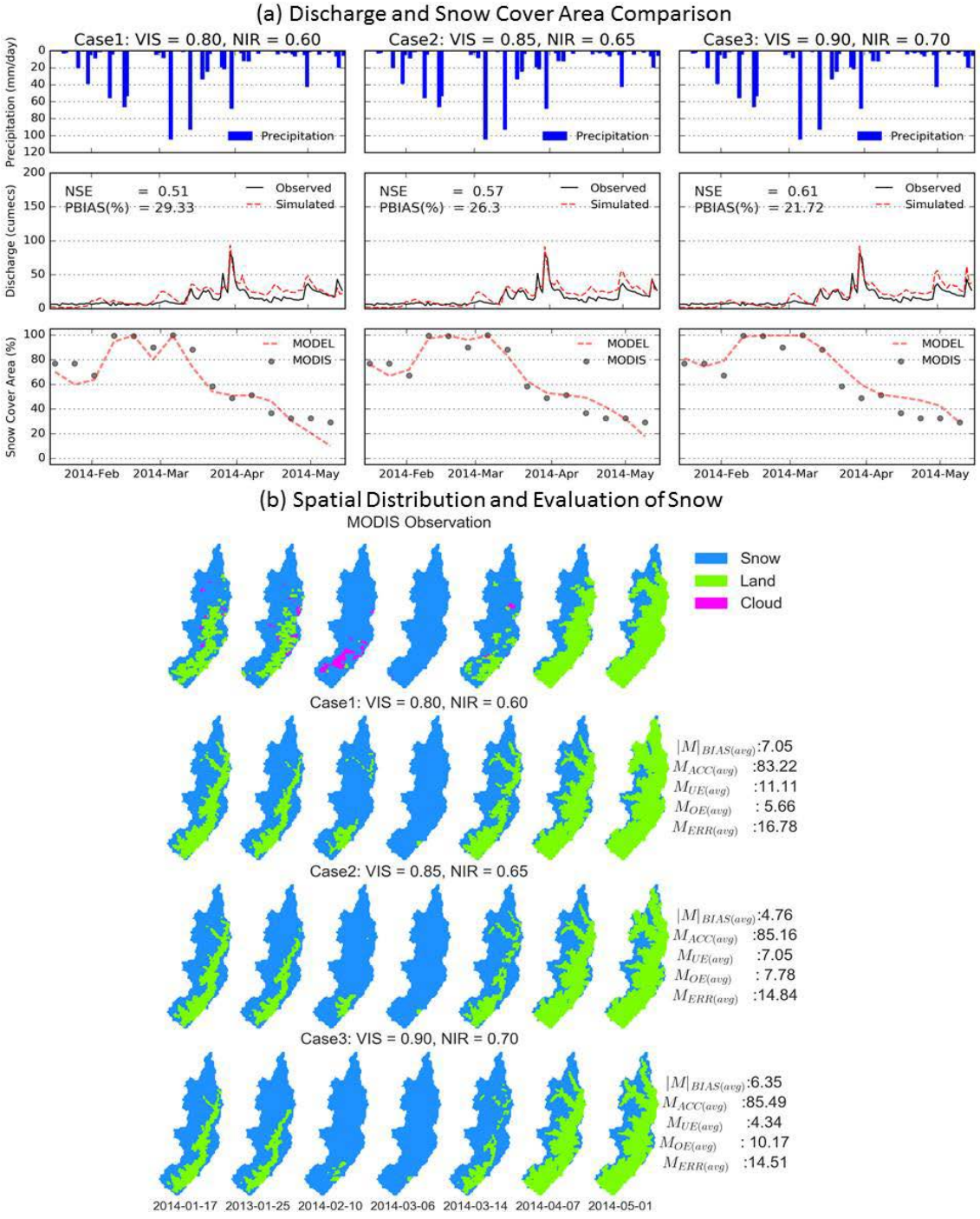

Figure 6.16. Snow aging parameter under visible an near-infrared albedo for Case 1: VIS = 0.80, NIR = 0.60, Case 2: VIS = 0.85, NIR = 0.65 and Case 3: VIS = 0.90, NIR = 0.70 (a) simulated discharge and snow cover area (%) with MODIS (MOD10A2) snow extent and (b) Spatial distribution of snow with pixel-by-pixel evaluation

Yet in Case 3, the snow albedo (both VIS and NIR) were increased from 0.85 to 0.90 and 0.65 to 0.70, with which more of the radiative energy was reflected back causing the delay in melting of snow, compared to both prior cases (Case1 and Case2).

The discharge situation improved considerably with NSE = 0.61 and PBIAS reduced from the 29.33% to 21.72%. The spatial distribution of snow cover was immensely elevated with $M_{ACC(avg)}$ = 85.5%, and with slight overestimation the $|M|_{BIAS(avg)}$ increased to 6.35% as described in graphics from Figure 6.16b (Case 3). In this way step-by-step method, the model performance was enhanced based on the evaluation indices for both discharge and pixel-by-pixel analysis for snow cover in addition to visual inspection.

6.6. Calibration and Validation

Based on the step-by-step procedure described above, the model was calibrated for the hydrological year October 2013–September 2014 with NSE = 0.76 and PBIAS = -9.08% for discharge and with $M_{ACC(avg)}$ = 88.15% and $|M|_{BIAS(avg)}$ = 7.17% for the spatial distribution of snow (Figure 6.17a). Later on, the model ouputs were validated for the next 3 hydrological years from Oct 2014 to Sep 2017, with NSE 0.74, 0.75 and 0.65 and PBIAS -9.91%, -1.85% and -5.67% for a discharge with $M_{ACC(avg)}$ = 87.68%, 85.9%, and 85.29% for 3 years respectively (Figure 6.17b).

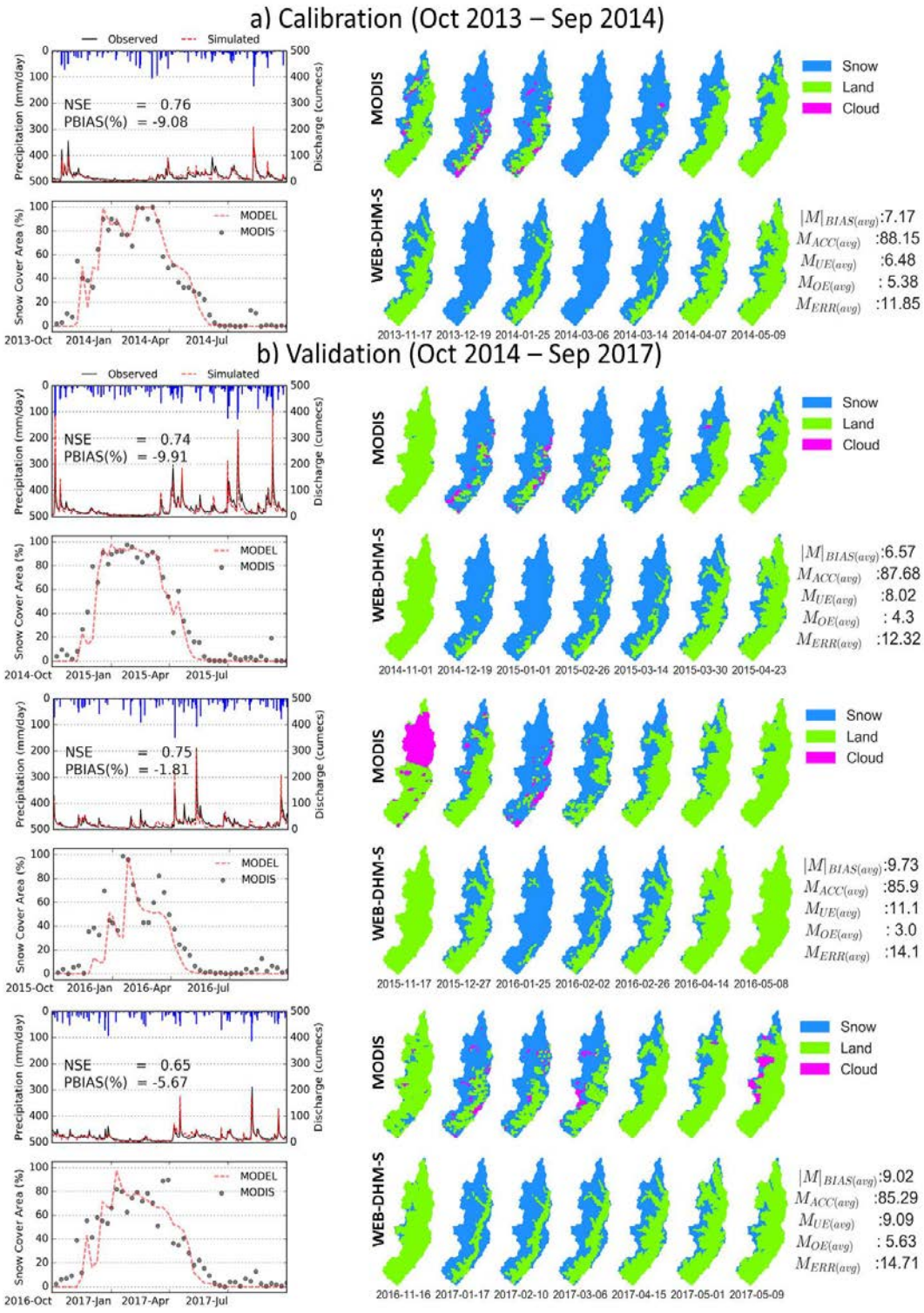

Figure 6.17. Comparison of simulated discharge vs observed discharge and Model Simulated SCA with MODIS (a) Calibration (October 2014–September 2015) (b) Validation (October 2014–September 2017)

7. Conclusion and Policy Implications

7.1. Conclusions

This study proposed a novel approach to integrate 3-D distribution/profiles from the JRA-55 reanalysis product for the computation of temperature over a river basin and to develop a deterministic and physically-based distributed hydrological modeling framework to deal with uncertainties by connecting the merits of observational data with atmospheric reanalysis data.

The VPT was developed at the basin scale by using JRA-55 geopotential heights and temperature data at various vertical levels reconstructed based on the in-situ observational temperature data. With VPT, it was confirmed that the lapse rate over the mountain terrain is different from the environmental lapse rate primarily governed by the existence or nonexistence of moisture and other orographic factors.

Based on the VPT and threshold temperature (freezing temperature for rain/snow), the precipitation was classified as snow and rain. It was observed that, despite calibration from multiple sources, composite radar products are still unable to correctly capture the intensity and resulted in substantial overestimation of rainfall and the underestimation of and snowfall. Another major problem is radar retrieval capability against the snow/ice and liquid rain especially in transitional seasons such as pre winter or post-winter when temperatures along the elevation are considerably variable.

After fixing the precipitation and land surface parameters, the spatiotemporal BCF was then determined for the cold season (pre-, mid-, and post-winter). We segregated the coexistence of snow and rain (mixed precipitation), based on elevational bands and a different correction factor for mixed precipitation and snowfall. The cold season output

was calibrated with snow hydrological parameters, such as the threshold temperature for rain/snow and snow aging.

It has been demonstrated that improved basic inputs for the hydrological modeling system can significantly reduce uncertainties, facilitating human and computational efforts for calibration and validation. Therefore, more time can be utilized to perform hydrological analysis from small-scale basins to large extents. During calibration of the snow hydrological parameters, it was observed that improvement in efficiency for one criterion might affect another. Some parameters resulted in a higher efficiency for discharge while, at the same time, they presented a poor match for the spatial distribution of snow cover. The study is found to be critically important for interpreting and understanding the collective role of temperature and precipitation trends for variations in streamflows.

7.2. Future Works and Policy Implications

The framework was applied to the Oi River Basin of Japan owing to policy implications regarding the maximization of hydropower generation and the minimization of flood damages to downstream properties by improving the dam operation. Precise estimation and prediction of discharge information are crucial for practitioners engaged in policy, planning and operational roles for catchment management. There are a series of dams constructed in the Oi River catchment namely Nagashima Dam, Ikawa Dam, Hatanagi-II Dam, Hatanagi-I Dam, Akaishi Dam and Tashiro Dam producing a significant amount of hydropower and protecting from the anticipated flooding. Primarily, the Hatanagi-I, Hatanagi-II, Ikawa and Nagashima Dam are operated from standpoint of power generation with storage capacity which is regulated and controlled by the relevant authorities.

There is significant share of water that sustains the streamflows in the Oi River Basin is from snow. In winter the northern part of the Oi River basin is completely covered with snow from the mid-December to the mid-March which completely melts away during the spring season and there is no snow in the summer season from mid-June to end of September. Thus, the generation of hydropower plants from these dams is subject to seasonal snow cover. If this snow can be accurately simulated under different climatic and atmospheric conditions the relevant authorities can operate and manage the reservoir operation for optimization of hydropower generation. The rainfall estimation is ambiguous despite of modern advancements and technology. On the other hand, snow exists and can be observed through remote sensing. It governs the stream flow when there is no rainfall and if we can predict the stream flow based on the temperature change the water management will be more effective for hydropower generation, flood protection and water supply.

The applicability of the proposed framework is not limited to Oi River Basin but can be applied to any mountainous region with snow/glaciers. The preservation and management of water resources are becoming the biggest of all the challenges. Moreover, the in practice approaches for water resource management are becoming incompatible. Climate change on the other hand is alarming for the regions with snow and glaciers as there are serious concerns due to rises in temperature that may sooner or later affect river flows in the future originating from such regions. It is therefore essential to predict the snow and glacier melt runoff to manage future water resources.

References

Abatzoglou, J. (2011). Influence of the PNA on declining mountain snowpack in the Western United States. *International Journal of Climatology*, *31*(8), 1135–1142. http://doi.org/10.1002/joc.2137

Abbott, M. B., Bathurst, J. C., Cunge, J. A., O'Connell, P. E., & Rasmussen, J. (1986). An introduction to the European Hydrological System — Systeme Hydrologique Europeen, "SHE", 2: Structure of a physically-based, distributed modelling system. *Journal of Hydrology*, *87*(1–2), 61–77. http://doi.org/10.1016/0022-1694(86)90115-0

Adikari, Y., & Yoshitani, J. (2009). *Global Trends in Water-Related Disasters: an insight for policymakers Water in a Changing World Global Trends in Water-Related Disasters: an insight for policymakers*. *The United Nations World Water Assessment Programme: Side publications series*. France.

Alexander, L. V., Zhang, X., Peterson, T. C., Caesar, J., Gleason, B., Klein Tank, A. M. G., … Vazquez-Aguirre, J. L. (2006). Global observed changes in daily climate extremes of temperature and precipitation. *Journal of Geophysical Research Atmospheres*, *111*(5), 1–22. http://doi.org/10.1029/2005JD006290

Anders, A. M., Roe, G. H., Hallet, B., Montgomery, D. R., Finnegan, N. J., & Putkonen, J. (2006). Spatial patterns of precipitation and topography in the Himalaya. *Geological Society of America*, *398*(1003), 39–53. http://doi.org/10.1130/2006.2398(03)

AR4. (2008). *Climate Change 2007: Impacts, Adaptation and Vulnerability. Contribution of Working Group II to the Fourth Assessment Report of the Intergovernmental Panel on Climate Change*. *Journal of Environment Quality* (Vol. 37). http://doi.org/10.2134/jeq2008.0015br

Barnett, T. P., Adam, J. C., & Lettenmaier, D. P. (2005). Potential impacts of a warming climate on water availability in snow-dominated regions. *Nature*, *438*(7066), 303–309. http://doi.org/10.1038/nature04141

Berne, A., Delrieu, G., Creutin, J.-D., & Obled, C. (2004). Temporal and spatial resolution of rainfall measurements required for urban hydrology. *Journal of Hydrology*, *299*(3–4), 166–179. http://doi.org/10.1016/J.JHYDROL.2004.08.002

Bevan, K. (2001). How far can we go in distributed hydrological modelling? *Hydrological and Earth System Sciences*, *5*(1), 1–12.

Bevan, K., & Kirkby, M. (1978). A physically based, variable contributing area model of basin hydrology. *Hydrological Sciences*, *24*(1), 43–69.

Blandford, T. R., Humes, K. S., Harshburger, B. J., Moore, B. C., Walden, V. P., & Ye, H. (2008). Seasonal and synoptic variations in near-surface air temperature lapse rates in a mountainous basin. *Journal of Applied Meteorology and Climatology*, *47*(1), 249–261. http://doi.org/10.1175/2007JAMC1565.1

Carturan, L., Fontana, G. D., & Borga, M. (2012). Estimation of winter precipitation in a high-altitude catchment of the Eastern Italian Alps: Validation by means of glacier mass balance observations. *Geografia Fisica e Dinamica Quaternaria*,

35(1), 37–48. http://doi.org/10.4461/GFDQ.2012.35.4

Cesaraccio, C., Spano, D., Duce, P., & Snyder, R. L. (2001). An improved model for determining degree-day values from daily temperature data. *International Journal Biometeorol*, *45*, 161–169.

Cherkauer, K. A., Bowling, L. C., & Lettenmaier, D. P. (2003). Variable infiltration capacity cold land process model updates. *Global and Planetary Change*, *38*, 151–159. http://doi.org/10.1016/S0921-8181(03)00025-0

Clark, M., & Slater, A. (2006). Probabilistic Quantitative Precipitation Estimation in Complex Terrain. *Journal of Hydrometeorology*, *7*(2006), 3–22.

Cooper, S., Wood, N., & L 'ecuyer, T. (2017). A variational technique to estimate snowfall rate from coincident radar, snowflake, and fall-speed observations. *Atmospheric Measurement Techniques*, *10*(2017), 2557–2571. http://doi.org/10.5194/amt-10-2557-2017

Dahri, Z. H., Ludwig, F., Moors, E., Ahmad, B., Khan, A., & Kabat, P. (2016). An appraisal of precipitation distribution in the high-altitude catchments of the Indus basin. *Science of the Total Environment*, *548–549*, 289–306. http://doi.org/10.1016/j.scitotenv.2016.01.001

Dickinson, R., Henderson-Sellers, A., & Kennedy, J. Biosphere-atmosphere Transfer Scheme (BATS) Version 1e as Coupled to the NCAR Community Climate Model, NCAR Tech. Rep. NCAR/TN-3871STR, 72 77 (1993). http://doi.org/10.5065/D67W6959

Dimri, A. P. (2014). How robust and (un)certain are regional climate models over the Himalayas? *The Cryosphere Discussions*, *8*, 6251–6270. http://doi.org/10.5194/tcd-8-6251-2014

Ebita, A., Kobayashi, S., Ota, Y., Moriya, M., Kumabe, R., Onogi, K., … Ishimizu, T. (2011). The Japanese 55-year Reanalysis “JRA-55”: An Interim Report. *SOLA*, *7*, 149–152. http://doi.org/10.2151/sola.2011-038

EPA. (2013). 2013 Freshwater Aquatic Life Ambient Water Quality Criteria for Ammonia. https://www.epa.gov/sites/production/files/2015-08/documents/aquatic-life-ambient-water-quality-criteria-for-ammonia-freshwater-2013.pdf

Ewen, J., Parkin, G., & Enda O ’connell, P. (2000). Shetran: Distributed River Basin Flow and Transport Modeling System. *Journal of Hydrologic Engineering*, *250*.

Foglia, L., Hill, M. C., Mehl, S. W., & Burlando, P. (2009). Sensitivity analysis, calibration, and testing of a distributed hydrological model using error-based weighting and one objective function. *Water Resources Research*, *45*(6), 1–18. http://doi.org/10.1029/2008WR007255

Frans, C., Istanbulluoglu, E., Lettenmaier, D., Clarke, G., Bohn, T., & Stumbaugh, M. (2016). Implications of decadal to century scale glacio-hydrological change for water resources of the Hood River basin, OR, USA. *Hydrological Processes*, *30*(23), 4314–4329. http://doi.org/10.1002/hyp.10872

Garen, D. C., & Marks, D. (2005). Spatially distributed energy balance snowmelt modelling in a mountainous river basin: estimation of meteorological inputs and

verification of model results. *Journal of Hydrology*, *315*(2005), 126–153. http://doi.org/10.1016/j.jhydrol.2005.03.026

Ghaemi, E., Kavianpour, M., Moazami, S., Hong, Y., & Ayat, H. (2017). Uncertainty analysis of radar rainfall estimates over two different climates in Iran. *International Journal of Remote Sensing*, 1–21. http://doi.org/10.1080/01431161.2017.1335909

Goodison, B., Sevruk, B., & Klemm, S. (1989). WMO Solid Precipitation Measurement Intercomparision: Objectives, Methodology, Analysis. *Atmospheric Déposition*, (179).

Grell, G. A., Dudhia, J., & Stauffer, S. R. (1994). *A description of the Fifth-generation Penn State/NCAR Mesoscale Model (MM5). NCAR Technical Note NCAR/TN-398+STR*. http://doi.org/10.5065/D60Z716B

Harlow, R. C., Burke, E. J., Scott, R. L., Shuttleworth, W. J., Brown, C. M., & Petti, J. R. (2004). Research Note: Derivation of temperature lapse rates in semi-arid south-eastern Arizona. *Hydrology and Earth System Sciences*, *8*(6), 1179–1185. http://doi.org/10.5194/hess-8-1179-2004

Hazenberg, P., Yu, N., Boudevillain, B., Delrieu, G., & Uijlenhoet, R. (2011). Scaling of raindrop size distributions and classification of radar reflectivity-rain rate relations in intense Mediterranean precipitation. *Journal of Hydrology*. http://doi.org/10.1016/j.jhydrol.2011.01.015

Heynen, M., Miles, E., Ragettli, S., Buri, P., Immerzeel, W. W., & Pellicciotti, F. (2016). Air temperature variability in a high-elevation Himalayan catchment.

Annals of Glaciology, *57*(71), 212–222. http://doi.org/10.3189/2016AoG71A076

Hofstra, N., Haylock, M., New, M., Jones, P., & Frei, C. (2008). Comparison of six methods for the interpolation of daily, European climate data. *Journal of Geophysical Research*, *113*, D21110. http://doi.org/10.1029/2008JD010100

Hofstra, N., & New, M. (2009). Spatial variability in correlation decay distance and influence on angular-distance weighting interpolation of daily precipitation over Europe. *International Journal of Climatology*, *29*, 1872–1880. http://doi.org/10.1002/joc

Immerzeel, W. W., Droogers, P., de Jong, S. M., & Bierkens, M. F. P. (2009). Large-scale monitoring of snow cover and runoff simulation in Himalayan river basins using remote sensing. *Remote Sensing of Environment*, *113*(1), 40–49. http://doi.org/10.1016/j.rse.2008.08.010

Immerzeel, W. W., Pellicciotti, F., & Shrestha, A. B. (2012). Glaciers as a Proxy to Quantify the Spatial Distribution of Precipitation in the Hunza Basin. *Mountain Research and Development*, *32*(1), 30–38. http://doi.org/10.1659/MRD-JOURNAL-D-11-00097.1

Immerzeel, W. W., Petersen, L., Ragettli, S., & Pellicciotti, F. (2014). The importance of observed gradients of air temperature and precipitation for modeling runoff from a glacierized watershed in the Nepalese Himalayas. *Water Resources Research*, *50*(March 2014), 2212–2226. http://doi.org/10.1002/2013WR014506

Immerzeel, W. W., van Beek, L., & Bierkens, M. (2010). Climate Change Will Affect

the Asian Water Towers. *Science*, *328*, 1382–1384. http://doi.org/10.1126/science.1183188

Immerzeel, W. W., van Beek, L. P. H., Konz, M., Shrestha, A. B., & Bierkens, M. F. P. (2012). Hydrological response to climate change in a glacierized catchment in the Himalayas. *Climatic Change*, *110*(3–4), 721–736. http://doi.org/10.1007/s10584-011-0143-4

IPCC. (2007). *Climate Change 2007: impacts, adaptation and vulnerability: contribution of Working Group II to the fourth assessment report of the Intergovernmental Panel*. http://doi.org/10.1256/004316502320517344

IPCC. (2014). *Climate Change 2014: Impacts, Adaptation, and Vulnerability. Summaries, Frequently Asked Questions, and Cross-Chapter Boxes*. *Climate Change 2014: Impacts, Adaptation, and vulnerability. Contribution of Working Group II to the Fifth Assessment Report of the Intergovernmental Panel on Climate Change*. http://doi.org/10.1016/j.renene.2009.11.012

Jennings, K. S., Winchell, T. S., Livneh, B., & Molotch, N. P. (2018). Spatial variation of the rain–snow temperature threshold across the Northern Hemisphere. *Nature*, *9*(1148). http://doi.org/10.1038/s41467-018-03629-7

Jin, J., Gao, X., Yang, Z.-L., Bales, R. C., Sorooshian, S., Dickinson, R. E., … Wu, G. X. (1999). Comparative Analyses of Physically Based Snowmelt Models for Climate Simulations. *Journal of Climate*, *12*(8), 2643–2657. http://doi.org/10.1175/1520-0442(1999)012<2643:CAOPBS>2.0.CO;2

JMA. (2013). *JRA-55 Product Users' Handbook, 1.25-degree latitude/longitude*. http://jra.kishou.go.jp/JRA-55/document/JRA-55_handbook_LL125_en.pdf

JMA. (2018). *WMO/ASEAN Training Workshop on Weather Radar Data Quality and Standardization Hands-on Training on Weather Radar QC*.

Jones, R. W., Renfrew, I. A., Orr, A., Webber, B. G. M., Holland, D. M., & Lazzara, M. A. (2016). Evaluation of four global reanalysis products using in situ observations in the Amundsen Sea Embayment, Antarctica. *Journal of Geophysical Research: Atmospheres*, *121*(11), 6240–6257. http://doi.org/10.1002/2015JD024680

Kattel, D., Yao, T., Yang, K., Tian, L., Yang, G., & Joswiak, D. (2013). Temperature lapse rate in complex mountain terrain on the southern slope of the central Himalayas. *Theoretical and Applied Climatology*, *113*(3–4), 671–682. http://doi.org/10.1007/s00704-012-0816-6

Kattel, D., Yao, T., Yang, W., Gao, Y., & Tian, L. (2015). Comparison of temperature lapse rates from the northern to the southern slopes of the Himalayas. *International Journal of Climatology*, *35*, 4431–4443. http://doi.org/10.1002/joc.4297

Khan, S. I., Hong, Y., Gourley, J. J., Khattak, M. U., & De Groeve, T. (2014). Multi-sensor imaging and space-ground cross-validation for 2010 flood along Indus River, Pakistan. *Remote Sensing*, *6*(3), 2393–2407. http://doi.org/10.3390/rs6032393

Kobayashi, S., Ota, Y., Harada, Y., Ebita, A., Moriya, M., Onoda, H., … Takahashi, K. (2015). The JRA-55 reanalysis: General specifications and basic characteristics.

Journal of the Meteorological Society of Japan, *93*(1), 5–48. http://doi.org/10.2151/jmsj.2015-001

Kulie, M., & Bennartz, R. (2009). Utilizing spaceborne radars to retrieve dry Snowfall. *Journal of Applied Meteorology and Climatology*, *48*(12), 2564–2580. http://doi.org/10.1175/2009JAMC2193.1

Kunstmann, H., Krause, J., & Mayr, S. (2006). Inverse distributed hydrological modelling of Alpine catchments. *Hydrology and Earth System Sciences*, *10*(3), 395–412. http://doi.org/10.5194/hess-10-395-2006

Li, X., Gao, F., Wang, J., & Strahler, A. (2001). A Priori Knowledge Accumulation and Its Application to Linear BRDF Model Inversion. *Journal of Geophysical Research Atmospheres*, *106(D11)*, 11,925-11,935.

Li, X., Wang, L., Chen, D., Yang, K., Xue, B., & Sun, L. (2013). Near-surface air temperature lapse rates in the mainland China during 1962-2011. *Journal of Geophysical Research Atmospheres*, *118*(14), 7505–7515. http://doi.org/10.1002/jgrd.50553

Liang, X., Lettenmaier, D. P., Wood, E. F., & Burges, S. J. (1994). A simple hydrologically based model of land surface water and energy fluxes for general circulation models. *Journal of Geophysical Research*, *99*(D7), 14415. http://doi.org/10.1029/94JD00483

Liu, Y., & Gupta, H. V. (2007). Uncertainty in hydrologic modeling: Toward an integrated data assimilation framework. *Water Resources Research*, *43*(7).

http://doi.org/10.1029/2006WR005756

Luo, L., Robock, A., Vinnikov, K. Y., Schlosser, C. A., Slater, A. G., Boone, A., … Yang, Z.-L. (2003). Effects of Frozen Soil on Soil Temperature, Spring Infiltration, and Runoff: Results from the PILPS 2(d) Experiment at Valdai, Russia. *Journal of Hydrometeorology*, *4*(2), 334–351. http://doi.org/10.1175/1525-7541(2003)4<334:EOFSOS>2.0.CO;2

Madsen, H. (2000). Automatic calibration of a conceptual rainfall–runoff model using multiple objectives. *Journal of Hydrology Elsevier Science Publishers B.V*, *235*, 276–288.

Makahira, Y., Uekiyo, N., Tabata, A., & Abe, Y. (1996). Accuracy of Radar-AMeDAS Precipitation. *IEICE Trans. Commun., B*, *79*(6), 751–762.

Marshall, S. J., Sharp, M. J., Burgess, D. O., & Anslow, F. S. (2007). Near-surface-temperature lapse rates on the Prince of Wales Icefield, Ellesmere Island, Canada: implications for regional downscaling of temperature. *International Journal of Climatology*, *27*(3), 385–398. http://doi.org/10.1002/joc.1396

Maurer, E. P., Wood, A. W., Adam, J. C., Lettenmaier, D. P., & Nijssen, B. (2002). A long-term hydrologically based data set of land surface fluxes and states for the conterminous United States: Updates and extensions. *Journal of Climate*, *15*(1993), 3237–3251. http://doi.org/10.1175/JCLI-D-12-00508.1

Minder, J. R. (2010). The Sensitivity of Mountain Snowpack Accumulation to Climate Warming. *Journal of Climate*, *23*(2010), 2634–2650.

http://doi.org/10.1175/2009JCLI3263.1

Minder, J. R., Mote, P. W., & Lundquist, J. D. (2010). Surface temperature lapse rates over complex terrain: Lessons from the Cascade Mountains. *Journal of Geophysical Research*, *115*(D14), D14122. http://doi.org/10.1029/2009JD013493

Moriasi, D. N., Arnold, J. G., Van Liew, M. W., Binger, R. L., Harmel, R. D., & Veith, T. L. (2007). Model evaluation guidelines for systematic quantification of accuracy in watershed simulations. *Transactions of the ASABE*, *50*(3), 885–900. http://doi.org/10.13031/2013.23153

Mote, P. W., Hamlet, A. F., Clark, M. P., & Lettenmaier, D. P. (2005). Declining mountain snowpack in western north America. *Bulletin of the American Meteorological Society*. http://doi.org/10.1175/BAMS-86-1-39

MRT. (2011). *Modis Reprojection Tool : User's Manual, USGS Earth Resources Observation and Science (EROS) Center*.

Nash, J., & Sutcliffe, J. (1970). River Flow Forecasting Through Conceptual Models Part I-A Discussion of Principles. *Journal of Hydrology*, *10*, 282–290. Retrieved from https://hydrology.agu.org/wp-content/uploads/sites/19/2016/04/

Nesbitt, S. W., & Anders, A. M. (2009). Very high resolution precipitation climatologies from the Tropical Rainfall Measuring Mission precipitation radar. *Geophysical Research Letters*, *36*(15), L15815. http://doi.org/10.1029/2009GL038026

Nešpor, V., & Sevruk, B. (1999). Estimation of Wind-Induced Error of Rainfall Gauge

Measurements Using a Numerical Simulation. *Journal of Atmospheric and Oceanic Technology*, *16*(4), 450–464. http://doi.org/10.1175/1520-0426(1999)016<0450:EOWIEO>2.0.CO;2

New, M., Hulme, M., & Jones, P. (2000). Representing Twentieth-Century Space–Time Climate Variability. Part II: Development of 1901–96 Monthly Grids of Terrestrial Surface Climate. *International Journal of Climatology*, *13*(13), 2217–2238. http://doi.org/10.1175/1520-0442(2000)013<2217:RTCSTC>2.0.CO;2

Ntegeka, V., Willems, P., Baguis, P., & Roulin, E. (2015). Tailored scenarios for streamflow climate change impacts based on the perturbation of precipitation and evapotranspiration. *Geophysical Research Abstracts EGU General Assembly*, *17*, 2015–4246.

Pellicciotti, F., Buergi, C., Immerzeel, W. W., Konz, M., & Shrestha, A. B. (2012). Challenges and Uncertainties in Hydrological Modeling of Remote Hindu Kush–Karakoram–Himalayan (HKH) Basins: Suggestions for Calibration Strategies. *Mountain Research and Development*, *32*(March 2012), 39–50. http://doi.org/10.1659/MRD-JOURNAL-D-11-00092.1

Pomeroy, J. W., Gray, D. M., Brown, T., Hedstrom, N. R., Quinton, W. L., Granger, R. J., & Carey, S. K. (2007). The cold regions hydrological model: a platform for basing process representation and model structure on physical evidence. *Hydrological Processes*, *21*(19), 2650–2667. http://doi.org/10.1002/hyp.6787

Praskievicz, S., & Chang, H. (2009). A review of hydrological modelling of basin-scale climate change and urban development impacts. *Progress in Physical Geography*,

33(5), 650–671. http://doi.org/10.1177/0309133309348098

Rango, A., & Martinec, J. (1995). Revisiting the degree-day method for snowmelt computations. *Journal of the American Water Resources Association*, *31*(4), 657–669. http://doi.org/10.1111/j.1752-1688.1995.tb03392.x

Rango, A., Salomonson, V. V., & Foster, J. L. (1977). Seasonal streamflow estimation in the Himalayan region employing meteorological satellite snow cover observations. *Water Resources Research*, *13*(1), 109–112. http://doi.org/10.1029/WR013i001p00109

Rigon, R., Bertoldi, G., & Over, T. M. (2006). GEOtop: A Distributed Hydrological Model with Coupled Water and Energy Budgets. *Journal of Hydrometeorology*, *7*(3), 371–388. http://doi.org/10.1175/JHM497.1

Roe, G. H. (2005). Orographic Precipitation. *Annual Review of Earth and Planetary Sciences*, *33*(1), 645–671. http://doi.org/10.1146/annurev.earth.33.092203.122541

Roe, G. H., & O'Neal, M. A. (2009). The response of glaciers to intrinsic climate variability: Observations and models of late-holocene variations in the Pacific northwest. *Journal of Glaciology*, *55*(193), 839–854. http://doi.org/10.3189/002214309790152438

Rolland, C. (2003). Spatial and seasonal variations of air temperature lapse rates in alpine regions. *Journal of Climate*, *16*(7), 1032–1046. http://doi.org/10.1175/1520-0442(2003)016<1032:SASVOA>2.0.CO;2

Saltikoff, E., Lopez, P., Taskinen, A., & Pulkkinen, S. (2015). Comparison of quantitative

snowfall estimates from weather radar, rain gauges and a numerical weather prediction model. *Boreal Environment Research*, *20*, 667–678.

Schwarb, M. (2000). The alpine precipitation climate: evaluation of a high-resolution analysis scheme using comprehensive rain-gauge data. http://doi.org/10.3929/ETHZ-A-004121274

Scott, D. T., Gooseff, M. N., Bencala, K. E., & Runkel, R. L. (2003). Automated calibration of a stream solute transport model: implications for interpretation of biogeochemical parameters. *Journal of the North American Benthological Society*, *22*(4), 492–510. http://doi.org/10.2307/1468348

Sellers, P. J., Randall, D. A., Collatz, G. J., Berry, J. A., Field, C. B., Dazlich, D. A., … Bounoua, L. (1996). A Revised Land Surface Parameterization (SiB2) for Atmospheric GCMS. Part I: Model Formulation. *Journal of Climate*, *9*(4), 676–705. http://doi.org/10.1175/1520-0442(1996)009<0676:ARLSPF>2.0.CO;2

Sevruk, B. (1997). Regional Dependency of Precipitation-Altitude Relationship in the Swiss Alps. *Climatic Change*, *36*(3/4), 355–369. http://doi.org/10.1023/A:1005302626066

Sevruk, B., Ondrás, M., & Chvíla, B. (2009). The WMO precipitation measurement intercomparisons. *Atmospheric Research*, *92*(3), 376–380. http://doi.org/10.1016/j.atmosres.2009.01.016

Shreshta, M. (2012). *Towards improved snow and glacier melt simulations in a distributed hydrological framework*. Department of Civil Engineering.

Shrestha, M., Koike, T., Hirabayashi, Y., Xue, Y., Wang, L., Rasul, G., & Ahmad, B. (2015). Integrated simulation of snow and glacier melt in water and energy balance-based, distributed hydrological modeling framework at Hunza River Basin of Pakistan Karakoram region. *Journal of Geophysical Research: Atmospheres*, *120*(10), 4889–4919. http://doi.org/10.1002/2014JD022666

Shrestha, M., Koike, T., Wang, L., Tsutsui, H., Xue, Y., & Hirabayashi, Y. (2014). Optimizing Snowfall Correction Factor for Radar-Amedas Precipitation. *Journal of Japan Society of Civil Engineers, Ser. B1 (Hydraulic Engineering)*, *70*(4), 223–228.

Shrestha, M., Wang, L., & Koike, T. (2010). Investigating the applicability of WEB-DHM to the Himalayan river basin of Nepal. *Annual Journal of Hydraulics Engineering*, *53*, 54–60.

Shrestha, M., Wang, L., Koike, T., Xue, Y., & Hirabayashi, Y. (2010). Improving the snow physics of WEB-DHM and its point evaluation at the SnowMIP sites. *Hydrology and Earth System Sciences*, *14*(12), 2577–2594. http://doi.org/10.5194/hess-14-2577-2010

Shrestha, M., Wang, L., Koike, T., Xue, Y., & Hirabayashi, Y. (2012). Modeling the Spatial Distribution of Snow Cover in the Dudhkoshi Region of the Nepal Himalayas. *Journal of Hydrometeorology*, *13*, 204–222.

Singh, P., & Jain, S. (2003). Modelling of streamflow and its components for a large Himalayan basin with predominant snowmelt yields. *Hydrological Sciences Journal*, *48*(2), 257–276. http://doi.org/10.1623/hysj.48.2.257.44693

Singh, P., & Kumar, N. (1997). Impact assessment of climate change on the hydrological response of a snow and glacier melt runoff dominated Himalayan river. *Journal of Hydrology*, *193*(96), 169403142–3.

Sixto, D. B., Shrestha, M., Wang, L., Yoshimura, K., & Koike, T. (2012). Snow Cover Modeling at the Puna Tsang River Basin in Bhutan with Corrected JRA-25 Temperature. *Annual Journal of Hydraulic Engineering, JSCE*, *56*, 235–240. http://doi.org/10.2208/jscejhe.68.I_235

Slater, A. G., Schlosser, C. A., Desborough, C. E., Pitman, A. J., Henderson-Sellers, A., Robock, A., … Xue, Y. (2001). The Representation of Snow in Land Surface Schemes: Results from PILPS 2(d). *Journal of Hydrometeorology*, *2*(1), 7–25. http://doi.org/10.1175/1525-7541(2001)002<0007:TROSIL>2.0.CO;2

Soulis, E., Kouwen, N., Pietroniro, A., Seglenieks, R., & Snelgrove, R. (2005). A Framework for Hydrological Modelling in Mags. In *Prediction in Ungauged Basins: Approaches for Canada's Cold Region* (pp. 119–138).

Storck, P., Bowling, L., Wetherbee, P., & Lettenmaier, D. (1998). Application of a GIS-based distributed hydrology model for prediction of forest harvest effects on peak stream flow in the Pacific Northwest. *Hydrological Processes*, *12*(6), 889–904. http://doi.org/10.1002/(SICI)1099-1085(199805)12

Sugiura, K., Yang, D., & Ohata, T. (2003). Systematic error aspects of gauge-measured solid precipitation in the Arctic, Barrow, Alaska. *Geophysical Research Letters*, *30*(4), 10–13. http://doi.org/10.1029/2002GL015547

Sun, S., Jin, J., & Xue, Y. (1999). A simple snow-atmosphere-soil transfer model. *Journal of Geophysical Research*.

Tahir, A., Chevallier, P., Arnaud, Y., Neppel, L., & Ahmad, B. (2011). Modeling snowmelt-runoff under climate scenarios in the Hunza River basin, Karakoram Range, Northern Pakistan. *Journal of Hydrology*, *409*(1–2), 104–117. http://doi.org/10.1016/j.jhydrol.2011.08.035

Tarboton, D., Luce, C., & Service, U. (1996). *Utah Energy Balance Snow Accumulation and Melt Model (UEB)*.

Tennant, C. J., Crosby, B. T., & Godsey, S. E. (2015). Elevation-dependent responses of streamflow to climate warming. *Hydrological Processes*, *29*(6), 991–1001. http://doi.org/10.1002/hyp.10203

Thayyen, R. J., & Dimri, A. P. (2016). Modeling Slope Environmental Lapse Rate (SELR) of temperature in the monsoon glacio-hydrological regime of the Himalaya. *The Cryosphere Discussions*, (August), 1–35. http://doi.org/10.5194/tc-2016-152

Todini, E. (1988). Rainfall-runoff modeling - Past, present and future. *Journal of Hydrology*, *100*(1–3), 341–352. http://doi.org/10.1016/0022-1694(88)90191-6

Troin, M., Arsenault, R., & Brissette, F. (2015). Performance and Uncertainty Evaluation of Snow Models on Snowmelt Flow Simulations over a Nordic Catchment (Mistassibi, Canada). *Hydrology*, *2*(2015), 289–317.

Valéry, A., Andréassian, V., & Perrin, C. (2010). Hydrological Sciences Journal

Regionalization of precipitation and air temperature over high-altitude catchments – learning from outliers Regionalization of precipitation and air temperature over high-altitude catchments – learning from outliers. http://doi.org/10.1080/02626667.2010.504676

Viviroli, D., Dürr, H., Messerli, B., Meybeck, M., & Weingartner, R. (2007). Mountains of the world, water towers for humanity: Typology, mapping, and global significance. *Water Resources Research*, *43*(7). http://doi.org/10.1029/2006WR005653

Wagener, T., & Gupta, H. V. (2005). Model identification for hydrological forecasting under uncertainty. *Stoch Environ Res Risk Assess*, *19*, 378–387. http://doi.org/10.1007/s00477-005-0006-5

Wang, L. (2007). *Development of a Distributed Runoff Model coupled with a Land Surface Scheme*. The University of Tokyo, Japan.

Wang, L., Sun, L., Shrestha, M., Li, X., Liu, W., Zhou, J., … Chen, D. (2016). Improving snow process modeling with satellite-based estimation of near-surface-air-temperature lapse rate. *Journal of Geophysical Research: Atmospheres*, *121*(2016), 12,005-12,030. http://doi.org/10.1002/2016JD025506

Wigmosta, M. S., Vail, L. W., & Lettenmaier, D. P. (1994). A distributed hydrology-vegetation model for complex terrain. *Water Resources Research*, *30*(6), 1665–1679. http://doi.org/10.1029/94WR00436

Wood, N. B., L'Ecuyer, T. S., Heymsfield, A. J., & Stephens, G. L. (2015).

Microphysical constraints on millimeter-wavelength scattering properties of snow particles. *Journal of Applied Meteorology and Climatology*, *54*(4), 909–931. http://doi.org/10.1175/JAMC-D-14-0137.1

Xue, Y., Shufen, S., Daniel, S., & Jiao, Y. (2003). Impact of parameterizations in snow physics and interface processes on the simulation of snow cover and runoff at several cold region sites. *Journal of Geophysical Research*, *108*.

Yang, D., Hearth, S., & Muisake, K. (2002). A hillslope-based hydrological model using catchment area and width functions. *Hydrological Sciences Journal*, *47*(1), 49–65. http://doi.org/10.1080/02626660209492907

Yang, D., Herath, S., & Musiake, K. (2002). A hillslope-based hydrological model using catchment area and width functions. *Hydrological Sciences Journal*, *47*(1), 49–65. http://doi.org/10.1080/02626660209492907

Yang, D., Koike, T., & Tanizawa, H. (2004). Application of a distributed hydrological model and weather radar observations for flood management in the upper Tone River of Japan. *Hydrological Processes*, *18*(16), 3119–3132. http://doi.org/10.1002/hyp.5752

Zanotti, F., Endrizzi, S., Bertoldi, G., & Regon, R. (2004). The GEOTOP snow module. *Hydrological Processes* , *18*, 3667–3679.

Zhang, F., Zhang, H., Hagen, S. C., Ye, M., Wang, D., Gui, D., … Liu, J. (2015). Snow cover and runoff modelling in a high mountain catchment with scarce data: effects of temperature and precipitation parameters. *Hydrological Processes*, *29*(1), 52–

65. http://doi.org/10.1002/hyp.10125

Appendix: 1

Table A1. Simple Biosphere 2 Model (SiB2) Legend

Value	Description
1	Broadleaf Evergreen Trees
2	Broadleaf Deciduous Trees
3	Broadleaf and Needleleaf Trees
4	Needleleaf Evergreen Trees
5	Needleleaf Deciduous Trees
6	Short Vegetation/C4 Grassland
7	Shrubs with Bare Soil
8	Dwarf Trees and Shrubs
9	Agriculture or C3 Grassland
10	Water, Wetlands
11	Ice/Snow
99	Interrupted Areas (Goodes Homolosine Projection)
100	Missing Data

Source: https://lta.cr.usgs.gov/glcc/

Appendix: 2

JRA-55 (1.25 °) latitude/longitude grid Data

Isobaric coordinates

Isobaric fields are produced for 37 isobaric surfaces (1000, 975, 950, 925, 900, 875, 850, 825, 800, 775, 750, 700, 650, 600, 550, 500, 450, 400, 350, 300, 250, 225, 200, 175, 150, 125, 100, 70, 50, 30, 20, 10, 7, 5, 3, 2 and 1 hPa) except dew-point depression (or deficit), specific humidity, relative humidity, cloud cover, cloud water, cloud liquid water and cloud ice, which are produced for 27 levels from 1000 to 100 hPa only. These fields are produced every six hours at 00, 06, 12 and 18 UTC (JMA, 2013).

Table A2. Parameters of isobaric analysis fields (anl_p125)

Code	Field Parameter	Unit	File name
7	Geopotential Height	gpm	anl_p125_hgt
11	Temperature	K	anl_p125_tmp

Source: http://jra.kishou.go.jp/JRA-55/